INVESTIGATION OF THIN CIRRUS CLOUD OPTICAL AND MICROPHYSICAL PROPERTIES ON THE BASIS OF SATELLITE OBSERVATIONS AND FAST RADIATIVE TRANSFER MODELS

A Dissertation

by

CHENXI WANG

Submitted to the Office of Graduate Studies of
Texas A&M University
in partial fulfillment of the requirements for the degree of

DOCTOR OF PHILOSOPHY

Chair of Committee,	Ping Yang
Committee Members,	George Kattawar
	Shaima Nasiri
	Gerald North
Head of Department,	Ping Yang

August 2013

Major Subject: Atmospheric Sciences

ABSTRACT

This dissertation focuses on the global investigation of optically thin cirrus cloud optical thickness (τ) and microphysical properties, such as, effective particle size (D_{eff}) and ice crystal habits (shapes), based on the global satellite observations and fast radiative transfer models (RTMs).

In the first part, we develop two computationally efficient RTMs simulating satellite observations under cloudy-sky conditions in the visible/shortwave infrared (VIS/SWIR) and thermal inferred (IR) spectral regions, respectively. To mitigate the computational burden associated with absorption, thermal emission and multiple scattering, we generate pre-computed lookup tables (LUTs) using two rigorous models, i.e., the line-by-line radiative transfer model (LBLRTM) and the discrete ordinates radiative transfer model (DISORT).

The second part introduces two methods (i.e., VIS/SWIR- and IR-based methods) to retrieve τ and D_{eff} from satellite observations in corresponding spectral regions of the two RTMs. We discuss the advantages and weakness of the two methods by estimating the impacts from different error sources on the retrievals through sensitivity studies.

Finally, we develop a new method to infer the scattering phase functions of optically thin cirrus clouds in a water vapor absorption channel (1.38-μm). We estimate the ice crystal habits and surface structures by comparing the inferred scattering phase functions and numerically simulated phase functions calculated using idealized habits.

We find two critical features of the two retrieval methods: (1) the IR-based method is more sensitive to optically thin cirrus cloud, and (2) the VIS/SWIR-based method is more sensitive to the pre-assumed ice cloud microphysical parameterization schemes. We derive the optically thin cirrus cloud phase functions based on the two methods. We find that small column-like particles (e.g., solid columns and column-aggregates) and droxtals with rough surfaces are likely to reside in optically thin cirrus clouds.

DEDICATION

This dissertation is dedicated to my mother Lihua Li and wife Yongjing Zhao.

ACKNOWLEDGEMENTS

I would like to express my respectful gratitude to my academic advisor, Dr. Ping Yang, whose insightful guidance and tremendous support during the last 4 years made it possible for me to focus on my research interest. Not only his profound knowledge and extensive learning, but also his rigorous attitude in scientific research consistently inspires me. I am deeply grateful to my committee members, Dr. George Kattawar, Dr. Shaima Nasiri, and Dr. Gerald North, for their constructive suggestions and comments during my Ph.D. study.

I also wish to express my appreciation to Drs. Bryan Baum and Steve Platnick for their important guidance and efforts on my publications, presentations, and proposal. I want to thank Drs. Heli Wei, Hironobu Iwabuchi, and Zhibo Zhang who shared their valuable experiences, which benefit my research. Thanks also go to my colleagues and group members, Shouguo Ding, Lei Bi, Feng Qian, Xie Yu, Yue Li, Bingqi Yi, Chao Liu, and Chen Zhou for their great help on both of my research and life.

The reported research was partly supported by NASA (NNX11A055G, NNX11AK37G, NNX10AM27G), a sub-award from the University of Wisconsin (301K630), and the endowment funds related to the David Bullock Harris Chair in Geosciences at the College of Geosciences, Texas A&M University.

I would like to thank my mother, Lihua Li, for her unconditional encouragement and support throughout my life. Finally, I would also like to thank my wife, Yongjing

Zhao. It was her continuous love accompanied with me throughout the past several years.

TABLE OF CONTENTS

Page

LIST OF FIGURES

FIGURE Page

LIST OF TABLES

TABLE Page

CHAPTER I

INTRODUCTION

1.1 Background of optically thin cirrus clouds

Optically thin cirrus clouds, consisting of small non-spherical ice crystals (Lynch and Sassen 2002), have received increased attention since 1980s due to their potentially radiative importance (Jensen et al. 1996; McFarquhar et al. 2000; Hartmann et al. 2001). This kind of cloud frequently occurs in the tropical upper troposphere (Prabhakara et al. 1993; Wang et al. 1994; Sassen et al. 2008) and covers approximately 30% of the tropical region between 20°N/S (Haladay and Stephens 2009). Satellite observations show that the occurrence frequency of optically thin cirrus reaches the maximum in the western Pacific region, Africa, and South America and its west coast (Prabhakara et al. 1993; Wang et al. 1994; Sassen et al. 2009). In comparison with deep convection systems, optically thin cirrus clouds have relatively longer life cycles up to 2 days (Winker et al. 1998; Luo and Rossow 2004) and larger horizontal scales up to several hundred kilometers (McFarquhar et al. 2000; Lynch and Sassen 2002; Massie et al. 2010). Optically thin cirrus clouds frequently occur above 10 km in tropics with a maximum frequency at 14 km (Sassen et al. 2009) and a typical vertical thickness 1 km, approximately (Massie et al. 2010).

Two major mechanisms are proposed for the formation of optically thin cirrus cloud near the tropical tropopause (Jensen et al. 1996). The first mechanism suggests that optically tropical thin cirrus clouds are formed due to the dissipation of outflow

anvils of tropical cumulonimbus clouds (Pfister et al. 2001). This kind of cloud is directly associated with deep convection system. The second mechanism is in situ formation. For example, ice crystals are nucleated homogeneously through a cooling effect of humid air. The occurrence of this kind of cloud is accompanied by synoptic-scale vertical uplift with a moderate ice supersaturation (e.g., <10%, Jensen et al. 1996) or Kelvin gravity waves (Boehm and Verlinde 2000; Boehm and Lee 2003; Immler et al. 2008; Fujiwara et al. 2009; Li et al. 2010).

1.2 Observations of optically thin cirrus clouds

The study of optically thin cirrus clouds near the tropical tropopause is difficult partially due to the difficult observations. In comparison with optically thick cloud, the satellite observations of optically thin cirrus cloud have relatively small signal-to-noise ratios (SNRs). In order to increase the SNRs, people investigate optically thin cirrus clouds by utilizing infrared, lidar, and other specific-designed instruments with either unique solar/viewing geometries or absorptive channels on board satellites, aircrafts, and ground stations.

1.2.1 Infrared-based observations

Infrared observations can be applied to detect optically thin cirrus clouds since ice crystals strongly absorb in this spectral region. Prabhakara et al. (1993) deduced the seasonal distribution of optically thin cirrus clouds over ocean from a high-spectral resolution instrument: the Infrared Interferometer Spectrometer (IRIS) on board the *Nimbus-4* satellite. Absorption ability of ice crystals demonstrates strong wavelength dependence in the infrared (IR) window region (i.e., 10 ~ 12 μm). For this reason,

optically thin cirrus clouds can be identified by comparing the brightness temperatures (BT) in two channels near 10.8 and 12.6 μm. By making full use of spectrum information from the High-Resolution Infrared Radiation Sounder (HIRS) on the National Oceanic and Atmospheric Administration (NOAA) Polar Orbiting Environmental Satellites, Wylie and Menzel (1999) and Stubenrauch et al. (2006) investigated the climatology of thin cirrus properties.

1.2.2 Limb-view-instrument-based observations

Limb-view-instruments observe cloud or atmosphere by eliminating the signals from the surface and therefore increase the SNRs. Wang et al. (1994, 1996) investigated the characteristics and climatology of tropical high clouds by using a satellite-based instrument of the Stratospheric Aerosol and Gas Experiment (SAGE II). The sensor of SAGE II measures the attenuated solar radiation penetrated the limb of the atmosphere in 7 narrow solar channels from near ultra-violet (UV) to near IR during sunrise and sunset periods. Observations of the SAGE II sensor are sensitive to thin cirrus clouds and have relatively high vertical resolution, due to the unique solar-viewing geometry. Another limb-view instrument, the Cryogenic Limb Array Etalon Spectrometer (CLAES), was also used for thin cirrus clouds detection (Mergenthaler et al. 1999).

1.2.3 Lidar-based observations

Lidar is a powerful active instrument that provides backscatter signal profiles of atmospheric columns with high vertical resolution (Winker et al. 1994; 1996), and therefore has inherent advantages in the detection of optically thin cloud and aerosol layers (Winker et al. 1998). Uthe and Russel (1977) detected thin cirrus clouds near the

tropical tropopause by using a ground-based lidar. The observations from the lidar In-space Technology Experiment (LITE) illustrated the possibility of lidar-based measurement from space (Winker et al. 1998; Pfister et al. 2001; Omar and Gardner 2001). Dessler et al. (2006) analyzed the vertical and horizontal distributions of optically thin cirrus clouds using the Geoscience Laser Altimeter System (GLAS) onboard the Ice, Cloud, and Land Elevation Satellite (ICESat).

Most recently, observations from the latest satellite-based lidar, Cloud-Aerosol Lidar with Orthogonal Polarization (CALIOP), on board the Cloud-Aerosol Lidar and Infrared Pathfinder Satellite Observations (CALIPSO, Winker et al. 2009) were extensively used for investigating the climatology of optically thin cirrus clouds on the global scale (e.g., Haladay and Stephens 2009; Riihimaki and McFarlane 2010).

1.2.4 1.38-μm solar reflection observations

At most solar wavelength, optically thin cirrus clouds are not quite reflective compared to the background. For example, the signal reflected by high-altitude cirrus can be more than one order of magnitude weaker than other signals contributed by the surface, lower-level clouds, and aerosol layers. Therefore, the use of solar reflection channels of passive instruments to detect thin cirrus clouds is difficult. A unique solar reflection channel centered near the 1.38-μm water vapor absorption band, however, eliminates noise from lower level atmosphere. Therefore, this channel is significantly sensitive to cirrus clouds (Gao et al. 1998). Numerous previous studies (Gao et al. 2002; Dessler and Yang 2003; Gao et al. 2004; Meyer et al. 2004; Meyer and Platnick 2010) focusing on the thin cirrus detection and inferring cloud optical properties were

conducted with observations near the 1.38-μm absorptive channel. Roskovensky and Liou (2003) designed a new method for detection thin cirrus clouds based on the 1.38- to 0.65-μm reflectance ratio and brightness temperature difference (BTD) between 8.6- and 11-μm. Wang et al. (2012) inferred cloud top heights of thin cirrus clouds based on the 1.38- to 1.24-μm reflectance ratio.

1.2.5 In situ measurements

In addition to the remote sensing approaches, in situ measurements provide direct observations of cloud microphysical properties. However, in situ measurement is difficult because of the high altitudes and thin geometric thicknesses of optically thin cirrus clouds. There was no documented in situ measurement of natural thin cirrus clouds at temperatures below –65° C until 1986. Heymsfiled (1986) measured a thin, cirriform cloud at a temperature approaching –85° C over the Marshall Islands on Dec. 17th, 1973. Specifically, a Particle Measuring System (PMS) with a one-dimensional cloud probe (1DC) was used to detect cloud particle sizes between 20 and 300 μm (Heymsfield and McFarquhar 1996). Another field campaign, the Central Equatorial Pacific Experiment (CEPEX), which aimed to investigate the microphysical properties of tropical thin cirrus clouds, was conducted in 1993 (Heymsfield and McFarquhar 1996). PMS with a 2DC probe was used to detect particle size spectrum from 40 μm to 1 mm.

However, in situ measurements suffer from artificial biases, such as the shattering effect, where large ice crystals shatter at the inlet to the probes because of collision (Heymsfield et al. 2004; Field et al. 2006). To mitigate this problem, another in

situ measurement included in a field campaign, Stratospheric-Climate Links with Emphasis on the Upper Troposphere and Lower Stratosphere (SCOUT-O_3), used improved airborne instruments: a FSSP-100 (Forward Scattering Spectrometer Probe) and a Cloud Imaging Probe (CIP). Combination of the two instruments provides measurable ice crystal size range from 2.7 to 1550 μm (de Reus et al. 2009). Most importantly, the shattering effect can be removed by distinguishing the short interarrival times due to this artificial effect from the long interarrival times representing actual ice crystals.

Obviously, in situ measurements have spatial and temporal limitations (Sassen et al. 2008). Investigation of optically thin cirrus clouds on a global scale requires a reliable method to infer properties, especially microphysical properties, of thin cirrus clouds based on satellite instruments.

1.3 Optical and microphysical properties

Optical and microphysical properties are critical parameters that determine ice cloud radiative properties. First, cloud optical properties, such as extinction optical thickness, bulk single scattering albedo, and bulk scattering phase function, describe photon paths within a cloud layer. Furthermore, the single scattering phase function (P_{11}) and single scattering albedo (ω) of individual ice cloud particles at a specified wavelength (λ) are determined by the maximum cloud particle dimension (D) and habit (H). Therefore, the bulk scattering properties of ice clouds depend on both single scattering properties and microphysical properties.

1.3.1 Basic definitions

Microphysical properties include the size and habit distributions of cloud particles, and the structures of ice crystal surfaces (e.g., degrees of surface roughness). For a given particle size distribution (PSD) and a given habit distribution (HD), the bulk scattering properties of ice cloud at a particular wavelength can be expressed as follows (Baum et al. 2005b):

$$\langle X \rangle = \frac{\int_{D_{\min}}^{D_{\max}} \left[\sum_{h=1}^{M} X_h(D) \sigma_{sca,h}(D) f_h(D) \right] \times n(D) dD}{\int_{D_{\min}}^{D_{\max}} \left[\sum_{h=1}^{M} \sigma_{sca,h}(D) f_h(D) \right] \times n(D) dD}, \qquad (1.1)$$

where X is an arbitrary single scattering variable, $n(D)$ is the PSD function, the two boundaries of the integral D_{min} and D_{max} represent the minimum and maximum sizes of ice crystals, $f_h(D)$ indicates the fraction of habit with index h, the total fraction of M different habits is 1, $\sigma_{sca,h}$ is scattering cross section. Angle brackets are used to denote bulk (averaged) scattering variables. The extinction optical thickness can be express as (Liou 2002):

$$\tau = \Delta Z \times \int_{D_{\min}}^{D_{\max}} \sum_{h=1}^{M} Q_{e,h}(D) f_h(D) A_h(D) \times n(D) dD, \qquad (1.2)$$

where τ is spectral cloud extinction optical thickness, ΔZ is the physical thickness of the cloud layer, Q_e is extinction efficiency, which approaches 2 if $D >> \lambda$, A is the projected area of an ice crystal. Note that in Eq. (1.2), the assumption that the cloud is vertically homogeneous (i.e., n and f are independent of height) is made. Although cloud PSD depicts a detailed image of ice crystals, Hansen and Travis (1974) showed that cloud

radiative properties generally depend on another parameter: effective particle size (D_{eff}). The introduction of D_{eff} simplifies parameterization in ice cloud radiation and climate studies. The parameter D_{eff} is defined as:

$$D_{eff} = \frac{3\int_{D_{\min}}^{D_{\max}} \left[\sum_{h=1}^{M} V_h(D) f_h(D) \right] \times n(D) dD}{2\int_{D_{\min}}^{D_{\max}} \left[\sum_{h=1}^{M} A_h(D) f_h(D) \right] \times n(D) dD}, \tag{1.3}$$

where V indicates the volume of a particle. This parameter has been widely used in cloud remote sensing applications (Nasiri et al. 2002) and climate studies (Fu 1996).

1.3.2 Optical and microphysical properties of optically thin cirrus clouds

The use of traditional solar-reflectance bands to inferring the τ information of thin cirrus clouds is difficult. For example, the operational τ retrieval algorithm of the Moderate Resolution Imaging Spectroradiometer (MODIS) instrument (King et al. 1997) has difficulty in retrieving cloud with τ less than 0.3 (Ackerman et al. 2008). However, the τ information can be derived from infrared observations (Inoue 1985; Prabhakara et al. 1993), lidar-based backscattering or two-way transmittance observations, and the solar reflectance information in the 1.38-μm channel (Gao et al. 2002; Dessler and Yang 2003; Meyer et al. 2004; Mayer and Platnick 2010). Jensen et al. (1996) showed the τ values of an optically thin cirrus cloud are on the order of 0.05 at 1 μm wavelength, which is calculated using airborne lidar backscattering measurement. Dessler and Yang (2003) investigate the distribution of optically thin cirrus τ by using the 1.38-μm observations of *Terra*/MODIS during a 3-day period in December 2000. For tropical thin cirrus clouds, they found that the most likely τ value is smaller than 0.02 and more than

90% cirrus samples have τ values less than 0.05. Based on two years of CALIOP/CALIPSO observations, Sassen et al. (2009) showed that more than 30% of global cirrus clouds (i.e., ice phase cloud with $\tau < 3$) are optically thin (i.e., $0.03 < \tau < 0.3$) cirrus clouds.

Although optical properties can be deduced from various remote sensing approaches, little microphysical information of optically thin cirrus clouds can be inferred due to the lack of sensitivity. For example, the observed solar reflectivity is insensitive to ice crystal size if the cloud is optically thin and observation in the IR region is insensitive to habits of ice crystals. The major knowledge of microphysical properties of thin cirrus clouds comes from direct in situ measurements. Heymsfield (1986) reported an ice crystals image within an isolated optically thin cirrus clouds near the tropical tropopause. The sizes of ice crystals in this measurement span a narrow range from 5 to 50 μm. Three typical habits within the cloud layer are: trigonal plate (thin plate with triangular cross section), solid column, and hollow column. According to the in situ measurements from the First ISCCP (International Satellite Cloud Climatology Project) Research Experiment, Phase II (FIRE II), Heymsfield and Miloshevich (1995) suggested that ice crystals within synoptic cirrus with temperatures around −40°C likely grow as 3D bullet rosette. Ice crystals with simple habits, such as quasi-spherical and column, were found in cold-topped (e.g., −60°C) synoptic cirrus (Fig. 1 in Baum et al. 2011). In the SCOUT-O3 field campaign, in situ measurements were focused on the outflow from tropical storm system. de Reus et al. (2009) reported that

the effective radius (i.e., half effective particle size) of ice crystals decreases with altitude and approached the minimum 3 μm at tropopause.

1.4 Optically thin cirrus clouds and climate

1.4.1 Radiative forcing

Clouds influence the global energy budget by reflecting solar radiation and emitting outgoing longwave emission at a low temperature (Liou 1986). However, optically thin cirrus clouds are approximately transparent to the solar radiation because of the small τ values (Rosenfield et al. 1998; McFarquhar et al. 2000). For example, Haladay and Stephens (2009) analyzed the impacts of thin cirrus clouds using the observations of CALIOP/CALIPSO instrument. The averaged shortwave radiative forcing at the top of the atmosphere for isolated thin cirrus cases is less than -2 Wm^{-2}. However, their relatively high altitudes result in a significant decrease of the outgoing longwave radiation up to 20 Wm^{-2} (Haladay and Stephens 2009). Therefore, thin cirrus clouds cause a positive radiative forcing at the top of the atmosphere. Using MODIS observations, Lee et al. (2009) investigated the radiative property of tropical optically thin cirrus clouds. According to their result, the averaged shortwave and longwave forcings for all sky cases (i.e., including clear-sky and thin cirrus cases) are -1.7 and 2.7 Wm^{-2}, respectively. The 1 Wm^{-2} net forcing in average is compatible with the effect of doubling CO_2 that leads to an approximate 4 W m^{-2} radiative forcing (e.g., Ramanathan et al. 1987). However, relatively large uncertainties remain in the radiative properties of optically thin cirrus clouds because of the limited knowledge of cloud microphysical properties.

1.4.2 Other impacts

Thin cirrus clouds also prevent the water vapor transportation from the upper troposphere to the lower stratosphere (Jensen et al. 1996; Hintsa et al. 1998; Jensen et al. 2001; Khvorostyanov and Sassen 2002; Steinwagner et al. 2010), where water vapor exists stably and has important impacts on climate (Clough et al. 1992; Solomon et al. 2010). Large-scale uplift movement initiates the homogenous nucleation process of ice crystal near tropopause. Meanwhile, the thin cirrus layer causes a local heating effect on the order of 1~2 K/day.

1.5 Motivation and objectives

Modeling thin cirrus clouds is important. By modeling thin cirrus clouds in weather prediction or climate models, understanding of the characteristics and short-term or long-term impacts of thin cirrus clouds are improved. However, the accuracy of thin cirrus cloud modeling depends on many other factors, such as the accuracy of single scattering properties of non-spherical ice particles and the optical and microphysical properties of global optically thin cirrus clouds. In this dissertation, we focus on investigating the properties of optically thin cirrus clouds on the global scale based on satellite observations and fast radiative transfer models (RTMs). The inferred global properties facilitate the simulation and parameterization of thin cirrus clouds in remote sensing applications and climate models in the future.

1.5.1 Fast radiative transfer model

Radiative transfer models, connecting cloud optical and microphysical properties to various observations, are widely applied to different applications, such as radiance

assimilation (Weng and Liu 2003), cloud retrievals (Wei et al. 2004; Yue et al. 2009; Garnier et al. 2012), and studies of cloud radiative properties. However, some rigorous RTMs, such as the discrete ordinates radiative transfer (DISORT, Stamnes et al. 1988) method, require substantial computational effort and raise a considerable issue associated with the large amount of observations. To reduce the computational burden, we develop two fast RTMs to simulate satellite observations in cloudy atmospheres in the VIS through thermal IR spectral regions.

1.5.2 Retrieval of cloud properties

Current satellite-based operational retrievals of ice cloud properties employ pre-calculated lookup tables (LUTs) of cloud transmittance and reflectance, which are based on pre-determined assumptions of ice particle size and habit distributions (Baum et al. 2005b). Therefore, satellite retrievals will be influenced by the pre-assumed microphysical parameterization schemes (Zhang et al. 2009). Furthermore, the retrievals may be also altered by the sensitivities of different spectral regions, basic assumptions in the forward model, model parameters, accuracy of model simulations, and errors from observations (Watts et al. 2011; Poulsen et al. 2012; Wang et al. 2013a). According to the operational satellite retrievals (Level-2 datasets), higher-level datasets (e.g., Level-3) are subsequently generated for climate community through specific aggregation methods depending on particular purposes. The quality of the Level-2 data, as such, continually influences further studies on climate level. For example, Yang et al. (2007) showed that the change of microphysical properties of ice clouds leads to a significant impact on instantaneous cloud radiative forcing (e.g., on the order of 10 Wm^{-2}).

Therefore, two different retrievals in different specific spectral regions are developed for two purposes: (1) understanding the impact of pre-assumed microphysical parameterization scheme on the retrieval of τ and D_{eff}; (2) investigating the optical and microphysical properties of global optically thin cirrus clouds. One year of satellite observations will be utilized to overcome the spatial and temporal limitations of in situ measurements. More details of the microphysical properties, such as habits and surface structures of ice crystals, are estimated in this study.

1.6 Organization of this dissertation

The remainder of this dissertation is organized as follows. In Chapters II and III, we introduce two different fast RTMs that simulate satellite-based observations such as solar reflection or thermal emission. Chapter IV focuses on retrieval algorithms based on the two fast RTMs and corresponding sensitivity studies. Chapter V introduces an approach to infer optically thin cirrus clouds properties from the *Aqua*/MODIS and CALIPSO/CALIOP observations. Specifically, a new method that statistically retrieves the scattering phase functions of optically thin cirrus clouds is introduced. The global properties of optically thin cirrus clouds are deduced, and optimal habits fractions of global optically thin cirrus clouds are suggested based on satellite observations and retrievals. Summary of current research is given in Chapter VI.

CHAPTER II

A FAST RADIATIVE TRANSFER MODEL FOR VISIBLE THROUGH SHORTWAVE INFRARED SPECTRAL REFLECTANCES IN CLEAR AND CLOUDY ATMOSPHERES*

2.1 Background

Fast forward radiative transfer models (RTMs) implemented for specific satellite-based instruments, also known as radiance simulators, are important to the radiance assimilation used in numerical weather prediction (NWP) systems (Weng and Liu 2003; Weng et al. 2007; Saunders et al. 1999; Saunders et al. 2007) and in the operational retrievals of atmospheric profiles (Strow et al. 2003; Jin and Li 2010; Han 2010) as well as cloud (Huang et al. 2004; Wei et al. 2004; Dubuisson et al., 2005; Wang et al. 2011; Wang et al. 2013a) and aerosol (Hsu et al 2006) properties. While numerous studies focused on the fast radiance calculations in the infrared (IR) region ($\lambda > 4$ μm) (Saunders et al 1999; Strow et al. 2003; Wei et al. 2004; Dubuisson et al. 2005; Wang et al. 2011; Wang et al. 2013a; Niu et al. 2007; Zhang et al. 2007), the forward radiance simulations in the IR spectral region are relatively straightforward compared with those in the visible through shortwave infrared (VIS/SWIR) regimes ($0.4\ \mu m < \lambda < 2.5\ \mu m$). For example, the sources of IR radiances, including thermal emission from the surface,

* Reprinted with permission from "A fast radiative transfer model for visible through shortwave infrared spectral reflectances in clear and cloudy atmospheres" by C. Wang, P. Yang, S. L. Nasiri, S. Platnick, B. A. Baum, A. K. Heidinger, and X. Liu, 2013. *Journal of Quantitative Spectroscopy & Radiative Transfer*, 116, 122-131, doi:10.1016/j.jqsrt/2012.10.012 Copyright by Elsevier

atmosphere, cloud, and aerosol layers, do not show significant angular dependence, and the limited impact of the anisotropic feature of surface reflection can be ignored due to the small albedo (Wan and Li 1997; Ruston et al. 2008). Additionally, both cloud and aerosol particles absorb more energy in the IR spectral region (Hele and Querry 1973; Warren and Brandt 2008; Sokolik et al. 1993; Volz 1972; Levoni et al. 1997) than in the VIS/SWIR spectral region mitigating relatively complicated scattering effects. In the VIS/SWIR region, however, the "quasi-isotropic" feature of radiance vanishes because of multiple scattering processes within the cloud/aerosol layers and with non-Lambertian surface reflection. Furthermore, the primary radiation source within the VIS/SWIR spectral region is solar radiation, giving rise to an azimuthal angular dependence of the radiance that is caused partially by the quasi-collimated direct solar beam. Consideration of both gaseous absorption and Rayleigh scattering effects makes the implementation of numerical simulation more difficult. If the cloud or aerosol layer is opaque, several of the well-known RTMs (Stamnes et al. 1988; Collins et al. 1972; Plass and Kattawar 1968; Twomey et al. 1966; Hansen and Hovenier 1971a), which deal with the multiple scattering in the cloud and aerosol layers and reflective non-Lambertian surfaces require significant computational effort to simulate the radiance.

A number of challenges exist in the accurate forward simulation of non-clear sky top of the atmosphere (TOA) radiance in the VIS/SWIR spectral region. First, the forward radiance simulator requires information about the cloud/aerosol layer, such as geometric height/thickness and optical/microphysical properties, and the atmospheric state, including the temperature, pressure, and humidity profiles. Modern satellite

operational products and their corresponding algorithms use a variety of approaches to infer cloud and aerosol layer geometries (Platnick et al. 2003; Winker et al. 2009; Vaughan et al. 2009; Menzel et al. 1983), ambient temperature, pressure, and humidity (Rodgers 1976; Kuo et al. 1994). A number of reanalysis products, such as the National Centers for Environmental Prediction/Global Data Assimilation System (NCEP/GDAS, Derber et al. 1991) and the NASA Global Modeling and Assimilation Office/Modern Era Retrospective-analysis for Research and Applications (GMAO/MERRA, Rienecker et al. 2008), provide near real-time meteorological data that facilitate the forward simulation.

Second, the bidirectional reflectance distribution function (BRDF) of a non-Lambertian surface is needed. The Moderate Resolution Imaging Spectroradiometer (MODIS) operational land surface product (MCD43) provides a series of parameters associated with a forward BRDF model (Lucht et al. 2000; Schaaf et al. 2002) to reveal the directional variance of surface reflectance (Ross 1981; Li and Strahler 1992). The surface BRDF over the ocean, largely determined by the surface wind speed (Cox and Munk 1954), can also be simulated. The BRDF models for both ocean and land surfaces are well developed and have been validated using satellite-based and in-situ measurements (Salomon et al. 2006). However, the Lambertian surface assumption is still widely used in current satellite-based cloud retrieval algorithms, such as the ones for MODIS Collection 5 (King et al. 1997), the Spinning Enhanced Visible and Infrared Imager (SEVIRI), and the Advanced Very High Resolution Radiometer (AVHRR) (Meirink et al. 2010).

Although many rigorous radiative transfer schemes, such as the adding-doubling (AD) algorithm (Twomey et al. 1966; Hansen and Hovenier 1971a) and the discrete ordinates radiative transfer (DISORT) method (Stamnes et al. 1988), have been developed, they require substantial computational effort and are impractical for global satellite remote sensing applications. Thus, it is critical to develop computationally efficient RTM capabilities. In this paper, a computationally stable and efficient AD algorithm is explored that is designed to solve approximately the problem of radiation transfer in scattering and absorbing media (thermal emission is omitted for simplification) above an arbitrary non-Lambertian surface. Two novel features of this algorithm are in its treatment of Rayleigh scattering and an arbitrary number of cloud/aerosol layers and the associated solid angle integration.

To consider separately both the impact of Rayleigh scattering and the cloud/aerosol layers, we divided the full radiative transfer equation (RTE) into six independent sub-equations (Ambartzumian 1958; Wang and King 1997). The total effect of multiple cloud/aerosol layers is solved numerically using the AD algorithm. The AD algorithm is known to be accompanied by a time consuming integration process over a conjunct solid angle associated with the two adjacent scattering and absorptive layers with the resulting integral known as “star products” (Liou 2002; Wendisch and Yang 2012). One traditional solution is to calculate numerically the integral with a constant zenith-azimuth (select constant values for zenith and azimuth angles) discretization scheme (Mobley 1994). The use of this discretization scheme in a fast RTM is inappropriate for two reasons. First, the radiance simulations slow down computationally

in the zenith (or nadir) direction, i.e., the zenith angle cosine is near 1 (or -1), where the variation of BRDF is not significant. Second, the discrete solid angles in the region where the zenith angle cosine is near zero (i.e., "equator region") are larger than those in the zenith/nadir region with the regular discretization scheme. However, the BRDF always contains obvious variations in the "equator region", and, as a result, the numerical integration can lose significant accuracy. While we note that some AD codes have chosen to circumvent this loss of accuracy by using a constant cosine of zenith angle discretization (i.e., equal solid angle, Twomey et al 1966), we have instead selected a twisted icosahedral grid (Heikes and Randall 1995a) to calculate the integral efficiently.

The remainder of this paper is organized with the Atmosphere-Cloud/Aerosol-Surface system described in Section 2.2; the analytical solutions of the independent RTEs briefly presented in Section 2.3; the numerical approach for reducing the computational burden is introduced in Section 2.4; and, the validation and summary are discussed in Sections 2.5 and 2.6, respectively.

2.2 Scheme of the model

To take advantage of the well-accepted AD technique, the RTE solver is designed for a plane-parallel and vertically inhomogeneous medium above a reflective lower boundary. Specifically, the background consists of two clear layers without cloud or aerosol particles, and a "non-clear" layer containing multiple consecutive cloud or aerosol layers (Fig 2.1), each of which is assumed to contain a homogeneous absorbing and/or scattering medium such that the spectral single-scattering albedo and phase

functions are constant. The Rayleigh scattering between any two consecutive cloud/aerosol layers is neglected for simplicity. The extinction caused by the clear-sky layer between the surface and the lowermost cloud/aerosol layer must be considered due to the non-negligible effects of water vapor and other gases. The sea-level Rayleigh optical thickness is generally smaller than 0.1 (Bodhaine et al. 1999) in the spectral regions (0.55, 0.66, 0.87, and beyond 1.0-μm) primarily used to study surface, cloud, and aerosol properties. Consequently, the Rayleigh scattering can be accounted for based on a single-scattering approximation (Wang and King 1997), meaning that only one scattering event between a single photon and an air molecule is assumed for all the clear layers in the column. A weakness of this approximation can be found for some cases, such as a high cirrus cloud over a low water cloud layer. Further study is required to efficiently take into account the Rayleigh scattering between consecutive non-clear layers.

Following the derivation of principles of invariance (Ambartzumian 1958) and the Rayleigh scattering correction technique (Wang and King 1997), we separate the complicated process into six independent events (Fig. 2.2). Photons are: (a) backward scattered by gas molecules within the upper clear layer; (b) first scattered by the upper clear layer and then reflected by the non-clear layer; (c) reflected by the non-clear layer and then scattered back toward the viewing direction by gas molecules; (d) directly reflected by the non-clear layer; (e) scattered by the lower gas molecules; and, (f) reflected due to the Rayleigh scattering occurring in the lower layer and then diffusely transmitted to the non-clear layer. The satellite-observed TOA bidirectional reflectance

(R_{TOA}) contributed by the six events can be expressed as the summation of the six individual parts.

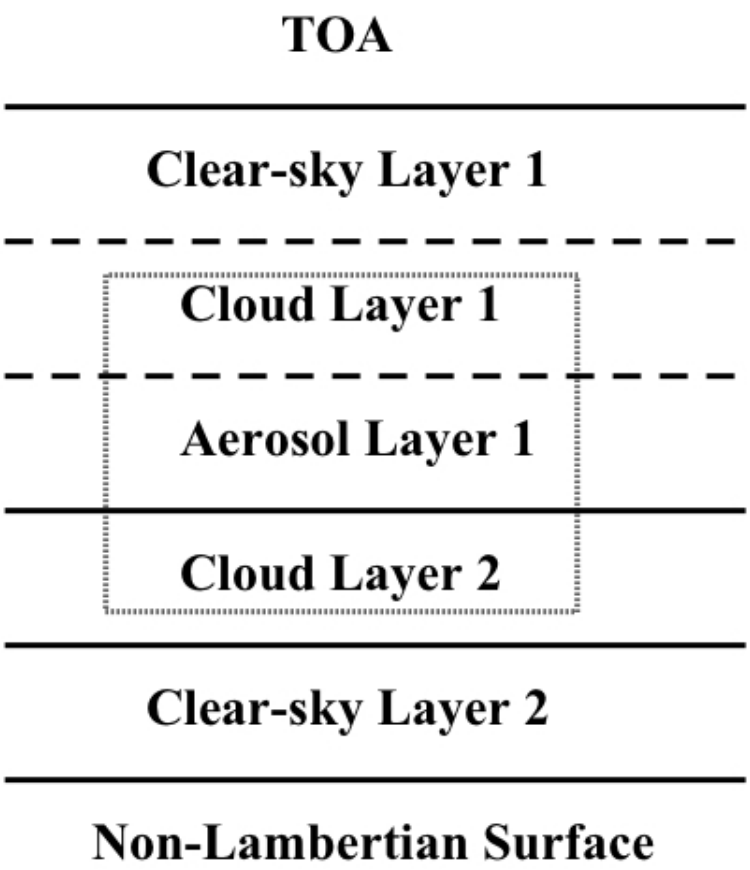

Fig.2.1 Illustrative diagram of a plane-parallel atmosphere consisting of two clear layers, multiple cloud/aerosol layers, and a non-Lambertian surface.

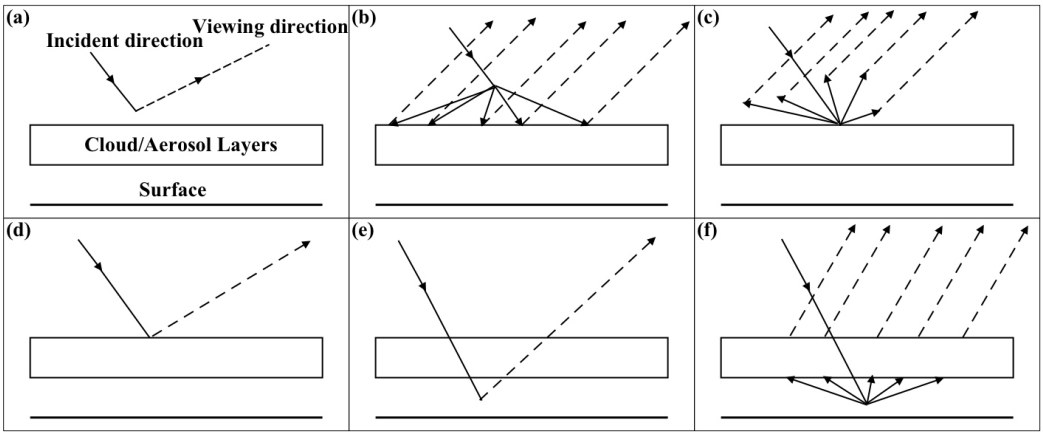

Fig.2.2 Six possible paths of photons transferred within the atmosphere-cloud/aerosol system. Photons are: (a) backward scattered by air molecules of the upper clear layer; (b) forward scattered by the upper clear layer and then reflected by the non-clear layer; (c) reflected by the non-clear layer and then scattered back toward the viewing direction due to the Rayleigh scattering; (d) directly reflected by the non-clear layer; (e) scattered by the air molecules within in the lower layer (no interaction with the non-clear layer); and, (f) reflected due to the Rayleigh scattering occurring in the lower layer and then diffusely transmitted to the non-clear layer. The dashed lines indicate the reflected radiation in the direction of satellite-based instrument.

2.3 Analytical solution

To specify the geometry of the incident solar beam and the viewing direction, the TOA radiance contributed by each of the six independent parts can be derived by solving six individual RTEs with different boundary conditions and can be expressed in terms of bidirectional reflectance functions. The definition of bidirectional reflectance is in the form:

$$R(\mu_v,\varphi_v,-\mu_i,\varphi_i)=\frac{\pi I(0,\mu_v,\varphi_v)}{\mu_i F_0}, \tag{2.1}$$

where μ is the cosine of zenith angle, φ is the azimuth angle, F_0 is the incident solar irradiance at the TOA, and the subscripts i and v indicate the incident and viewing directions. The spectral dependence is implied. The six bidirectional reflectance functions can be expressed as follows:

$$R_I = \frac{\omega_u P_{-iv}}{4(\mu_i + \mu_v)}[1 - \exp(\frac{-\tau_u(\mu_i + \mu_v)}{\mu_i \mu_v})], \tag{2.2a}$$

$$R_{II} = \frac{\omega_u}{4\pi}\exp(-\frac{\tau_u}{\mu_v})\int_0^{2\pi}\int_0^1 \frac{\mu'}{\mu' - \mu_i} P_{ij} R_{jv}[\exp(\frac{-\tau_u}{\mu'}) - \exp(\frac{-\tau_u}{\mu_i})]d\mu' d\varphi', \tag{2.2b}$$

$$R_{III} = \frac{\omega_u}{4\pi\mu_v}\exp(-\frac{\tau_u}{\mu_i})\int_0^{2\pi}\int_0^1 \frac{\mu'\mu_v}{\mu' - \mu_v} R_{ij} P_{jv}[\exp(\frac{-\tau_u}{\mu'}) - \exp(\frac{-\tau_u}{\mu_v})]d\mu' d\varphi', \tag{2.2c}$$

$$R_{IV} = \exp(-\frac{\tau_u}{\mu_i})\exp(-\frac{\tau_u}{\mu_v})R_{iv}, \tag{2.2d}$$

$$R_V = \frac{\omega_l P_{-iv}}{4(\mu_i + \mu_v)}\exp[-\frac{\mu_i + \mu_v}{\mu_i \mu_v}(\tau_c + \tau_u)][1 - \exp(-\frac{\mu_i + \mu_v}{\mu_i \mu_v}\tau_l)], \tag{2.2e}$$

$$R_{VI} = \frac{\omega_l}{4\pi}\exp(-\frac{\tau_c + \tau_u}{\mu_i})\exp(-\frac{\tau_u}{\mu_v})\int_0^{2\pi}\int_0^1 \frac{\mu'}{\mu_i + \mu'} P_{-ij} T_{jv} d\mu' d\varphi', \tag{2.2f}$$

where the subscript j is associated with μ' and φ'; τ_u, τ_l, and τ_c correspond to the extinction optical thickness of the upper clear layer, lower clear layer, and the total effect of non-clear layer (i.e., consisting of consecutive cloud/aerosol layers), respectively; and ω_u and ω_l are the single-scattering albedo values of the upper and lower clear layers. Under the assumption that energy is conserved during the Rayleigh scattering process, the single-scattering albedo of a clear layer can be expressed as:

$$\omega = \frac{\tau_R}{\tau_R + \tau_a}, \tag{2.3}$$

where τ_R and τ_a indicate the Rayleigh and absorption optical thicknesses. Consequently, the denominator of Eq. 2.3 is essentially the extinction optical thickness of a clear layer, while P, R, and T, respectively, represent the Rayleigh phase function, the bidirectional reflectance, and transmittance (diffuse) function of the non-clear layer. The two subscripts associated with each of P, R, T functions specify the incoming direction (the former) and the outgoing direction (the latter). Additionally, a negative sign before the two subscripts of P indicates that the signs of the incoming and outgoing zenith angle cosines are different.

The BRDF of a cloud (or aerosol)-surface system (R_{cs}) or cloud-cloud (or aerosol) system (R_{cc}) and the bidirectional transmittance distribution function (BTDF) of a cloud-cloud (T_{cc}) system are necessary to derive Eq. 2.2(b) ~ Eq. 2.2(f). In the rigorous AD algorithm (Twomey et al. 1966; Hansen and Hovenier 1971a), the R and T functions of a single layer cloud/aerosol are numerically computed with the so-called doubling process. This process starts with a cloud/aerosol layer with an infinitesimal optical thickness (e.g., $\tau \sim 10^{-8}$ in numerical calculation) so that the single-scattering approximation can be applied. However, it is time-consuming if the cloud/aerosol layer is not optically thin. In this study, the computational burden resulting from the doubling process is alleviated by using a set of pre-computed R and T lookup tables (LUTs) for single homogeneous cloud or aerosol layers (Zhang et al. 2007). The AD method (although the doubling process is avoided, we will continue to use the AD term for convention) is employed to simulate R and T functions of the non-clear layer and the reflective non-Lambertian surface.

The cloud-surface system is illustrated in Fig. 2.3. As mentioned in Section 2.2, the absorptive gases within the clear layer between the surface and cloud lower boundary need to be taken into account. The first-order Rayleigh scattering has been included in the fifth and sixth independent events (shown in Figs. 2.2e and 2.2f). As shown in Fig. 2.3, the optical thicknesses of the non-clear layer and clear layer are τ_c and $\tau_{a,}$ while R_c and T_c indicate the BRDF and BTDF of the non-clear layer. The nth order of radiance reflected by the cloud-surface system is $I_{ref\text{-}n}$. The total reflected intensity, I_{ref}, is expressed as the summation of all the orders. If we define a star product operator (Liou 2002) as:

$$X(\mu,\varphi) * Y(\mu,\varphi) = \frac{1}{\pi}\int_0^{2\pi}\int_0^1 X(\mu,\varphi)Y(\mu,\varphi)\mu d\mu d\varphi, \tag{2.4}$$

where X and Y are two arbitrary functions of μ and φ, then the first three orders of intensity are given by:

$$I_{ref-1} = I_{inc,i} * R_{iv}, \tag{2.5a}$$

$$I_{ref-2} = I_{inc,i} * (T_{c,ij} + \delta_{ij} t_{c,j}) * t_{a,j} R_{s,jk} t_{a,k} * (T_{c,kv} + \delta_{kv} t_{c,v}), \tag{2.5b}$$

$$I_{ref-3} = I_{inc,i} * (T_{c,ij} + \delta_{ij} t_{c,j}) * t_{a,j} R_{s,jk} t_{a,k} * R_{c,kl} t_{a,l} * R_{s,lm} t_{a,m} * (T_{c,mv} + \delta_{mv} t_{c,v}), \tag{2.5c}$$

where the subscripts i, j, k, l, m, and v indicate the direction of incident or reflected (transmitted) radiance. For example, $T_{c,ij}$ indicates the BTDF for a situation in which the incident radiance towards direction i is scattered by the cloud/aerosol particles and eventually transmitted out of the layer towards direction j. $I_{inc,i}$ is the incident radiance towards the directions, i, $t_{c,j}$, and $t_{a,j}$, and defined as follows:

$$t_{c,j} = \exp(-\frac{\tau_c}{\mu_j}), \tag{2.6a}$$

$$t_{a,j} = \exp(-\frac{\tau_a}{\mu_j}), \tag{2.6b}$$

which are the direct transmittance functions of the non-clear and clear layers. δ_{ij} is the Kronecker delta defined as:

$$\delta_{ij} = \begin{cases} 1, & i = j \\ 0, & i \neq j \end{cases}. \tag{2.7}$$

With the definition of bidirectional reflectance, Eq. 1, $R_{cs,iv}$ can be given by:

$$R_{cs,iv} = R_{c,iv} + (T_{c,ij} + \delta_{ij} t_{c,j}) * U_{cs,jp} * (T_{c,pv} + \delta_{pv} t_{c,v}), \tag{2.8}$$

where $U_{cs,jp}$ is defined as:

$$\begin{aligned} U_{cs,jp} = {} & t_{a,j} R_{s,jp} t_{a,p} + \\ & t_{a,j} R_{s,jk} t_{a,k} * R_{c,kl} t_{a,l} * R_{s,lp} t_{a,p} + \\ & t_{a,j} R_{s,jk} t_{a,k} * R_{c,kl} t_{a,l} * R_{s,lm} t_{a,m} * R_{c,mn} t_{a,n} * R_{s,np} t_{a,p} + \\ & \ldots \end{aligned}. \tag{2.9}$$

The cloud-cloud system is essentially the same as the cloud-surface combination. In a like manner, $R_{cc,iv}$ and $T_{cc,iv}$ can be expressed as:

$$R_{cc,iv} = R_{1,iv} + (T_{1,ik} + \delta_{ik} t_{1,k}) * U_{cc,kp} * (T_{1,pv} + \delta_{pv} t_{1,v}), \tag{2.10}$$

$$\begin{aligned} T_{cc,ij} = {} & T_{1,ik} * t_{a,k} T_{2,kj} + T_{1,ij} t_{a,j} t_{2,j} + t_{1,i} t_{a,i} T_{2,ij} + \\ & (T_{1,ik} + \delta_{ik} t_{1,k}) * D_{cc,kq} * (T_{2,qj} + \delta_{qj} t_{2,j}) \end{aligned}, \tag{2.11}$$

and $U_{cc,kp}$ and $D_{cc,kq}$ are defined as:

$$
\begin{aligned}
U_{cc,kp} = & t_{a,k} R_{2,kp} t_{a,p} + \\
& t_{a,k} R_{2,kl} t_{a,l} * R_{1,lm} t_{a,m} * R_{2,mp} t_{a,p} + \\
& t_{a,k} R_{2,kl} t_{a,l} * R_{1,lm} t_{a,m} * R_{2,mn} t_{a,n} * R_{1,no} t_{a,o} * R_{2,op} t_{a,p} + \\
& \ldots
\end{aligned}
\qquad (2.12)
$$

$$
\begin{aligned}
D_{cc,kq} = & t_{a,k} R_{2,kl} t_{a,l} * R_{1,lq} t_{a,q} + \\
& t_{a,k} R_{2,kl} t_{a,l} * R_{1,lm} t_{a,m} * R_{2,mn} t_{a,n} * R_{1,nq} t_{a,q} + \\
& t_{a,k} R_{2,kl} t_{a,l} * R_{1,lm} t_{a,m} * R_{2,mn} t_{a,n} * R_{1,no} t_{a,o} * R_{2,op} t_{a,p} * R_{1,pq} t_{a,q} + \ldots
\end{aligned}
\qquad (2.13)
$$

where the subscripts *1* and *2* indicate the upper and lower cloud/aerosol layers. Note that t_a indicates the transmittance function between the two non-clear layers.

2.4 Numerical solution

In the previous section, we derived a generally applicable solution of the TOA bidirectional reflection. However, to achieve a rapid and accurate model for operational applications, we need an appropriate way to select the quadrature points and weights of the spherical solid angle integration shown in Eq. 2.4. With a simple discretization scheme, the integral could be easily calculated on a grid with constant zenith angle and azimuth angle intervals (Mobley 1994). However, several problems arise associated with a regular zenith-azimuth discretization scheme. For example, the area of differential element rapidly decreases towards the zenith. As a result, the numerical integration based on this grid scheme increases the computational burden in the pole region (i.e., μ is close to 1), and decreases the accuracy near the equator (i.e., μ is close to 0).

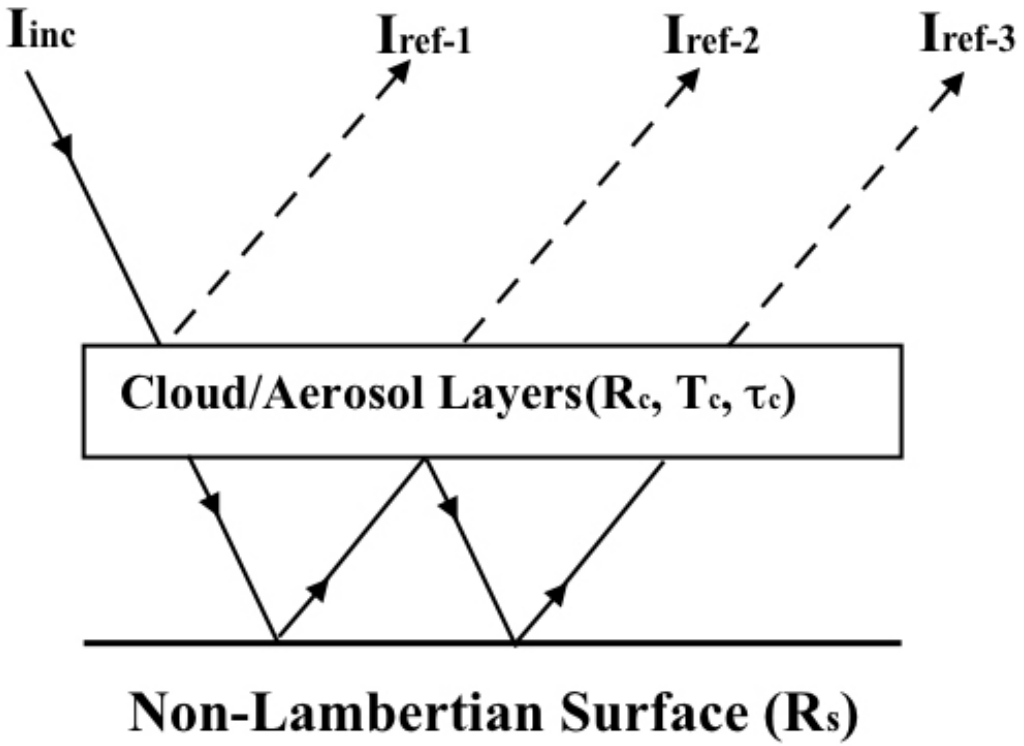

Fig.2.3 Illustrative diagram of the adding algorithm applied to the cloud/aerosol and non-Lambertian surface system.

Various studies have focused on the approaches of discretization on a sphere (Stuhne and Peltier 1999; Górski et al. 2005), and many of these methods have already been applied in numerical models (Heikes and Randall 1995b). In this study, we conduct the numerical calculation on a twisted icosahedral grid (Fig. 2.4), which has been successively utilized to numerically calculate the shallow-water equations in the atmospheric general circulation model (AGCM, Heikes and Randall 1995b) developed

by Colorado State University. The primary advantages of a twisted icosahedral grid are: (1) The elemental triangles have similar areas and shapes, which stabilizes the accuracy of the numerical integration; and, (2) The grid is symmetric with respect to the "equator" (i.e., none of the elemental triangles spans the "equator"), (3) This discretization scheme does not use a Fourier cosine series to factor out the azimuth dependence (Stamnes et al. 1988; Chandrasekhar 1960). These features simplify the adding processes; however, one must be very careful in generating the BRDF/BTDF database of cloud/aerosol layers on a twisted icosahedral gird due to the significant forward peak of the particle phase function resulting from diffraction.

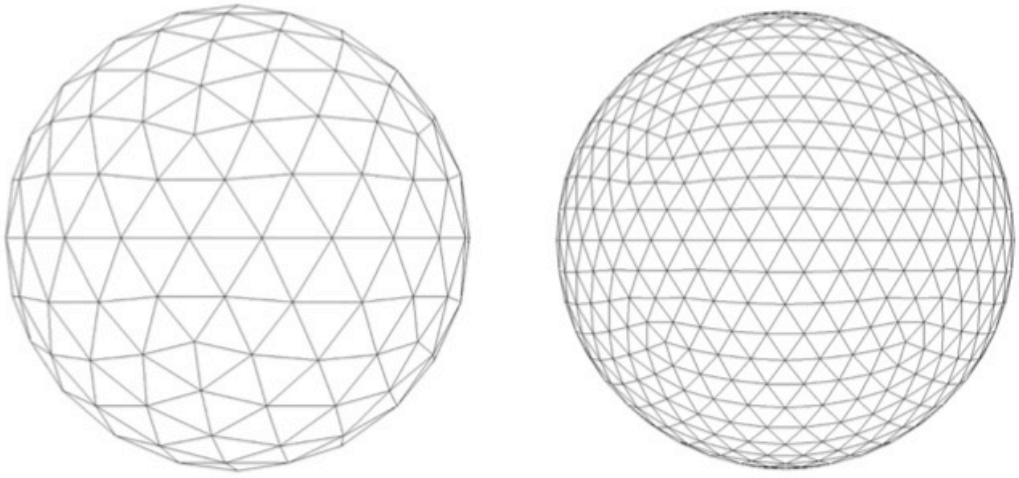

Fig.2.4 Twisted icosahedrons inscribed in unit spherical surfaces. Left panel: 320 small triangles. Right panel: 1280 small triangles.

Many numerical methods (Wiscombe 1977; Hu et al. 2000) have been developed to mitigate the effect of the strong forward peak so that the phase function can be approximated as a summation of Legendre Polynomials with limited terms. However, the truncated phase functions (especially for large particles) in the forward directions (e.g., scattering angle < 5°) are larger than those in the semi-forward directions (e.g., 5° < scattering angle < 10°, Hu et al. 2000). For this reason, in addition to using the delta-fit method (Hu et al. 2000) to truncate the phase function in the generation of both transmittance and reflectance LUTs, we continually refine the elemental triangles in the forward directions when calculating the diffuse transmittance LUTs. The use of icosahedral grid makes this step easy. Specifically, the triangles in the forward directions (i.e., scattering angle < 5°) are first divided into 16 or 64 sub-triangles with approximately the same area and then projected onto the spherical surface (see Fig. 2.5). The diffuse transmittance function in the forward direction is the average of the 16 or 64 transmittance functions calculated in the normal directions of the re-projected sub-triangles.

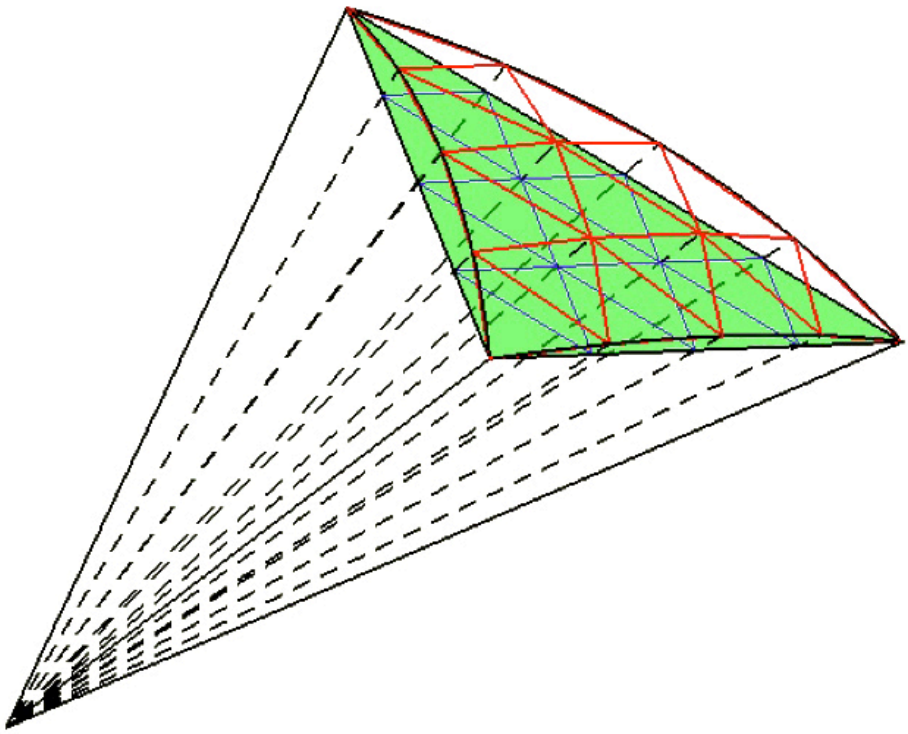

Fig.2.5 An example of dividing a triangle into 16 small triangles, which are continually projected onto the spherical surface.

In accordance with the order of six independent events, we successively give their contributions to the TOA bidirectional reflectance in the form of numerical solutions. Assume that a twisted icosahedron has 2N elemental facets, half of which are located in the upward hemisphere. The area of the *n*th facet in the upward hemisphere is A_n. The surface area of the upward hemisphere is then given by:

$$S = \sum_{n=1}^{N} A_n \,. \tag{2.14}$$

The numerical forms of R_I to R_{VI} shown in Eq. 2.2 can be expressed as:

$$R_I = \frac{\omega_u P_{-iv}}{4(\mu_i + \mu_v)}\left[1 - \exp(-c\tau_u)\right], \tag{2.15a}$$

$$R_{II} = \frac{\omega_u}{2S} t_{u,v}\left[\sum_{\substack{j=1 \\ \mu_j \neq \mu_i}}^{N} \left(\frac{\mu_j}{\mu_j - \mu_i}\right) P_{ij} R_{jv} A_j (t_{u,j} - t_{u,i}) + \lim_{\mu_j \to \mu_i} \left(\frac{\tau_u}{\mu_j} P_{ij} R_{jv} A_j t_{u,j}\right)\right], \tag{2.15b}$$

$$R_{III} = \frac{\omega_u}{2S\mu_v} t_{u,i}\left[\sum_{\substack{j=1 \\ \mu_j \neq \mu_v}}^{N} \left(\frac{\mu_j \mu_v}{\mu_j - \mu_v}\right) R_{ij} P_{jv} A_j (t_{u,j} - t_{u,v}) + \lim_{\mu_j \to \mu_v} \left(\tau_u P_{ij} R_{jv} A_j t_{u,j}\right)\right], \tag{2.15c}$$

$$R_{IV} = t_{u,i} t_{u,v} R_{iv}, \tag{2.15d}$$

$$R_V = \frac{\omega_l P_{-iv}}{4(\mu_i + \mu_v)} \exp[-c(\tau_c + \tau_u)]\left[1 - \exp(-c\tau_l)\right], \tag{2.15e}$$

$$R_{VI} = \frac{\omega_l}{2S} t_{cu,i} t_{u,v} \sum_{j=1}^{N} \frac{\mu_j}{\mu_i + \mu_j} P_{-ji} T_{jv} A_j, \tag{2.15f}$$

where c is a coefficient defined as:

$$c = \frac{\mu_i + \mu_v}{\mu_i \mu_v}, \tag{2.16}$$

and $t_{cu,i}$ is the direct transmittance function:

$$t_{cu,i} = \exp\left(-\frac{\tau_u + \tau_c}{\mu_i}\right). \tag{2.17}$$

The BRDF or BTDF of a cloud/aerosol layer or surface can be simply expressed in the form of N×N matrices, e.g., $\mathbf{R}_c$, $\mathbf{T}_c$, and $\mathbf{R}_s$. Hence, $R_{s,jk}$ shown in Eq. 2.5

represents the element at the *j*th row and *k*th column of matrix $\mathbf{R}_s$. Additionally, the star product can be rewritten as:

$$X(\mu,\varphi) * Y(\mu,\varphi) = f\sum_{i=1}^{N} X_i Y_i \mu_i A_i, \tag{2.18}$$

where *f* is a normalization factor defined as:

$$f = \frac{2}{\sum_{i=1}^{N} A_i} = \frac{2}{S}. \tag{2.19}$$

Through using matrix multiplication and Eq. 18, we conclude that the star product of two bidirectional reflectance matrices, e.g., $\mathbf{R}_c$ and $\mathbf{R}_s$, can be expressed as:

$$\mathbf{R}_c * \mathbf{R}_s = f\overline{\mathbf{R}}_c \mathbf{R}_s. \tag{2.20}$$

The definition of the notation "bar" is

$$\overline{\mathbf{R}} = \begin{bmatrix} R_{11}A_1\mu_1 & R_{12}A_2\mu_2 & \dots & R_{1N}A_N\mu_N \\ R_{21}A_1\mu_1 & \vdots & \vdots & \vdots \\ \vdots & \vdots & \vdots & \vdots \\ R_{N1}A_1\mu_1 & \dots & \dots & R_{NN}A_N\mu_N \end{bmatrix}. \tag{2.21}$$

Therefore, $\mathbf{U}_{cs}$ in Eq. 9 can be expressed as:

$$\mathbf{U}_{cs} = \mathbf{R}_{gsg} + f^2\overline{\mathbf{R}}_{gsg}\mathbf{V}_{cs} + f^4\overline{\mathbf{R}}_{gsg}(\overline{\mathbf{V}}_{cs}\mathbf{V}_{cs}) + \cdots, \tag{2.22}$$

$$\mathbf{V}_{cs} = \overline{\mathbf{R}}_{cg}\mathbf{R}_{sg}, \tag{2.23}$$

where the matrices $\mathbf{R}_{gsg}$, $\mathbf{R}_{cg}$, and $\mathbf{R}_{sg}$ are defined as follows:

$$\mathbf{R}_{gsg} = \begin{bmatrix} t_{a,1}R_{s,11}t_{a,1} & t_{a,1}R_{s,12}t_{a,2} & \dots & t_{a,1}R_{s,1N}t_{a,N} \\ t_{a,2}R_{s,21}t_{a,1} & \vdots & \vdots & \vdots \\ \vdots & \vdots & \vdots & \vdots \\ t_{a,N}R_{s,N1}t_{a,1} & \dots & \dots & t_{a,N}R_{s,NN}t_{a,N} \end{bmatrix}, \tag{2.24a}$$

$$\mathbf{R}_{cg} = \begin{bmatrix} R_{c,11}t_{a,1} & R_{c,12}t_{a,2} & \ldots & R_{c,1N}t_{a,N} \\ R_{c,21}t_{a,1} & : & : & : \\ : & : & : & : \\ R_{c,N1}t_{a,1} & \ldots & \ldots & R_{c,NN}t_{a,N} \end{bmatrix}, \tag{2.24b}$$

$$\mathbf{R}_{sg} = \begin{bmatrix} R_{s,11}t_{a,1} & R_{s,12}t_{a,2} & \ldots & R_{s,1N}t_{a,N} \\ R_{s,21}t_{a,1} & : & : & : \\ : & : & : & : \\ R_{s,N1}t_{a,1} & \ldots & : & R_{s,NN}t_{a,N} \end{bmatrix}. \tag{2.24c}$$

Hence, based on Eq. 2.20, we can replace the formulation of the bidirectional reflectance of the cloud-surface system shown in Eq. 2.8 by the following equations:

$$\mathbf{R}_{cs} = \mathbf{R}_c + f^2\overline{\mathbf{T}}_c\mathbf{W}_{cs} + f\mathbf{X}_{cs} + \mathbf{Y}_{cs}, \tag{2.25a}$$

$$\mathbf{W}_{cs} = \overline{\mathbf{U}}_{cs}\mathbf{T}_c, \tag{2.25b}$$

$$\mathbf{W}'_{cs} = \overline{\mathbf{T}}_c\mathbf{U}_{cs}. \tag{2.25c}$$

$\mathbf{X}_{cs}$ is a symmetric matrix whose entries can be generally expressed as:

$$X_{cs,ij} = W_{cs,ij}t_{c,i} + W'_{cs,ij}t_{c,j}, \tag{2.25d}$$

and the general expression of entries of matrix $\mathbf{Y}_{cs}$ is

$$Y_{cs,ij} = t_{c,i}U_{cs,ij}t_{c,j}. \tag{2.25e}$$

Similarly, the bi-directional reflectance matrix $\mathbf{R}_{cc}$ for a cloud-cloud system is given by

$$\mathbf{R}_{cc} = \mathbf{R}_1 + f^2\overline{\mathbf{T}}_1\mathbf{W}_{cc} + f\mathbf{X}_{cc} + \mathbf{Y}_{cc}, \tag{2.26a}$$

where

$$\mathbf{W}_{cc} = \overline{\mathbf{U}}_{cc}\mathbf{T}_1, \tag{2.26b}$$

$$\mathbf{W}'_{cc} = \overline{\mathbf{T}}_1\mathbf{U}_{cc}, \tag{2.26c}$$

$$X_{cc,ij} = W_{cc,ij}t_{1,i} + W'_{cc,ji}t_{1,j}, \tag{2.26d}$$

$$Y_{cc,ij} = t_{1,i} U_{cc,ij} t_{1,j}, \tag{2.26e}$$

$$\mathbf{U}_{cc} = \mathbf{R}_{g2g} + f^2 \overline{\mathbf{R}}_{g2g} \mathbf{V}_{cc} + f^4 \overline{\mathbf{R}}_{g2g} (\overline{\mathbf{V}}_{cc} \mathbf{V}_{cc}) + ..., \tag{2.26f}$$

$$\mathbf{V}_{cc} = \overline{\mathbf{R}}_{1g} \mathbf{R}_{2g}, \tag{2.26g}$$

and the corresponding bidirectional transmittance matrix $\mathbf{T}_{cc}$ is given by

$$\mathbf{T}_{cc} = f^2 \overline{\mathbf{T}}_1 \mathbf{E}_{cc} + f(\overline{\mathbf{T}}_1 \mathbf{T}_2 + \mathbf{G}_{cc}) + \mathbf{H}_{cc}, \tag{2.27a}$$

where

$$\mathbf{E}_{cc} = \overline{\mathbf{D}}_{cc} \mathbf{T}_2, \tag{2.27b}$$

$$\mathbf{D}_{cc} = f\mathbf{V}'_{cc} + f^3 \overline{\mathbf{V}'_{cc}} \mathbf{V}'_{cc} + f^5 [\overline{\mathbf{V}'_{cc}} (\overline{\mathbf{V}'_{cc}} \mathbf{V}'_{cc})] + ..., \tag{2.27c}$$

$$\mathbf{V}'_{cc} = \overline{\mathbf{R}}_{g2g} \mathbf{R}_{1g}, \tag{2.27d}$$

$$G_{cc,ij} = E_{cc,ij} t_{1,i} + F_{cc,ij} t_{2,j}, \tag{2.27e}$$

$$\mathbf{F}_{cc} = \overline{\mathbf{T}}_1 \mathbf{D}_{cc}, \tag{2.27f}$$

$$H_{cc,ij} = t_{1,i} D_{cc,ij} t_{2,j} + T_{1,ij} t_{a,j} t_{2,j} + t_{1,i} t_{a,i} T_{2,ij}. \tag{2.27g}$$

Note that the definitions of $\mathbf{R}_{1g}$, $\mathbf{R}_{2g}$, and $\mathbf{R}_{g2g}$ are similar to those $\mathbf{R}_{cg}$, $\mathbf{R}_{sg}$, and $\mathbf{R}_{gsg}$, shown in Eqs. 2.24a, 2.24b, and 2.24c. Generally, the entries in $\mathbf{U}_{cs}$, $\mathbf{U}_{cc}$, and $\mathbf{D}_{cc}$ rapidly converge if the first and second orders of reflected radiance are considered (i.e., consider the first two terms of the right-hand sides of Eqs. 2.9, 2.12 and 2.13). A simple exponential interpolation method is used to calculate the BRDF of cloud-surface system at user defined viewing zenith angles (VZA).

2.5 Model validation

To validate, we implement a set of comparisons between the newly developed fast RTM and a benchmark model, DISORT run using 128 streams, with respect to both

the model accuracy and computational efficiency. We compare the TOA reflectance simulations obtained by both models for two scenes: 1) a single ice cloud layer and 2) overlapped ice cloud layers. The ice cloud microphysical (Baum et al. 2005a) and optical properties (Baum et al. 2005b; Yang et al. 2000; Zhang et al. 2004) employed in the comparison are the same as those used in the current operational MODIS Collection 5 algorithm. The pre-computed ice cloud bidirectional reflectance database is generated on the twisted icosahedral grid with 320 elemental facets (i.e., N = 160 in Eq. 2.14).

Fig. 2.6 shows the relative errors of the fast model simulated TOA BRDFs at 0.64 μm as functions of the VZA for the background, which includes a single ice cloud layer and a reflective non-Lambertian surface. The dependence of the relative error on the solar zenith angle (SZA) is demonstrated by using solid, dotted, and dashed lines to give the relative errors in small (10°), medium (35°), and large (50°) SZA situations. The cloud effective radius (R_{eff}, half of D_{eff}) is 25 μm.

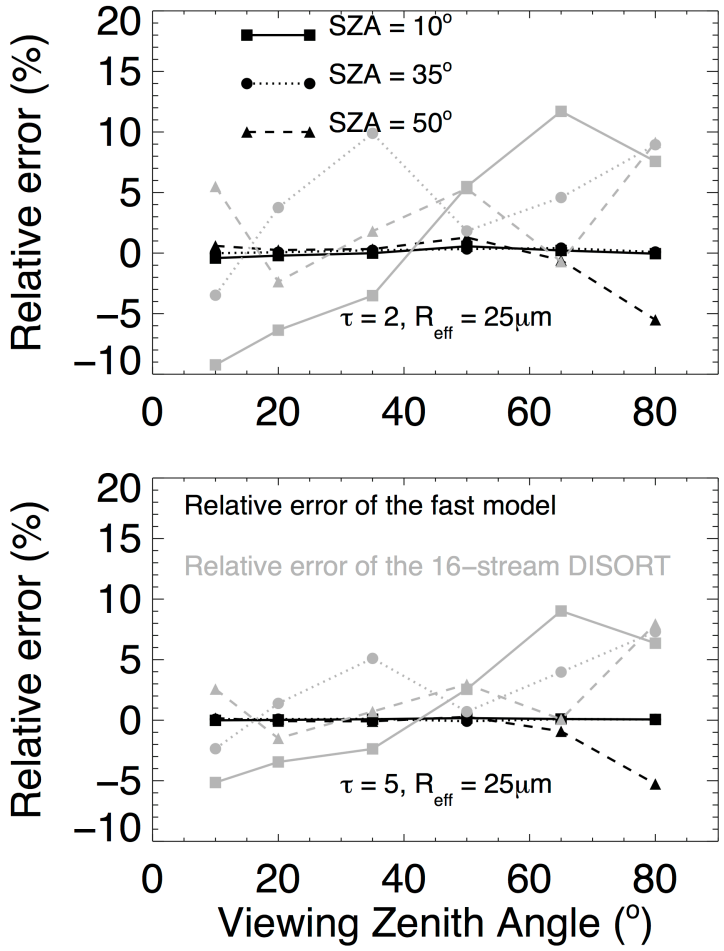

Fig.2.6 Relative errors of TOA BRDFs at 0.64-μm simulated by the fast model (black) and the 16-stream DISORT (gray) in comparison with the benchmark model (i.e., DISORT with 128-stream). Single ice cloud layer and a non-Lambertian surface are considered. Three SZA values, 10, 35, and 50, are employed and their corresponding results are demonstrated using solid lines, dotted lines, and dashed lines. Upper panel: τ = 2.0 (at 0.64-μm), effective radius (half effective particle size, R_{eff}) = 25 μm; lower panel: τ = 5.0, R_{eff} = 25 μm.

In general, the fast model provides satisfactory simulations in the case of a single ice cloud layer located above a non-Lambertian surface. The relative errors are smaller than 1% if the SZA is smaller than 35°. Note that the relative errors of the optically thick (e.g., $\tau = 5$, lower panel of Fig. 2.6) cloud layer cases are slightly smaller than those of the moderately thick (e.g., $\tau = 2$, upper panel of Fig. 2.6) cloud layer cases. The BTDF of a thick cloud is smaller than the BTDF of a moderately thick cloud and the errors resulting from the numerical integration in the adding process may be mitigated. The relative errors are maximized if both the VZA and SZA are large (i.e., up to 6% if VZA > 70° and SZA > 45°), which may be caused by the relative large variation of cloud BRDF function in these satellite geometries. Future work, such as restructuring grids near the "equator region" to improve model accuracy for large VZA and SZA cases, is necessary.

The influence of multiple cloud layers on the accuracy of the model simulation is considered by simulating overlapped ice cloud layers above a non-Lambertian surface. Similarly, comparisons between DISORT and the fast model (see Fig. 2.7) indicate that the accuracy of the current fast model maintains an acceptable level even if the multiple cloud layers give rise to more complicated processes in the forward simulation. However, the relative errors exceed 1% when the SZA is large and the upper cloud layer is transparent. It is possible that the relatively large bias is caused by the average of upper layer BTDF in the forward directions (e.g., scattering angle < 5°) since the forward diffuse transmittance is maximized when the cloud is transparent.

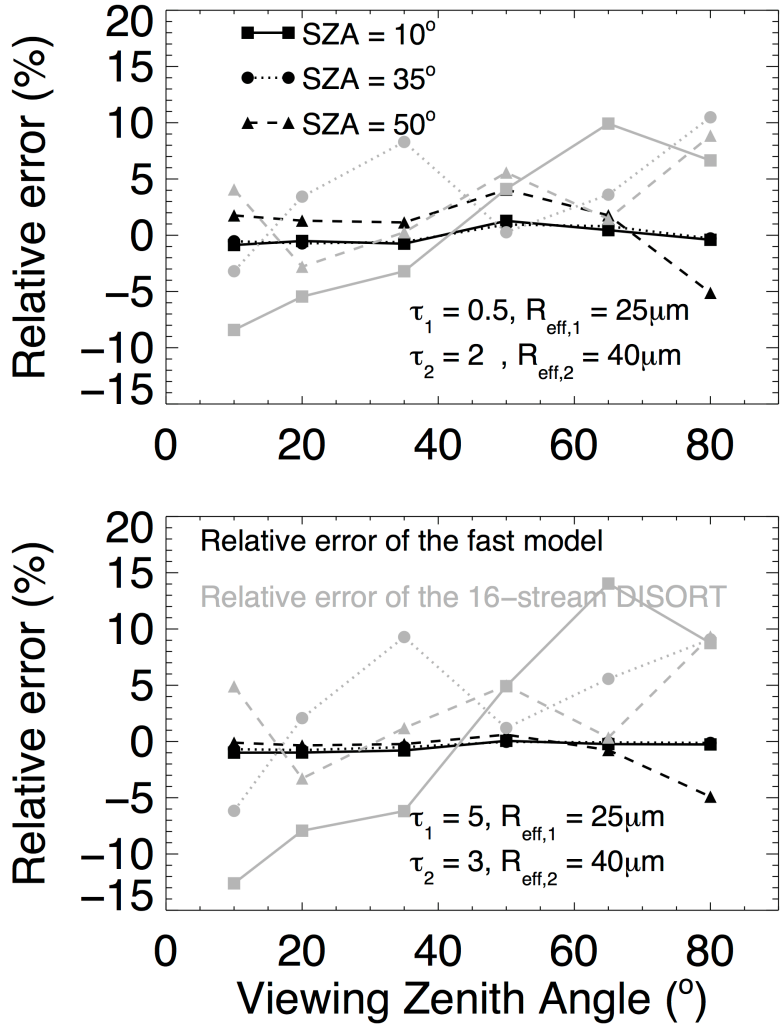

Fig.2.7 Same as Fig. 2.6, but for the overlapped ice cloud layers with non-Lambertian surface cases. Upper panel: $\tau_1 = 0.5$, $\tau_2 = 2.0$, $R_{eff,1} = 25$ μm, $R_{eff,2} = 40$ μm ; lower panel: $\tau_1 = 5.0$, $\tau_2 = 3.0$, $R_{eff,1} = 25$ μm, $R_{eff,2} = 40$ μm.

With respect to the computational efficiency, a detailed comparison is demonstrated in Fig. 2.8. As expected, the computational efficiency of the current fast

model is maximized for the case of a single cloud layer over a Lambertian surface. The BRDF and BTDF of a cloud/aerosol layer can be extracted easily from the pre-computed database and, more importantly, no additional adding procedure is required in the simulation based on the single-scattering approximation of clear-sky layers. When the presence of either a non-Lambertian surface or multiple cloud layers is taken into account, the efficiencies of both the DISORT and the fast model decrease, though by different magnitudes. The fast model calculates 80~90 times faster than the DISORT for the cases of two overlapped ice cloud layers above a reflective non-Lambertian surface. The computational efficiency of DISORT gradually decreases with an increase in the number of user defined computing angles (i.e., not Gaussian quadrature angles) due to additional interpolation of computing angles to user defined VZA. However, the increase in number of output VZA does not significantly decrease the computational efficiency of the fast model primarily because the most time consuming process in the forward simulation is the numerical integration during the adding processes. For current remote sensing purposes, such as pixel-level cloud retrieval and forward simulation coupled with a particular satellite-based instrument, the calculation is based on specified solar-satellite geometry, and for most cases, the result (i.e., TOA BRDF) at a unique VZA is required. However, for scientific research purposes, such as the study of model sensitivities to different factors, the model simulations on a series of VZAs and azimuthal angles may be desired. In these cases, this fast model has the advantage of computational efficiency. Specifically, the fast model runs 160 times, and 100 times

faster than the DISORT for a single layer with overlapped cloud layers above a non-Lambertian surface.

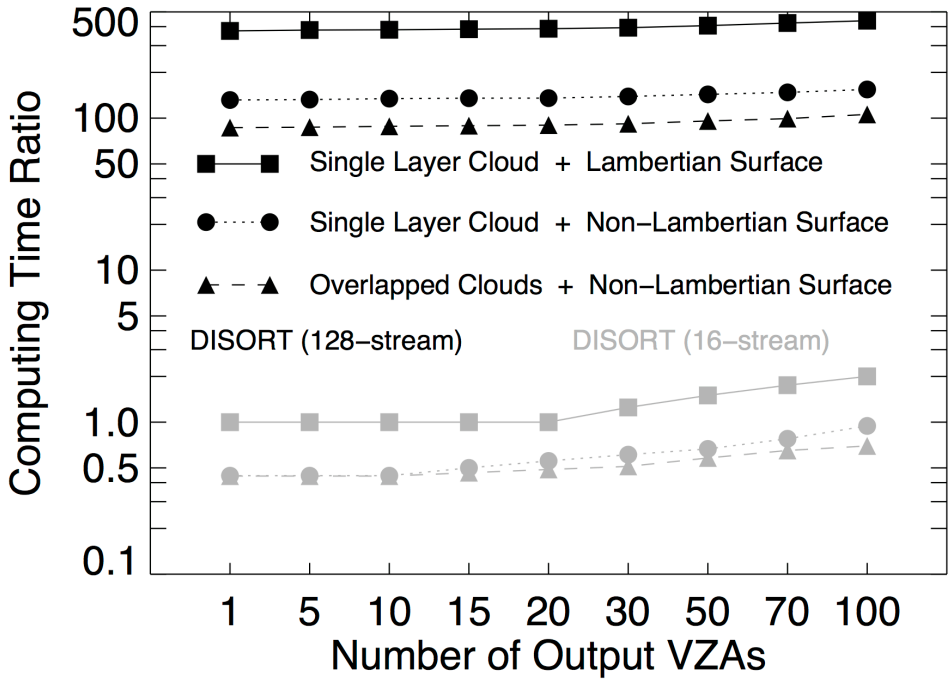

Fig.2.8 The computing time ratio of DISORT (black: 128-stream mode; gray: 16-stream mode) to the fast model as a function of number of VZA. The ratio is independent to cloud optical and microphysical properties. Three scenes are considered: single layer cloud with Lambertian surface (solid line), single layer cloud with non-Lambertian surface (dotted line), and overlapped clouds with non-Lambertian surface (dashed line).

DISORT results based on a 16-stream calculation are also employed for comparison, as shown in Figs. 2.6, 2.7, and 2.8. Although the computing times of the fast model and the 16-stream DISORT have the same order of magnitude, as evident from Fig. 2.8, the relative errors of a 16-stream DISORT simulation can exceed 10% for several geometries (see Figs. 2.6 and 2.7).

2.6 Summary

This study focuses on the development of a fast and accurate RTM for cloud property retrieval purposes in the solar spectral region. To do this, we separate the complex radiation transfer process into six relatively simple events governed by six independent RTEs and particular boundary conditions such that analytical solutions can be obtained under the plane-parallel approximation. The AD algorithm is employed to calculate the total BRDF of the consecutive non-clear (i.e., cloud/aerosol) layers, as well as to consider the directional variation of surface reflectance. Two approaches are used in the fast RTM to increase the speed of the AD algorithm. First, the major time consuming process, the doubling process, is avoided by using pre-computed LUTs. Second, the twisted icosahedral discretization scheme is adopted to improve the efficiency and accuracy of the numerical integration.

The model is validated by comparison with the 128-stream DISORT. As demonstrated in Section 2.5, the performance of this fast RTM is satisfactory in terms of both computing efficiency and accuracy. To be more specific, this model is approximately 500 times faster than DISORT for the case of one cloud or aerosol layer above a Lambertian surface because of the use of pre-computed BRDF/BTDF LUTs.

With either an increase of non-clear layers or the consideration of reflective non-Lambertian surfaces, the efficiency of both the fast RTM and DISORT decreases but by different magnitudes. However, the fast RTM still performs approximately 100 times faster than DISORT if two overlapped cloud layers and a non-Lambertian surface are considered. Additionally, the fast RTM exhibits a satisfactory simulation accuracy in the range of possible satellite-solar geometries. Indeed, the biases between the RTM and DISORT abruptly increase when both SZA and VZA angles exceed particular threshold values (i.e., SZA > 45° and VZA > 70°). For most instruments aboard a polar-orbiting satellite, the VZA values are generally smaller than 70°, such as MODIS (~ 65°) and the Visible/Infrared Imager Radiometer Suite (VIIRS, ~70°). For this reason, this fast RTM can be applied to both forward modeling and cloud/aerosol retrieval and is suitable for various space-based or aircraft based observations in the VIS/SWIR region.

CHAPTER III

A FAST HYSPECTRAL-SPECTRAL RESOLUTION RADIATIVE TRANSFER MODEL IN THE THERMAL INFRARED SPECTRAL REGION[*]

3.1 Background

Ice clouds play an important role in the Earth radiation budget through their albedo and greenhouse effects (Herman et al. 1980; Hartmann and Short 1980; Ohring and Clapp 1980; Stephens 2005; Eguchi et al. 2007). Currently, satellite-based remote sensing is the only viable means for obtaining ice cloud properties globally. However, the remote sensing of ice clouds is a challenging task because of their widely varying horizontal and vertical distribution, formation-dissipation time scales, and complicated morphology of non-spherical ice particles (Heymsfield and Iaquinta 2000; Heymsfield et al. 2002). Satellite-based measurements provide an unparalleled opportunity for monitoring the global distribution of ice clouds and their optical and microphysical properties. In comparison with solar-reflectance-based retrieval algorithms (Nakajima and King 1990), the advantages offered by infrared (IR) sensors [e.g., the high-spectral-

---

[*] Part of this chapter is reprinted with permission from "Retrieval of ice cloud optical thickness and effective particle size using a fast infrared radiative transfer model" by C. Wang, P. Yang, B. A. Baum, S. Platnick, A. K. Heidinger, Y. X. Hu, and R. E. Holz, 2011. *Journal of Applied Meteorology And Climatology*, **50**, 2283-2297, doi:10.1175/JAMC-D-11-067.1, Copyright by American Meteorological Society, and "Retrieval of ice cloud properties from AIRS and MODIS observations based on a fast high-spectral-resolution radiative transfer model" by C. Wang, P. Yang, S. Platnick, A. K. Heidinger, B. A. Baum, T. Greenwald, Z. Zhang, and R. E. Holz, 2013. *Journal of Applied Meteorology And Climatology*, **52**, 710-727, doi:10.1175/JAMC-D-12-020.1, Copyright by American Meteorological Society.

resolution sensors – the Atmospheric Infrared Sounder (AIRS, Aumann et al. 2003) and the Infrared Atmospheric Sounding Interferometer (IASI, Blumstein et al. 2004)] are that the ice cloud retrievals are consistent for both daytime and nighttime conditions and are less sensitive to ice particle habits, degree of surface roughness, and ice particle inhomogeneity. On the other hand, IR-based optical thickness retrievals are limited to smaller optical thickness in comparison with solar reflectance-based techniques and require accurate surface temperature and atmospheric state profiles (e.g., Huang et al. 2004; Cooper and Garrett 2010). Some studies demonstrated that shortwave and IR observations provide complementary information and therefore the combination of the two can provide more consistent retrievals (Baran and Francis 2004a).

To simulate the IR radiative transfer (RT) in a cloudy atmosphere, an IR radiative transfer model (RTM) that incorporates both gaseous absorption and multiple scattering within cloud layers is indispensable. The line-by-line (LBL) radiative transfer model (LBLRTM; Clough et al. 2005) is a rigorous model that accounts fully for both the line absorption and continuum absorption (Clough et al. 1989) of various absorption gases in the planetary atmosphere. However the LBL model is too expensive computationally for consideration as an operational method where speed is a necessity. Many algorithms are available to alleviate the computing burden of the LBL model and include the Exponential Sum Fitting of Transmissions method (ESFT; Armbruster and Fischer 1996), the correlated-*k* distribution method (CKD; Arking and Grossman 1972; Lacis et al. 1979; Goody et al. 1989; Lacis and Oinas 1991; Kratz 1995), the Optimal Spectral Sampling method (OSS; Moncet et al. 2008), the Principle Component-based

Radiative Transfer Model (PCRTM; Liu et al. 2006), the Radiative Transfer for Television Infrared Observation Satellite (TIROS) Operational Vertical Sounder (RTTOV; Saunders et al. 1999, 2006) and the fast narrowband transmittance model (FFTM; Wei et al. 2007). These algorithms employ different theoretical approaches and are designed for different purposes. For example the CKD and OSS methods simulate the spectral transmittance of a narrow interval by computing a selected number of representative monochromatic transmissions rather than fully considering the effects from the entire set of absorption lines, as is done in the LBL algorithm. The PCRTM removes redundant monochromatic calculations using a principle component analysis and significantly improves the efficiency by the predetermined principal component scores. The FFTM uses pre-computed non-linear regression coefficients to fit the absorption coefficient with a moderate spectral resolution (i.e., 1 cm^{-1}).

In an absorptive-scattering medium, a cloud-scattering properties model is also a critical component in RT simulations. Various rigorous RTMs, such as the discrete ordinates radiative transfer model (DISORT; Stamnes et al. 1988) and the adding-doubling method (Twomey et al. 1966; Hansen and Hovenier 1971a), consider multiple scattering and are considered to be the standard benchmarks for RTMs. However, their high computational costs prevent them from operational use in global cloud property retrievals and numerical weather prediction data assimilation efforts. To solve this problem, several previous studies (e.g., Baran and Francis 2004a; Wei et al. 2004; Dubuisson et al. 2005; Heidinger et al. 2006; Wang et al. 2011) developed a series of fast radiative transfer equation (RTE) solvers to facilitate the design of ice cloud

retrieval algorithms. For example, The RTTOVE is a fast RT model developed for space-based multi-sensors and can be coupled with a numerical weather prediction model. Dubuisson et al. (2005) developed a fast RTM to simulate top-of-the-atmosphere (TOA) brightness temperatures (BTs) for clear or water-cloudy atmospheres. Heidinger et al. (2006) developed the Successive Order of Interaction model by implementing several approximations to the adding-doubling method that are most applicable to moderately scattering atmospheres in the IR and microwave regions. Wei et al. (2004) reported the development of a fast infrared RTM (FIRTM1). In extending from a single cloud layer to multiple cloud layers, Niu et al., (2007) developed a RTE solver (FIRTM2) to simulate upwelling radiance at the TOA efficiently for multilayered clouds. Both FIRTM1 and FIRTM2 are faster than the DISORT by three orders of magnitude. Based on the adding-doubling method, Zhang et al. (2007) developed a adding-doubling based fast RTE solver (FIRTM-AD) that could be applied to an atmosphere with an arbitrary number of cloud and aerosol layers with different microphysical and optical properties. The FIRTM-AD can be used for analysis of both space-based and ground-based high-spectral resolution radiance observations. The FIRTM-AD performs similar calculations 250 times as fast as the DISORT. However, the accuracies decrease since these models assume clouds to be isothermal. The root-mean-square error (RMSE) of FIRTM-AD in BTs is smaller than 0.1 K in comparison with the rigorous DISORT simulations. The RMSEs of FIRTM1 and FIRTM2 approach 0.5 K. Hong et al. (2007) reported that consideration of the cloud geometrical thickness (essentially the non-isothermal effect of clouds) improves the model simulation.

In this study, a new high-spectral-resolution cloudy-sky radiative transfer model (HRTM) is developed to account to account for gas absorption. Specifically, a clear-sky transmissivity database containing both line and continuum absorption is generated based on the LBLRTM (version: 11.7; Clough et al. 2005) with a 0.1 cm^{-1} spectral resolution. The total transmissivity within a certain spectral interval of a thin inhomogeneous layer is determined by the absorber amount, density weighted pressure, and temperature. Based on this transmissivity database, the layer absorption optical thickness is calculated. The model incorporates high-spectral-resolution ice cloud bulk scattering properties from Baum et al. (2007). The bulk scattering model is developed using single scattering properties of ice crystals calculated by Yang et al. (2005) and Zhang et al. (2004), and in situ measured ice cloud microphysical data, including both particle size distributions (PSDs) and particle habit distributions (HDs, Heymsfield et al. 2002; Baum et al. 2005a).

An efficient RTE solver (Wang et al. 2011) is developed to simulate satellite observations for different atmospheric conditions. This RTE solver takes advantage of the pre-computed lookup tables (LUTs) including cloud transmissivity, reflectivity, effective emissivity, and effective temperature that consider the multiple scattering, absorption, and thermal emission processes. Moreover, these ice cloud LUTs are generated with a high spectral resolution. The HRTM can be applied to current high-spectral-resolution instruments, such as the AIRS and IASI, and narrow band instruments, such as the MODIS and the Spinning Enhanced Visible and Infrared Imager (SEVIRI). In the future, similar measurements will be provided by the Geostationary

Operational Environmental Satellite Advanced Baseline Imager (GOES-R/ABI), the Visible Infrared Imaging Radiometer Suite (VIIRS), and the Cross-track Infrared Scanner (CrIS).

The chapter is organized as follows. Section 3.2 introduces basic principles of clear-sky transmissivity simulation and the method used to solve RTE efficiently. The performance of HRTM is evaluated in Section 3.3 in comparison with simulations of both the LBLRTM and DISORT in a 32-stream mode. Summary and conclusions are given in Section 3.4.

3.2 Forward model

3.2.1 Clear-sky transmissivity

The HRTM includes three components: (1) a fast clear-sky transmissivity or absorption optical thickness simulator, (2) a fast RTE solver, and (3) a cloud multiple scattering-thermal emission and absorption model (Wang et al. 2011). This section describes the method and technical details related to the clear-sky gas absorption component of the HRTM.

For a given absorption line at an arbitrary monochromatic wavenumber, the absorption coefficient is mainly determined by pressure, temperature, and the spectral distance between the wavenumber and the center of the absorption line. However, for some strong absorbers, such as water vapor, the absorption coefficients are also influenced by the amount of substance present because of the self-broadening processes (Clough et al. 1989). For a clear atmospheric layer, the monochromatic transmissivity depends on the absorption coefficient and the absorber amount. Instead of deriving clear-

sky transmissivity from the gas absorption coefficient as in the LBLRTM, we build an extensive database of clear-sky transmissivity directly as a function of pressure, temperature, and absorber amount. Based on this database, the monochromatic transmissivity of the clear-sky layer can be derived efficiently and incorporated into an RTM under the plane-parallel approximation.

In extending from a single clear layer case to a more complex atmosphere, the total monochromatic transmissivity at a given wavenumber υ is given by:

$$T(\upsilon) = \prod_{i=1}^{N} T_i(\upsilon), \tag{3.1}$$

where the subscript i is the index of a homogenous layer (i.e., constant pressure, temperature, and absorber amount). For practical use, a narrow spectral interval is defined such that the variation of the Planck function within the interval can be ignored, and the total spectral transmissivity of the atmosphere within the interval approximately satisfies the multiplication in Eq. (3.1):

$$\overline{T}_{\Delta\upsilon} = \int_{\Delta\upsilon} \prod_{i=1}^{N} T_i(\upsilon) \frac{d\upsilon}{\Delta\upsilon} \cong \prod_{i=1}^{N} \int_{\Delta\upsilon} T_i(\upsilon) \frac{d\upsilon}{\Delta\upsilon}. \tag{3.2}$$

The spectral interval, 0.1 cm^{-1}, is found to satisfy the above conditions, while maintaining the simulation accuracy and the computational efficiency. For most simulations in the thermal IR window region (e.g., 800-1200 cm^{-1}), the relative errors of the total spectral transmissivity derived from the right side of Eq. (3.2) for clear-sky scenes are limited to 0.1% compared with the accurate transmissivity values given by integrating Eq. (3.1) in the spectral intervals (shown in Table 3.1). Note that we only consider the impact from the spectral interval on the simulation for narrowband

instruments, such as the MODIS, because a 1 cm^{-1} spectral interval is too large for the spectral response functions (SRF) of high-spectral-resolution instruments such as AIRS and IASI.

Table 3.1 Clear-sky layer transmissivities calculated with different spectral resolutions.

MODIS IR band	0.001 cm^{-1} spectral resolution	0.1 cm^{-1} spectral resolution (Relative Error)	1.0 cm^{-1} spectral resolution (Relative Error)
	U.S. Standard Atmosphere		
Band 29 (8.5 μm)	0.7672	0.7680 (0.1%)	0.7678 (0.1%)
Band 31 (11 μm)	0.8826	0.8822 (0.1%)	0.8638 (2.1%)
Band 32 (12 μm)	0.8348	0.8349 (0.0%)	0.8364 (0.2%)
	Tropical Summer Profile		
Band 29 (8.5 μm)	0.5045	0.5052 (0.1%)	0.5041 (0.1%)
Band 31 (11 μm)	0.5192	0.5185 (0.1%)	0.4987 (3.9%)
Band 32 (12 μm)	0.4086	0.4087 (0.0%)	0.4093 (0.2%)

Simulations in the thermal IR region need to account for multiple absorptive gases such as water vapor, carbon dioxide, carbon monoxide, ozone, methane, and nitrous oxide. The effect of continuum absorption due to the far wings of individual pressure broadening spectral lines is also important, especially in the 700-1200 and 2000-3000 cm^{-1} spectral regions (Clough et al. 1989). Several previous studies (e.g. Wei

et al. 2007; Moncet et al. 2008) treat line absorption and continuum absorption separately; that is, the total transmissivity of a layer is the product of the transmissivities due to line absorption and those by the continuum absorption:

$$\overline{T}_{i,\Delta\upsilon} \cong T_{cont} \prod_{j=1}^{M} \overline{T}_{i,\Delta\upsilon}^{j}, \tag{3.3}$$

where the index j indicates the j^{th} absorptive gas and T_{cont} is the transmissivity contribution from continuum absorption. Similar to the case in Eq. (3.2), both the accuracy and computational efficiency of Eq. (3.3) decrease with the number of absorbers (Wei et al. 2007). In the HRTM, two steps are implemented to avoid a decrease in both calculation speed and simulation accuracy due to multiple products. First, the contribution of continuum absorption is included in a pre-computed transmissivity database. Second, water vapor, carbon dioxide, and oxygen are treated as a "mixed-gas", whose effective concentration is solely determined by the amount of water vapor if the ambient pressure and temperature are specified since carbon dioxide and oxygen are well-mixed gases. Additionally, water vapor and carbon dioxide are the two most important absorptive gaseous species throughout the IR region. As a result, the introduction of the mixed-gas facilitates the computational efficiency and maintains the calculation accuracy of the continuum absorption resulting from water vapor self-broadening and foreign broadening. It is thus convenient to rewrite the thin-layer spectral transmissivity (Eq. 3.3), as follows:

$$\overline{T}_{\Delta\upsilon,total} \cong \overline{T}_{\Delta\upsilon}(P,t,u_{mix}) \times \overline{T}_{\Delta\upsilon}(P,t,u_{O_3}) \times \overline{T}_{\Delta\upsilon}(P,t,u_{CO}) \times \overline{T}_{\Delta\upsilon}(P,t,u_{CH_4}) \times \overline{T}_{\Delta\upsilon}(P,t,u_{N_2O}), \tag{3.4}$$

where P and t are the pressure and temperature of a homogeneous clear-sky layer, respectively, and u is the gas amount within the layer.

Table 3.2 The grids of pre-computed transmissivity database for absorptive gases.

Variables[†]	Low pressure layers	Median pressure layers	High pressure layers
Pressure (hPa)	50 grids: 1150 ~ 100.0	50 grids: 100 ~ 10.0	50 grids: 10 ~ 0.1
Temperature (K)	110 grids: 309 ~ 200	40 grids: 239 ~ 200	110 grids: 309 ~ 200
Absorber amount[‡] (atm cm)	100 grids: 10^{-4} ~ 10^{1}	100 grids: 10^{-4} ~ 10^{1}	100 grids: 10^{-4} ~ 10^{1}

The pre-computed gas spectral transmissivity database is generated using the latest version of the LBLRTM (Clough et al. 2005) with the High-Resolution Transmission molecular absorption database (HITRAN 2004; Rothman et al. 2005), and including the Mlawer, Tobin, Clough, Kneizys, and Davies continuum model (also known as MT_CKD version: 2.5; Mlawer et al. 2003). The spectral transmissivities for

[†] Grid spacing of pressure and absorber amount is logarithmic.
[‡] The absorber amount of water vapor for the lower part is from 10^{-4} to 10^{3} atm cm.

each absorptive gaseous species are tabulated over hundreds of pressure levels, temperatures, and amount grids. To be more specific, the entire atmosphere is divided into three parts according to the pressure (i.e., low, median, and high). Table 3.2 gives the detailed information of the selected grids of the pre-computed transmissivities.

To apply the present database to simulate an arbitrary inhomogeneous thin clear-sky layer, the density weighted effective layer pressure and temperature are used (Gallery et al. 1983). The definition can be expressed as follows:

$$\overline{P} = \frac{\int_{h_1}^{h_2} P(h)\rho(h)dh}{\int_{h_1}^{h_2} \rho(h)dh} \text{ and} \tag{3.5}$$

$$\overline{t} = \frac{\int_{h_1}^{h_2} t(h)\rho(h)dh}{\int_{h_1}^{h_2} \rho(h)dh}, \tag{3.6}$$

where h_1 and h_2 specify the lower and upper attitudes of the layer, respectively, and $P(h)$ and $\rho(h)$ indicate the pressure and density at altitude h. Subsequently, the layer spectral transmissivity can be inferred from the database using a three-dimensional interpolation. While the concentration of carbon dioxide has been increasing during the past 50 years, the CO_2 concentration in the model is selected as 385 ppm without the seasonal variation. Were the model to be used for decadal satellite data processing, the changing concentration of CO_2 would need to be considered.

3.2.2 Cloud included RTM

As shown in Fig 3.1, the atmosphere is assumed to consist of N−1 layers (i.e., L_1, L_2, …, L_{M-1}, L_{M+1}, …, L_N) with an ice cloud in layer L_M. Each clear atmospheric layer has

a unique extinction optical thickness (τ) and a mid-layer temperature, whereas an ice cloud layer is specified by four basic properties: cloud-top temperature T_{top}, cloud-base temperature T_{base}, t, and effective particle size (D_{eff}). To consider non-isothermal ice cloud layer, we introduce a new physical quantity, effective temperature T_e, defined as:

$$T_e = T_B(\frac{I}{\varepsilon_c}), \tag{3.7}$$

where I is the emitted radiance from the cloud layer, ε_c indicates the cloud effective emissivity, and T_B expresses the inversion of the Planck function. We generate four LUTs, including cloud transmissivity (t), reflectivity (r), ε_c, and T_e. Unless specifically stated, the ice extinction cloud optical thickness is referenced to a visible (VIS, 0.65-μm) wavelength, i.e., $\tau_{ext,vis}$. The ice cloud extinction optical thickness at an arbitrary wavelength ($\tau_{ext,\lambda}$) can be derived as follows:

$$\tau_{ext,\lambda} = \tau_{ext,vis} \frac{\langle Q_{ext,\lambda} \rangle}{\langle Q_{ext,vis} \rangle}, \tag{3.8}$$

where $< Q_{ext,\lambda} >$ represents the bulk extinction efficiency at wavelength λ and $< Q_{ext,vis} >$ is the bulk VIS extinction efficiency, both of which depend on the D_{eff}. It must be emphasized that, in this study, the effect of vertical inhomogeneity of D_{eff} is ignored. The definition of D_{eff} is shown in Eq. (1.3).

As shown in Fig. 3.1, I_1 and I_2 indicate the thermal emission from the total atmospheric layers below and above the cloud layer, respectively. Similarly, Γ_1 and Γ_2 indicate the total transmissivities of the two atmospheric layers, respectively. I_c and I_s represent the emitted radiances from the ice cloud layer and the surface, respectively.

$T(z)$ indicates the air temperature at altitude z. T_s and ε_s are the surface temperature and emissivity, respectively. $\Gamma(z)$ represents the transmissivity of atmosphere from the TOA to altitude z. The TOA upward radiance I_{TOA} can be expressed as the sum of three parts: the direct transmission part of the thermal emission from the surface, ice cloud, and atmosphere I_A; the first-order radiance reflected by the surface I_B; and the first-order radiance reflected by the ice cloud I_C, which can be expressed as follows:

$$I_A = I_s \Gamma_1 t \Gamma_2 + I_1^{\uparrow} t \Gamma_2 + I_c^{\uparrow} \Gamma_2 + I_2^{\uparrow}, \tag{3.9}$$

$$I_B = (I_1^{\downarrow} + I_c^{\downarrow} \Gamma_1 + I_2^{\downarrow} t \Gamma_1) \times (1 - \varepsilon_s) \Gamma_1 t \Gamma_2, \tag{3.10}$$

$$I_C = I_2 t \Gamma_2, \tag{3.11}$$

where the two arrow symbols indicate the down-welling and up-welling radiances correspondingly. The emitted radiances from the cloud, the surface, and atmosphere can be expressed as follows:

$$I_c = B(T_e)\varepsilon_c, \tag{3.12}$$

$$I_s = B(T_s)\varepsilon_s, \tag{3.13}$$

$$I_1^{\uparrow} = \int_0^{cloudbase} B[T(z)] \frac{d\Gamma(z)}{dz} dz, \tag{3.14}$$

$$I_2^{\uparrow} = \int_{cloudtop}^{\infty} B[T(z)] \frac{d\Gamma(z)}{dz} dz, \tag{3.15}$$

where B is the Planck function.

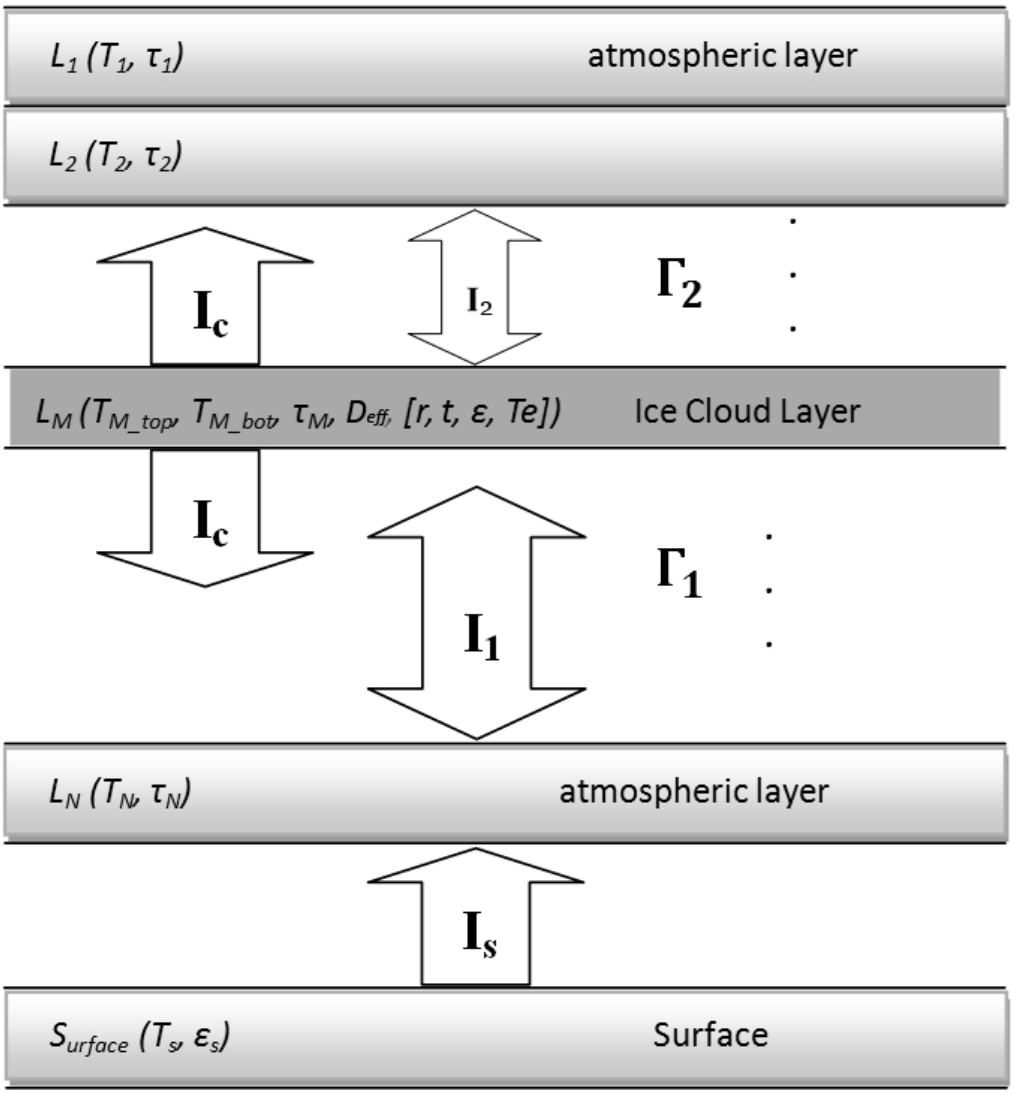

Fig.3.1 Illustrative diagram of the fast IR RTM radiance components *I* for a single ice cloud in layer L_M, located between top and bottom layers L_1, and L_N, respectively.

To increase the computational efficiency and maintain the accuracy, four LUTs (r, t, ε_c, and T_e) are generated by using the DISORT in the 32-stream mode. The

averaged bulk scattering properties (Baum et al. 2007) including the extinction efficiency, single-scattering albedo, and scattering phase function are used as input parameters in the DISORT.

The corresponding cloud effective emissivity function can be expressed as follows, by assuming an isothermal cloud layer with temperature T_c:

$$\varepsilon_c(\tau, D_{eff}, \mu) = \frac{I_{cloudtop}(T_c, \tau, D_{eff}, \mu)}{B(T_c)}. \tag{3.16}$$

where μ indicates the cosine of the zenith angle of radiance direction, and $I_{cloudtop}$ is the up-welling radiance at cloud top. Although both $I_{cloudtop}$ and $B(T_c)$ are temperature dependent, the effective emissivity ε_c is relatively insensitive to temperatures between 200 and 260 K, the range that encompasses most atmospheric ice clouds. After calculating the cloud effective emissivity with the DISORT, T_e for a non-isothermal ice cloud layer (in this study, we assume that the temperature within a cloud layer varies with height linearly) can be expressed as:

$$T_e = \left\{ \frac{T_B\left[\dfrac{I(T', T'', \tau, D_{eff}, \mu)}{\varepsilon_c(\tau, D_{eff}, \mu)}\right] - T'}{T'' - T'} \right\} \times (T_{base} - T_{top}) + T_{top}, \tag{3.17}$$

where $I(T', T'', \tau, D_{eff}, \mu)$ is the DISORT computed thermal emission at the top (or bottom) of a non-isothermal cloud with an arbitrary cloud-top temperature T' and cloud-base T''. T_{base} and T_{top} are the actual temperatures of the cloud base and cloud top. Note that the four LUTs depend on wavelength.

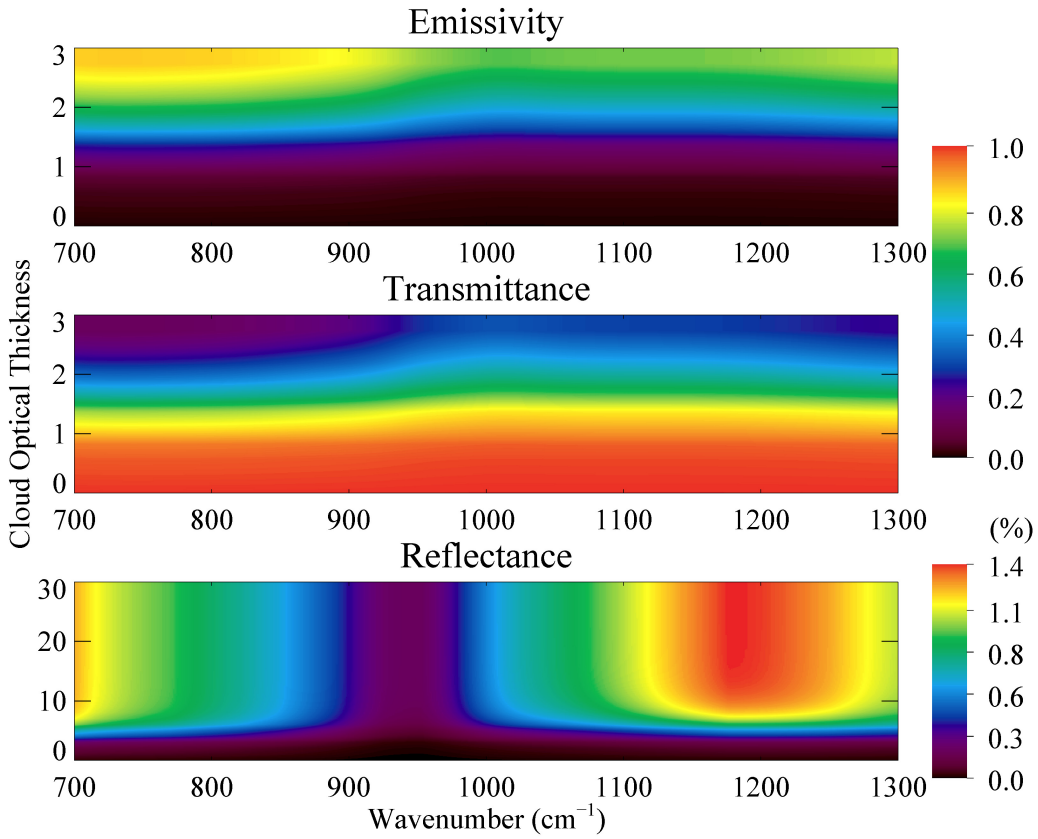

Fig.3.2 Examples of pre-computed LUTs (emissivity, transmissivity, and reflectivity) as a function of wavenumber and cloud optical thickness (D_{eff} = 50 μm).

The four LUTs are pre-computed for 33 τ values ranging from 0.01 to 100, 18 D_{eff} values from 10 to 180 μm, nine viewing zenith angles from 0° to 80°, and 600 monochromatic wavenumbers with a 1.0 cm^{-1} from 700 cm^{-1} to 1300 cm^{-1}. Fig. 3.2 shows an example of the ice cloud LUTs. In the thermal IR window region, the ice cloud reflectance is close to 0 (especially when wavenumber is close to 950 cm^{-1}) due to

significant absorption of ice crystal. The transmissivity values are close to 0 if τ is larger than 2. For this reason, higher-order reflections between cloud layer and the surface can be safely ignored for simplification in the spectral region.

To work with satellite-based IR sensors such as the AIRS and MODIS, the TOA up-welling radiances are weighted by the SRF:

$$I_{ch,TOA} = \frac{\int_{\Delta\upsilon} I_{TOA}(\upsilon) R_{ch}(\upsilon) d\upsilon}{\int_{\Delta\upsilon} R_{ch}(\upsilon) d\upsilon}, \tag{3.18}$$

where $R_{ch}(\upsilon)$ is the SRF of instrument. For example, the AIRS sensor, consisting of 2378 IR channels, measures the upwelling radiance at the TOA from 650 to 2670 cm^{-1} with a spectral resolving power $\upsilon/\Delta\upsilon = 1200$. The half-width of the AIRS SRF increases moderately from 0.6 to 1.1 cm^{-1} with increasing channel center wavenumber. To more efficiently consider the AIRS SRFs, each SRF is truncated when the wavenumber distance is greater than 1.2 cm^{-1} from the channel center. Therefore, for applications with AIRS observation, Eq. (3.18) can be rewritten as:

$$I_{ch,TOA} = \frac{\sum_{n=-12}^{n=12} I_{TOA}(\upsilon_{ch} + n\Delta\upsilon) R_{ch}(\upsilon_{ch} + n\Delta\upsilon)\Delta\upsilon}{\sum_{n=-12}^{n=12} R_{ch}(\upsilon_{ch} + n\Delta\upsilon)\Delta\upsilon}, \tag{3.19}$$

where υ_{ch} is the center wavenumber of an AIRS channel and $\Delta\upsilon$ is the spectral resolution of HRTM (i.e., 0.1 cm^{-1}).

3.3 Model validation

In this section the accuracy and efficiency of HRTM are evaluated by comparing with the benchmark models: LBLRTM and DISORT with 32-stream mode (hereafter

referred to as LBLDIS) for clear-sky cases (shown in Fig.3.3) and cloudy-sky cases (shown in Fig.3.4) with a high-spectral resolution. Specifically, Fig.3.3 shows the spectral transmissivity as a function of wavenumber for a single inhomogeneous atmospheric layer with averaged pressure and temperature values of 975 hPa and 270.5 K, respectively (calculated from Eq. 3.5 and Eq. 3.6). In the region between 700 and 1300 cm^{-1}, the root-mean-square error (RMSE) of transmissivity is limited to 0.001. For the cloudy-sky simulations, a typical mid-latitude summer atmospheric profile is used. As shown in Fig.3.4, the largest BT difference (HRTM-LBLDIS) of 0.2 K is found when an ice cloud is optically thin and consists of small particles. Meanwhile, relatively large RMSE occurs in a CO_2 absorption band (up to 0.25 K; 700~740 cm^{-1}) and a water vapor absorption band (0.3 K; 1260~1300 cm^{-1}). One cause of the relatively large differences may be related to the relatively strong absorption in the two narrow bands, which may lead to significant variations of transmissivities and therefore decrease the accuracy of applying the multiplication rule to HRTM with an assumed 0.1 cm^{-1} spectral resolution. With a gradual increase in cloud optical thickness, the RMSE decreases from 0.2 to 0.1 K (e.g., τ = 3), and to 0.05 K (τ = 5). For the last two cases, the TOA upwelling radiances are dominated by the ice cloud thermal emission as a result of the high optical thickness values and strong absorption of ice crystals. An interesting point to note is that large departures in the BT spectrum can be found in the CO_2 and O_3 bands if a cloud layer is optically thick. This is caused by gas emission above the cloud layer that becomes significant if the background radiance is small in comparison with the emission from the absorptive gas (i.e., cloud is high in altitude and optically thick).

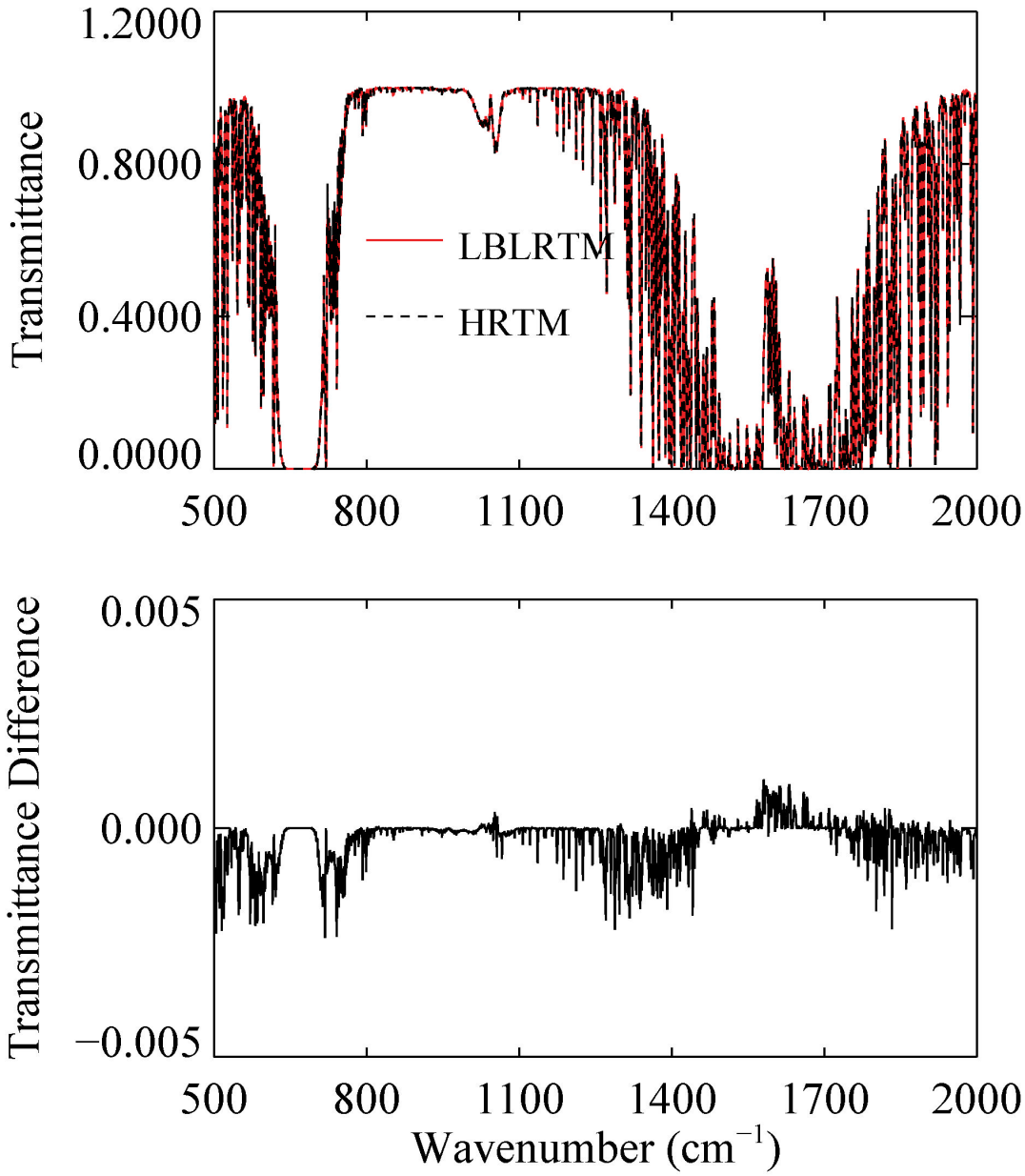

Fig.3.3 Inhomogeneous clear-sky layer (top) transmissivity calculated by the HRTM and the LBLRTM and their differences (bottom). Averaged pressure and temperature are 975 hPa and 270.5 K, respectively.

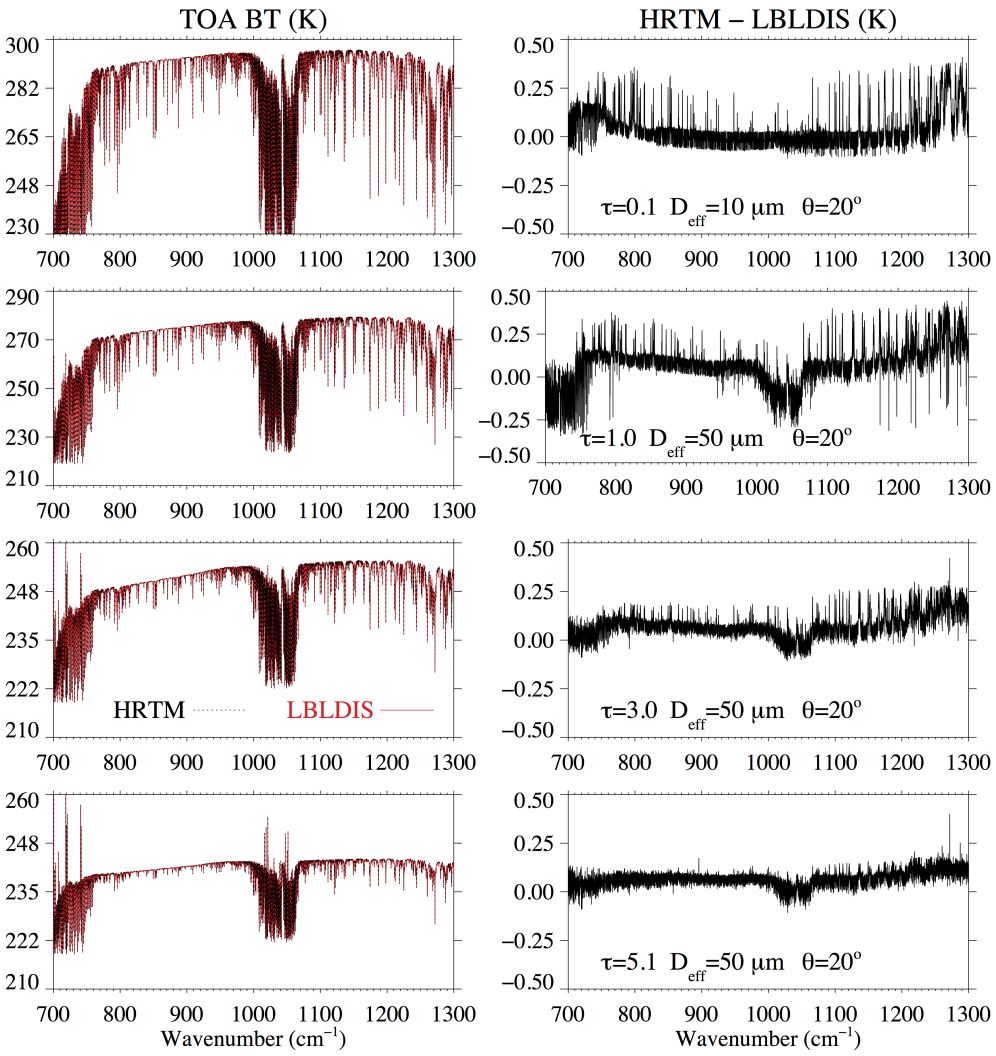

Fig.3.4 HRTM and LBLDIS (left) simulated TOA BTs and their differences (right).

Another special case is also included for validation of the model capability for thin cirrus clouds. These clouds with small optical thickness values (e.g., 0.1), consisting of small ice particles (e.g., D_{eff} = 10 μm), are frequently observed near tropical

tropopause (McFarquhar et al. 2000). In the thermal window region, the HRTM demonstrates and excellent ability to model the thin cirrus cloud. With regard to the computational efficiency, HRTM simulates the TOA BTs (single ice cloud layer, 70 clear layers, summer mid latitude atmospheric profile) from 700 to 1300 cm^{-1} with a 0.1 cm^{-1} spectral resolution in a time that is three orders of magnitude shorter than the LBLDIS.

3.4 Summary

The present study explores the development of a high-spectral-resolution radiative transfer model to simulate IR radiances at the TOA rapidly and accurately. To minimize the computational burden, a transmissivity database is generated for seven major absorptive gases with a 0.1 cm^{-1} spectral resolution, which is sufficient for considering the SRF of a spaceborne hyperspectral sensor. The layer transmissivity of an individual absorber is determined by the absorber amount, density-weighted pressure, and temperature. Moreover, carbon dioxide and oxygen are treated as a mixed gas because of their relatively constant concentrations. The effect of continuum absorption has been included in the present database to reduce the computing time.

For cloud simulations, in addition to the reflectivity and transmissivity LUTs of cloud, which are employed in some previous RTMs (e.g., Wei et al. 2004; Niu et al. 2007), the HRTM uses cloud effective emissivity and effective temperature to improve the accuracy. Specifically, the use of the additional two LUTs captures the non-isothermal properties of natural clouds, in particular for simulating transparent clouds. For instance, the internal part of a cloud of an optically thin cloud also contributes to the

emitted radiance at cloud top. For this reason, it is important to find a relation between the cloud-top/cloud-base temperature and cloud emission. On the basis of the cloud effective temperature, the HRTM computes upwelling (downwelling) radiance at cloud-top (cloud-base) efficiently and accurately.

Generally speaking, the comparisons of TOA BT simulations between the HRTM and LBLDIS show that the differences are less than 0.2 K. The computational speed of the HRTM is three orders of magnitude faster than the LBLDIS. However, a limitation of the HRTM is that the clear-sky transmissivity database is quite large (~20 GBytes). Additionally, this model can be applied only to clear sky or single-layer cloud cases. Adding-doubling based method is required to extend the current model capability to multiple cloud layers.

CHAPTER IV

RETRIEVAL OF ICE CLOUD OPTICAL AND MICROPHYSICAL PROPERTIES USING THE FAST RADIATIVE TRANSFER MODELS*

4.1 Background

Numerous approaches (e.g., Nakajima and King 1990; Stubenrauch et al. 1999; Platnick et al. 2003; Chiriaco et al. 2004; Kokhanovsky and Nauss 2005; Minnis et al. 2011a, b) have been developed to infer ice cloud optical thickness τ, effective particle size D_{eff}, and the ice particle size distribution function (PSD; e.g., Mitchell et al. 2010) from satellite-based imager and high-spectral-resolution infrared (IR) sounder measurements (Wei et al. 2004; Huang et al. 2004; Yue et al. 2009; Wang et al. 2013a). The method used by the Moderate Resolution Imaging Spectroradiometer (MODIS) operational cloud-property retrieval is a bi-spectral method employing observations from a combination of two solar-reflectance bands (Platnick et al. 2003). The premise of this approach is that a weakly absorbing, visible or near-infrared window band (VIS/NIR, e.g., 0.64, 0.86, or 1.24-μm) is sensitive mainly to τ, whereas an ice absorbing shortwave

---

* Part of this chapter is reprinted with permission from "Retrieval of ice cloud optical thickness and effective particle size using a fast infrared radiative transfer model" by C. Wang, P. Yang, B. A. Baum, S. Platnick, A. K. Heidinger, Y. X. Hu, and R. E. Holz, 2011. *Journal of Applied Meteorology And Climatology*, **50**, 2283-2297, doi:10.1175/JAMC-D-11-067.1, Copyright by American Meteorological Society, and "Retrieval of ice cloud properties from AIRS and MODIS observations based on a fast high-spectral-resolution radiative transfer model" by C. Wang, P. Yang, S. Platnick, A. K. Heidinger, B. A. Baum, T. Greenwald, Z. Zhang, and R. E. Holz, 2013. *Journal of Applied Meteorology And Climatology*, **52**, 710-727, doi:10.1175/JAMC-D-12-020.1, Copyright by American Meteorological Society.

infrared (SWIR) band (e.g., 1.6, 2.13, or 3.75-μm) is sensitive to both D_{eff} and τ. To be more specific, in a VIS band, scattering is dominant so that the reflectance is primarily dependent of τ. For a SWIR band, in which both scattering and absorption are important, the single-scattering albedo decreases and the asymmetry factor increases with an increase of D_{eff}, resulting in a high sensitivity of reflectance to D_{eff} in this spectral region.

The ice cloud properties can be inferred from radiance measurements based on lookup tables (LUTs) that include the transmissivity and reflectivity functions for clouds of various viewing geometries, surface boundary conditions, and cloud properties. This approach works best when the isolines of τ and D_{eff} in the $R_{0.86}$–$R_{2.13}$ (here the terms indicate the reflectances at the two bands) space are orthogonal, which tends to occur when τ is higher than 5. At lower values of τ, the isolines begin to converge, coupling the τ and D_{eff} solution. Furthermore, as τ decreases below 4, the retrievals become increasingly sensitive to surface albedo characteristics, that is, the clear-sky values for the VIS/NIR and SWIR bands. Because VIS/NIR and SWIR bands are involved, this method is limited to daytime retrievals in which the solar zenith angle is less than (~80°). In addition, as shown in several previous studies (e.g., Hess et al. 1998; Sun et al. 2004; Yang et al. 2008; Xie et al. 2009; Baum et al. 2010), the single-scattering properties in the solar bands are sensitive to the assumed ice habit and the degree of ice particle surface roughening, and these effects influence the LUTs.

Another approach to inferring cloud properties is the split window technique (Inoue 1985), which is based on two IR-window channels (i.e., 11 and 12-μm). The premise for this method is that the absorption characteristics of ice crystals are different

at wavelengths 11 and 12-μm (Prabhakara et al. 1988). This is the approach adopted for the decadal cloud property record from the Advanced Very High Resolution Radiometer (Heidinger and Pavolonis 2009). The split-window method is sensitive to optically thin ice clouds for which $0.1 < \tau < 4$ and, as such, is complementary to the solar-reflectance method adopted by MODIS. Another benefit is that the split-window method can be applied to all data regardless or solar illumination, leading to consistent retrievals for both daytime and nighttime conditions, a distinct advantage for building ice cloud climatology. Furthermore, the ice crystal optical properties (Baran and Francis 2004b, 2009; Yang et al. 2005, and references cited therein) used to generate the LUTs are fundamental to ice cloud-property retrievals (Chepfer et al. 1998; Wendisch et al. 2005; Yang et al. 2007), and it is very challenging to simulate realistic ice crystal shapes and surface textures (i.e., the degree of surface roughness) in light-scattering calculations. In another words, the LUTs based on IR bands are much less sensitive to ice particle habit and structure. It is shown that the split-window based cloud retrievals require accurate surface temperature and emissivity, and atmospheric state profiles (e.g., Huang et al. 2004; Cooper and Garrett 2010). Some studies demonstrated that the VIS/SWIR and IR observations provide complementary information and therefore the combination of the two can provide more consistent retrievals (Baran and Francis 2004a).

In this chapter, two different RTM-based retrieval methods are developed and evaluated. According to the characteristics of optically thin cirrus clouds, an appropriate RTM and corresponding inverse method will be suggested to provide retrieved information for further studies. The chapter is organized as follows. Section 4.2 gives

sensitivities of the VIS/SWIR and IR observations to different parameters, such as, cloud properties, cloud height, atmospheric profiles, surface emissivity and reflectivity, and the cloud microphysical parameterization scheme. Section 4.3 introduces the retrieval algorithm and Section 4.4 gives the comparisons of retrieved cloud properties based on the two RTMs and microphysical parameterization schemes. The summary and conclusion will be given in Section 4.5.

4.2 Sensitivity studies

In this section, we investigate the sensitivity of RTM simulations to both ice cloud properties and other major model parameters. Here, ice cloud properties include cloud optical thickness (τ), effective particle size (D_{eff}), habits and roughness of cloud particles; while model parameters include atmospheric temperature, humidity, and gas concentration profiles, cloud geometric locations, albedo, emissivity, and temperature of the surface (Watts et al. 2011). The two fast RTMs discussed in the previous two chapters, i.e., the shortwave RTM (hereafter referred to as SRTM, Wang et al. 2013b) and the high-spectral resolution infrared RTM (HRTM) are used to conduct the sensitivity studies. Since the sources of radiation that the two RTMs taking into account are totally different, the critical parameters that have most sensitivities to the model simulations are different. For instance, in the thermal infrared spectral region the surface emission contributes a lot to the satellite observed radiance at the TOA. For this reason, the surface temperature and emissivity, which determine how much energy emitted from the surface, are important in the HRTM. However, in the shortwave spectral region, reflected solar radiation is the major source contributing satellite observed radiance,

which is actually independent of the surface temperature and emissivity. Ice cloud properties and the major model parameters that are considered in this chapter are listed in Table 4.1.

Table 4.1 Ice cloud properties and model parameters employed in the sensitivity studies.

Variable Type	Variable Name		
Cloud Properties	Cloud Optical Thickness	Effective Particle Size	Habits and Degree of Roughness
Model Parameters (SRTM)	Gas Concentration	Surface Albedo	Cloud Height
Model Parameters (HRTM)	Gas Concentration Temperature Profile	Surface Temperature	Cloud Height

4.2.1 Overall information

To conduct sensitivity studies, we applied different ice cloud properties and model parameters. Only single-layer ice cloud cases are considered for simplification. Different cloud optical thicknesses, and effective particle sizes are pre-determined for the two models, which are listed in Table 4.2 in details. Furthermore, to investigate the impacts from the habits and roughness of ice crystals on model simulations, we employ

9 different habits (i.e., solid and hollow columns, droxtals, plates, small and large aggregates of plates, solid and hollow bullet rosettes, and aggregates of solid colums) and 3 degrees of particle surface roughness (see Table 4.2 and Fig. 4.1). Ice crystals with each of the habits and degrees of surface roughness satisfy the gamma distribution (Kosarev and Mazin 1991; Mitchell 1991; Heymsfield et al. 2002; Baum et al. 2005a), which is defined as follows:

$$N(D) = N_0 D^{\mu} \exp(-\lambda D), \tag{4.1}$$

where D is the maximum dimension of ice crystal, N is the number of ice crystals with maximum dimension between D and $D+\Delta D$, N_0 is the intercept, λ and μ are the slope and dispersion, respectively.

The latest database (Yang et al. 2013) of ice crystal single scattering properties includes different ice crystal habits and degrees of surface roughness, and updated refractive indices of ice crystal (Warren and Brandt 2008) in the spectral region from ultraviolet (UV) to far infrared (i.e., 100 μm). A combination of two numerical approaches, i.e., the Amsterdam discrete dipole approximation (ADDA, Yurkin and Hoekstra 2011) and the improved geometric optics method (the new IGOM, Bi et al. 2009) are used to calculate the single scattering properties of small (size parameter $\chi <$ 20) and large ($\chi > 20$) ice crystals. Here the size parameter is defined as:

$$\chi = \frac{2\pi r}{\lambda}. \tag{4.2}$$

Several improvements over previous databases (Yang et al. 2000, 2005) are included in this latest one. For example, Bi et al. (2008) introduced a new approach to

remove a "delta-transmission" parameter to make the physical meaning clearly; a more efficient beam-splitting technique (Bi et al., 2011b) is applied to calculate the near electric field instead of the time consuming Monte Carlo ray tracing technique employed in the previous IGOM (Yang and Liou 1998); and improved approaches to reduce errors from the near-to-far field mapping and backward scattering (Bi et al. 2009; 2011a). The effect of ice crystal surface roughness is also considered using the IGOM (Yang et al. 2013). A sea surface model is employed to simulate the surface structure of ice crystal. A normal distribution of slopes of small facets on ice crystals are defined as follows (Cox and Munk 1954):

$$P(X,Y) = \frac{1}{\sigma^2 \pi} \exp\left(-\frac{X^2 + Y^2}{\sigma^2} \right), \tag{4.3}$$

where X and Y are the slope variations of the surface in two orthogonal directions, and σ is the roughness parameter. A large σ indicates roughened surface, and if σ is 0 the surface is perfectly smooth. In our sensitivity studies, three degrees of surface roughness are included (see Table 4.2).

Ice clouds (1 km physical thickness), are insert into 6 different typical atmospheric profiles (McClatchey et al. 1971) and locate on five different levels ranging from 5 km to 15 km. The 6 profiles include the United State standard, tropical, mid-latitude summer, mid-latitude winter, high-latitude summer, and high-latitude winter. For simplification, CO_2 and O_2 are considered to be well-mixed gases with concentrations 385 and 2.09×10^5 ppmv, respectively. Note that surface temperatures from the 6 representative profiles span a wide range from 257 to 300 K. 5 Lambertian

surfaces with different albedo values (i.e., 0, 0.05, 0.1, 0.3, 0.5) are considered for simplification. The surface emissivity in IR region is assumed to be 0.98. Fig. 4.2 depicts the differences of the six profiles in temperature, humidity, and O_3 concentration.

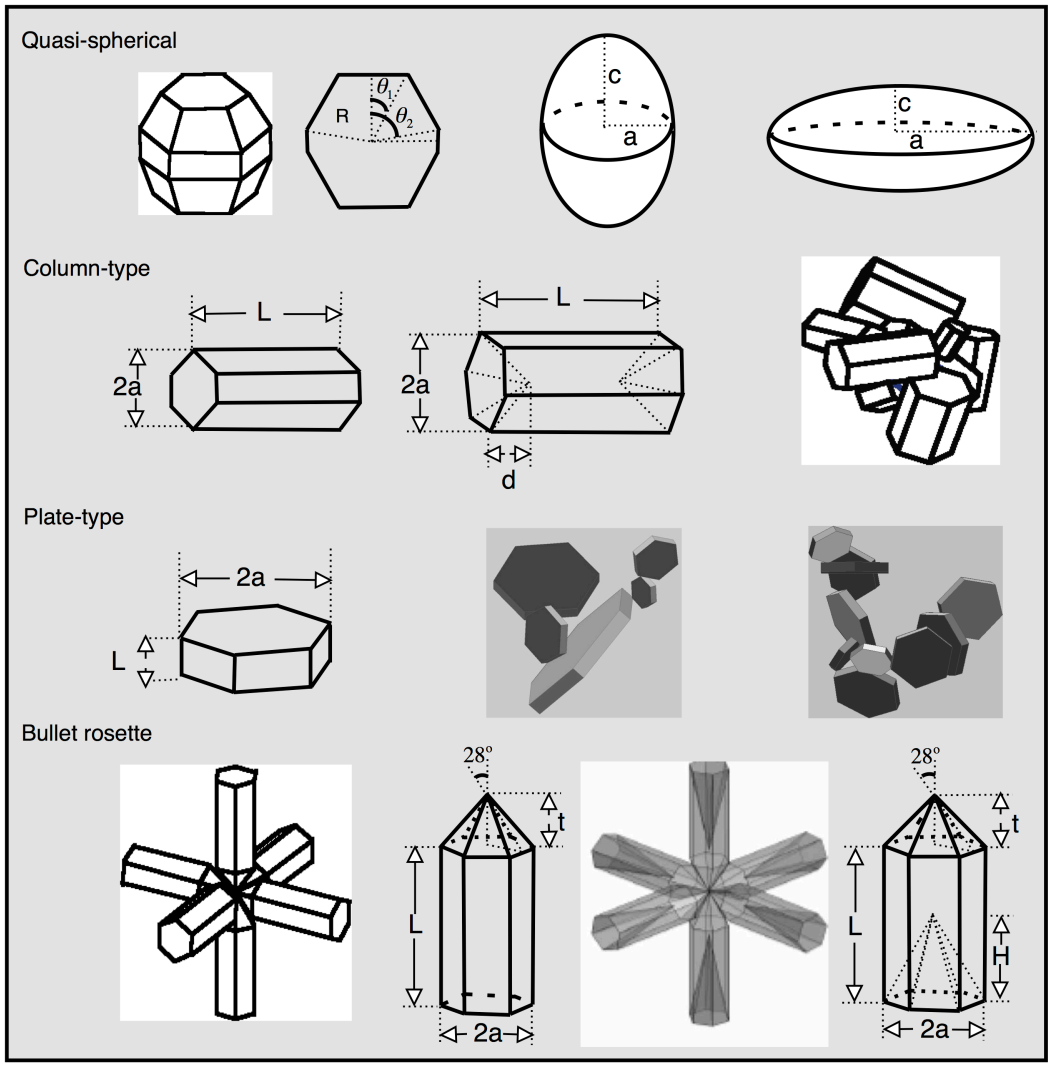

Fig.4.1 Habits of ice crystals (from Yang et al., 2013).

Table 4.2 Details of ice cloud properties and model parameters.

Variable Name	Variable Values or Description
Cloud Optical thickness	0.1, 0.2, 0.5, 1.0, 2.0, 3.0, 5.0, 10.0, 20.0, 50.0
Effective Particle Size (μm)	10, 20, 30, 40, 50, 60, 70, 80, 90, 100
Habit	Solid/Hollow Column, Solid/Hollow Bullet Rosette, Droxtal, Plate, Small/Large Aggregate of Plates, Aggregate of Solid Columns
Roughness Parameter	0, 0.03, 0.05
Cloud Height (km)	5.0, 7.5, 10.0, 12.5, 15.0
Surface Temperature (K)	257, 272, 287, 288, 294, 299 (From Atmospheric Profiles)
Surface Albedo (SRTM)	0, 0.05, 0.1, 0.3, 0.5
Surface Emissivity (HRTM)	0.98
Atmospheric Profile	U.S. Standard, Tropical, Mid-Latitude Summer, Mid-Latitude Winter, High-Latitude Summer, High-Latitude Winter
Water Vapor	From Atmospheric Profiles
Ozone	From Atmospheric Profiles
Carbon Dioxide (ppmv)	385
Oxygen (ppmv)	2.09×10^5

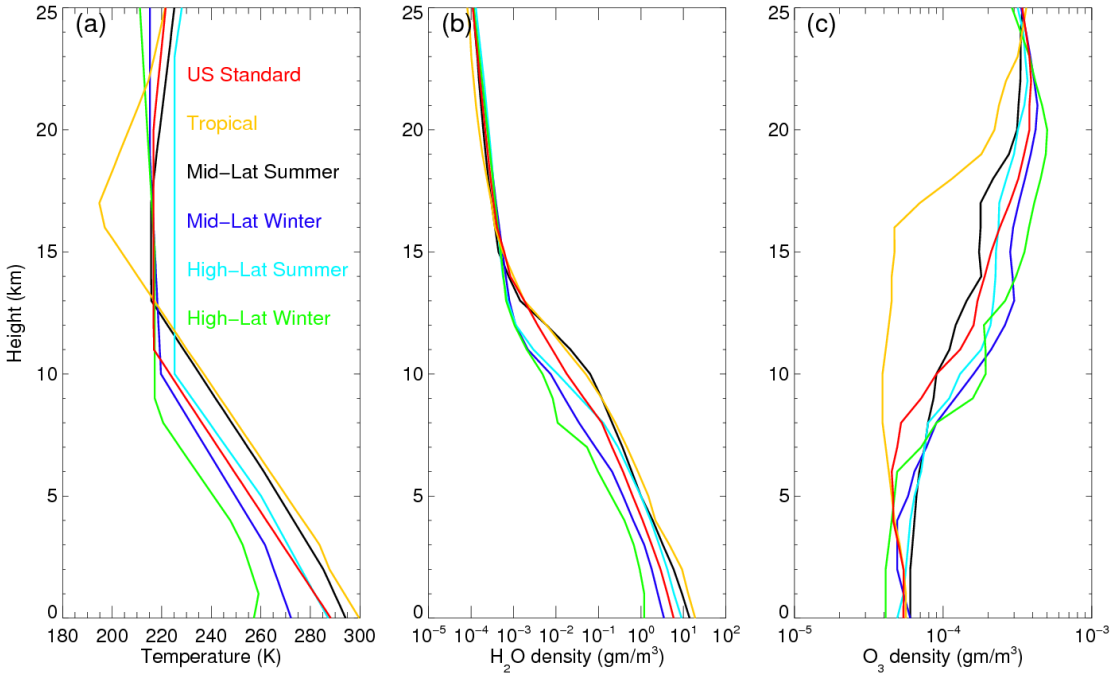

Fig.4.2 Six standard atmospheric profiles (McClatchey et al. 1971) as a function of height: (a) temperature profiles, (b) water vapor density profiles, and (c) O_3 density profiles.

4.2.2 Sensitivity studies in the shortwave regime

Satellite-based passive instruments, such as the MODIS and the Spinning Enhanced Visible and Infrared Imager (SEVIRI, Schmetz et al. 2002), observe reflected solar radiance at the TOA. The observations include the impacts from clouds, the surface, atmosphere, and solar-viewing geometries. To deduce cloud properties from the reflectivity observations, one can expect that the optimal channels have large sensitivity to cloud and less sensitivity to the environment, such as gas concentrations and surface

reflection. Fig. 4.3 (a) and (b) show the real and imaginary parts of ice crystal refractive indices in the visible through near infrared spectral region, respectively (Warren and Brandt 2008). The real part of ice refractive index decreases slowly as the increase of wavelength, whereas the imaginary part significantly increases in the same spectral region. A two-channel reflectivity method (Nakajima and King 1990) was developed based on the reflection and absorption features of ice crystal. Cloud reflectivity observations in this spectral region are simultaneously employed to infer cloud properties based on this two-channel reflectivity method (e.g., Arking and Child 1985; Platnick and Twomey 1994; Platnick et al. 2001; King et al. 2003). A non-absorptive band with wavelength less than 1.5-μm is selected to give maximum sensitivity of reflectivity to cloud optical thickness. Normally, the Band1 and Band2 (0.64- and 0.86-μm) of the MODIS instrument are considered to be the non-absorptive channels for cloud retrievals over land and over ocean, respectively (Platnick et al. 2003). The Band2 is primary used for oceanic clouds because of the strong absorption of water in this channel gives relatively small surface albedo (Morel 1974). The Band6 and Band7 are frequently selected as the absorptive channel in the retrieval method because the imaginary parts of ice refractive indexes in the two channels are approximately more than 2 orders of magnitude higher than in Band1, Band2 and Band5 (see Fig. 4.3). Fig. 4.4 shows the clear-sky transmissivity spectrum of a mid-latitude summer atmosphere calculated using the LBLRTM. The MODIS channels discussed above are not located in the clear-sky absorptive bands (except Band26) to maximize the sensitivity of

observations to cloud. Reflectivity in a narrow channel of the MODIS is defined as follows:

$$R_{modis,TOA} = \frac{\int_{\Delta\upsilon} R_{TOA}(\upsilon) r(\upsilon) S(\upsilon) d\upsilon}{\int_{\Delta\upsilon} r(\upsilon) S(\upsilon) d\upsilon}, \tag{4.4}$$

where R is the reflectivity at the TOA, S is the incident spectral solar spectrum, and r is the instrument response function.

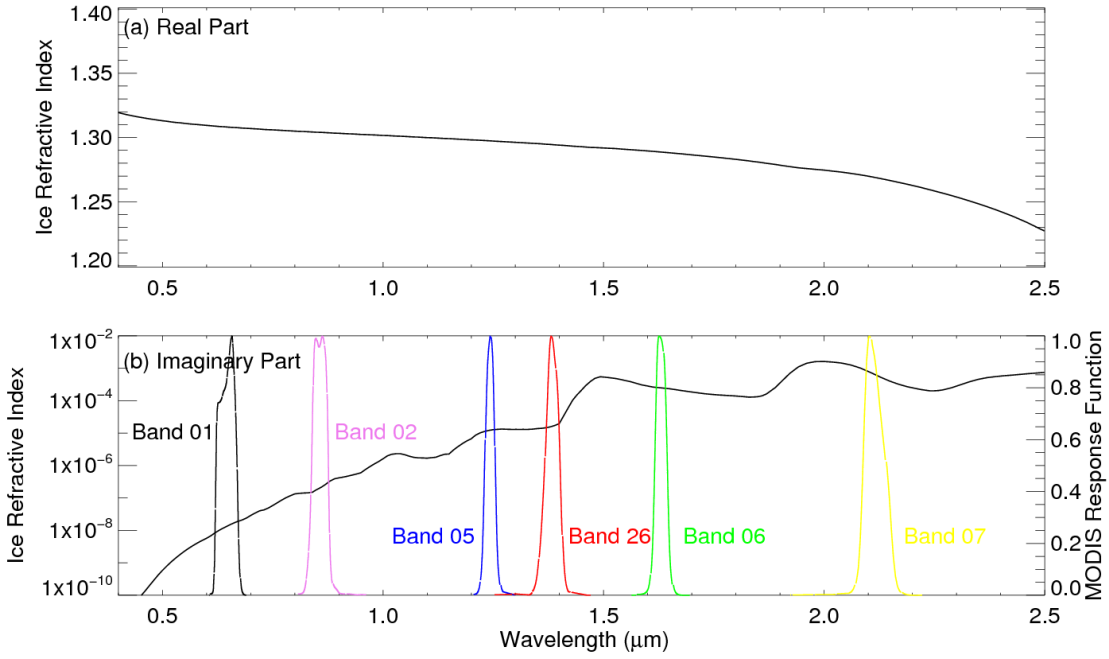

Fig.4.3 Real (a) and imaginary (b) parts of ice crystals in a spectral region from 0.4 to 2.5 μm. The delta function-like curves represent the response functions of 6 MODIS channels. The ice crystal refractive indices data are available online: (http://www.atmos.washington.edu/ice_optical_constants/).

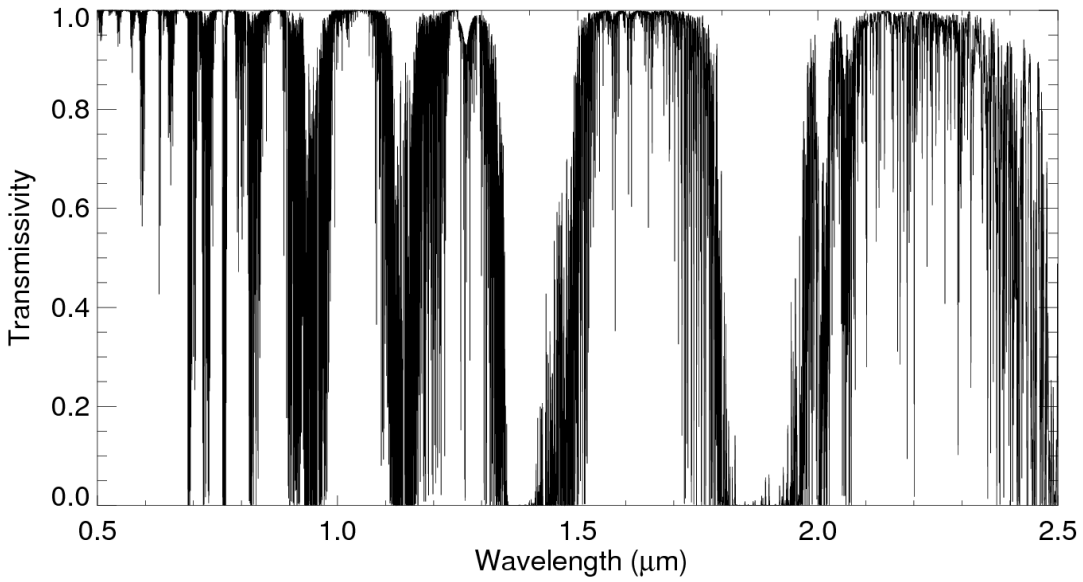

Fig.4.4 Clear-sky transmissivity spectrum of the mid-latitude summer atmosphere. Calculation is conducted using the LBLRTM.

Fig. 4.5 shows an example of the two-channel reflectivity method. The Band2 and Band7 of the MODIS are employed in this example. It shows that the reflectivity in the non-absorptive channel is approximately a function of optical thickness and the absorptive channel can be impacted by effective particle size. The figure shows that the reflectivities in the two channels are close to 0 and converge together when cloud is optically thin ($\tau < 1$).

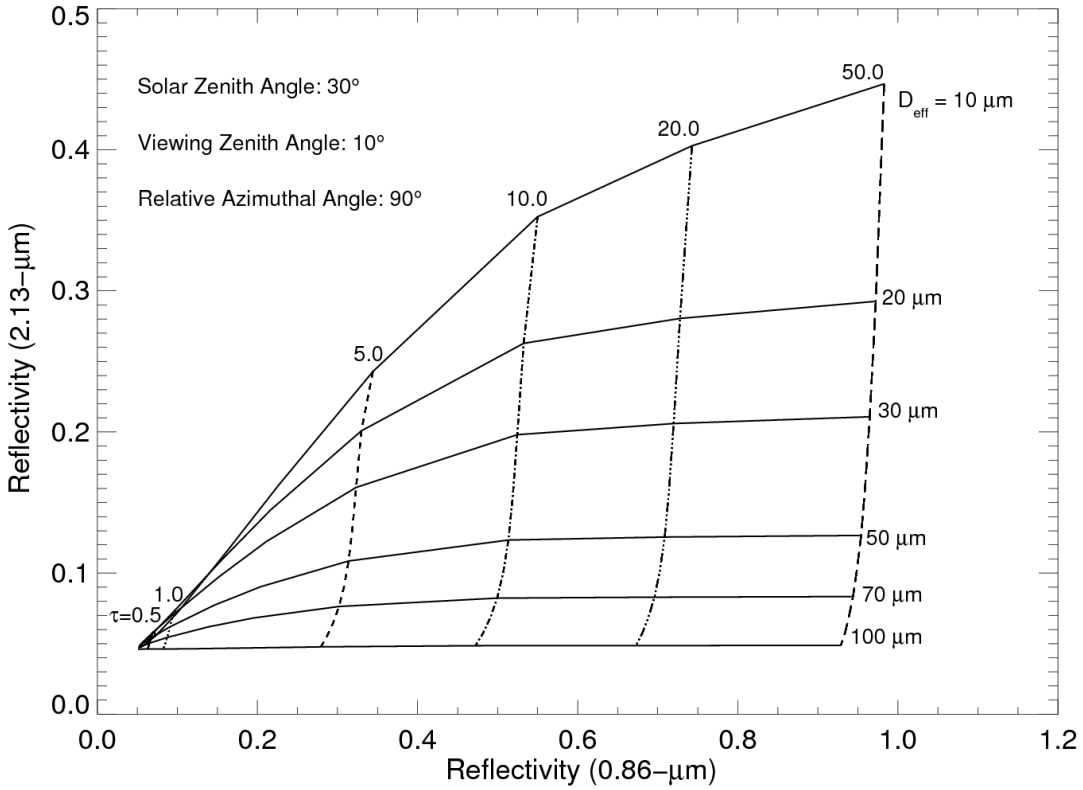

Fig.4.5 Relationship between the MODIS Band2 (0.86-μm) and Band7 (2.13-μm) reflectivities for ice clouds. A Lambertian surface is assumed with albedo 0.05 for the two channels. The solar zenith angle and viewing zenith angle are 30° and 10°, respectively. The solid curves indicate constant effective particle sizes, and vertical (dotted or dashed lines) indicate constant optical thickness values. Ice cloud particles are assumed to be smooth solid columns and the size distribution is the gamma distribution (Kosarev and Mazin 1991). The U.S. standard atmosphere is used to conduct the calculation.

Fig. 4.6 shows sensitivity of the MODIS Band2 and Band7 reflectivity observations to different surface albedo values. The surface albedo has significant impact on the reflectivities in the two channels if τ is smaller than 10. However, if cloud

is optically thick (i.e., $\tau > 20$), different colored meshes generally coincide with each other because a large portion of incident solar radiation are reflective back to the space and therefore the impacts of surface reflection are ignorable. For retrieval of thin cirrus clouds or aerosol layers with τ less than 1, the selection of the combination of two shortwave channels must be careful. For example, in order to retrieve the optical thickness of aerosol over desert region, which has high surface reflectivity in the visible and near infrared spectral region between 0.6 and 2.5 μm, Hsu et al. (2004; 2006) developed the Deep Blue method, which replaces the MODIS Band1 (0.64-μm) with Band3 (0.47-μm). Desert surfaces have low surface reflectivity in Band3, which helps mitigate the surface impact.

From Fig. 4.3 and Fig. 4.4, we find that most MODIS shortwave channels are designed to avoid strong gas absorption to maximize signals from the objects of interest. It can be expected that the reflectivities in these channels are profile and cloud height insensitive except the MODIS Band26, which locates in a strong water vapor absorption band. Fig. 4.7 shows sensitivity of the MODIS Band26 reflectivity observation to different cloud top heights (Fig. 4.7a) and representative atmospheres (Fig. 4.7b). Observation in Band26 of the MODIS shows strong sensitivity to cloud height: the TOA reflectivity decreases with the decrease of cloud top height. The Band26 reflectivity is less than 0.15 even if an optically thick cloud with τ =100 is put into a tropical atmospheric layer 5 km above the surface. Another interesting feature can be found in both of the two panels is that the surface is totally black in cloud-free case according to the observation of Band26, suggesting that this channel has less sensitivity to the surface

reflectivity. The difference in observations of ice clouds with different heights can be attributed to the variations of water vapor amount above the different cloud layers.

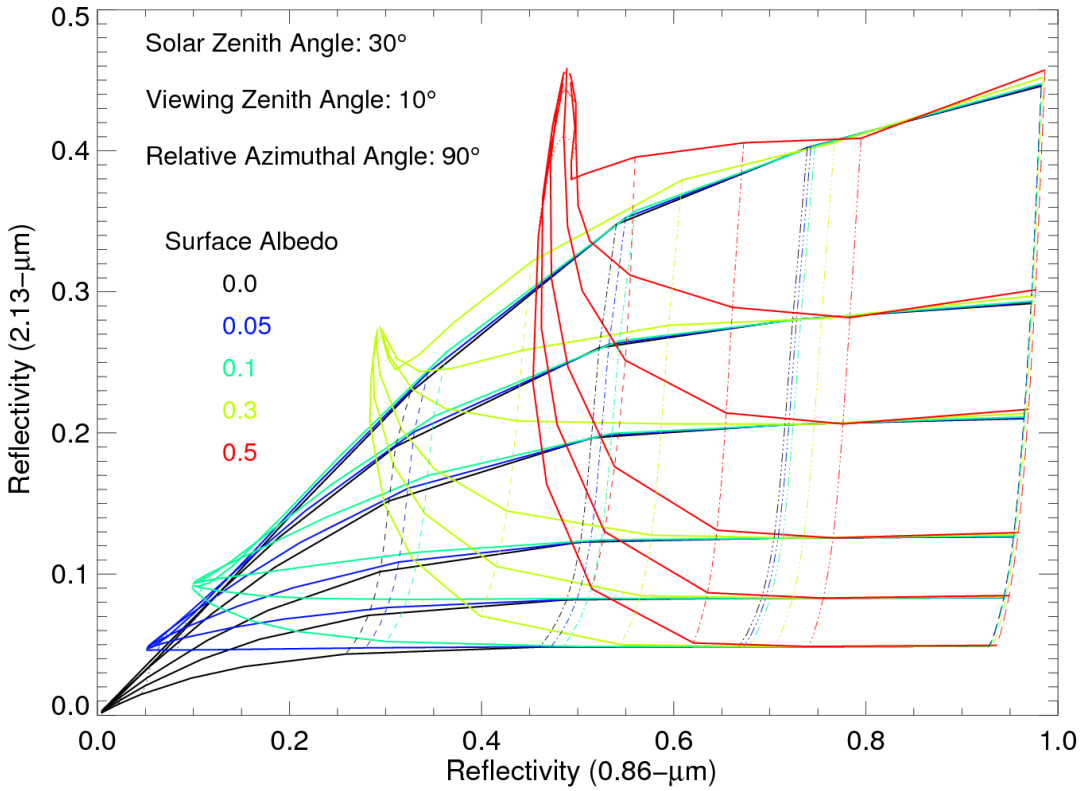

Fig.4.6 Relationship between the MODIS Band2 (0.86-μm) and Band7 (2.13-μm) reflectivities for ice clouds over different surfaces. Five Lambertian surfaces are assumed with albedo 0, 0.05, 0.1, 0.3, and 0.5. The other conditions are the same as in Fig. 4.5.

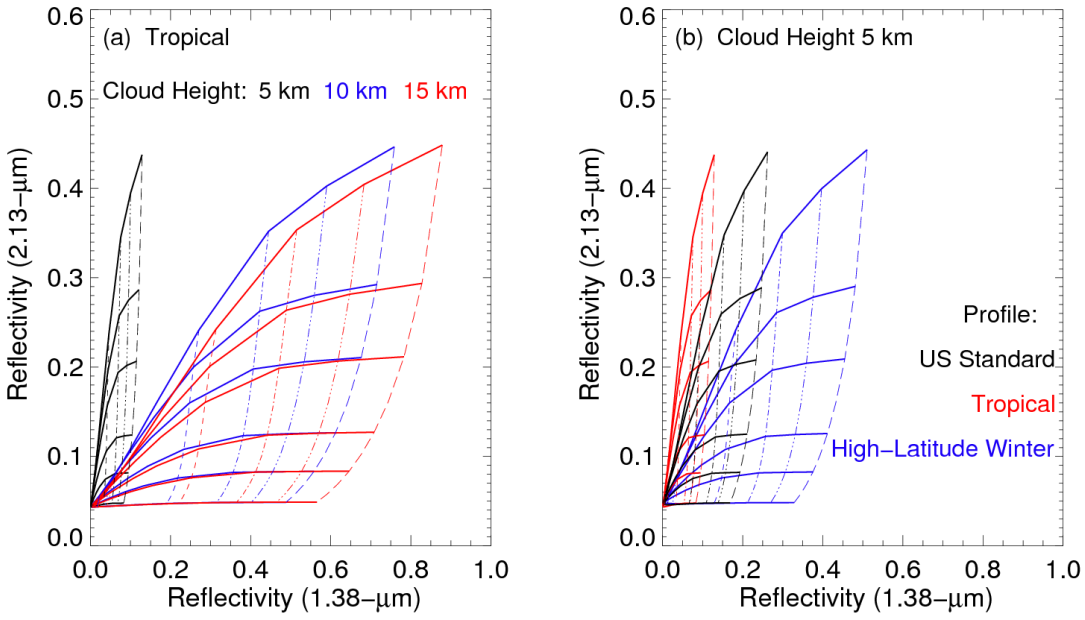

Fig.4.7 Relationships between the MODIS Band26 (1.38-μm) and Band7 (2.13-μm) reflectivities for ice clouds (a) with different altitudes and (b) in different atmospheres. The other conditions are the same as in Fig. 4.5.

Fig. 4.8 shows the impacts on the MODIS Band2 and Band7 observations from the degree of ice crystal surface roughness. Six typical habits are shown in six panels: (a) solid column, (b) solid bullet rosette, (c) aggregate of solid columns, (d) droxtal, (e) plate, and (f) hollow column. The scattering angles for the cases shown in this figure are 120°. Generally speaking, the bi-channel reflectivity meshes exhibit sensitivities to the degree of surface roughness. However, investigating different habits, such as the solid column (panel a) and plate (panel e), one can find that the mesh is more sensitive to

habit. For some habits, such as the aggregate and droxtal, the curves of constant τ and constant D_{eff} are orthogonal to each other if cloud is optically thick. However, for some other habits, such as the solid bullet rosette and plate, the constant τ curves are no longer vertical, suggesting the reflectivites in the MODIS Band2 calculated using these habits still depend on D_{eff}. D_{eff} is defined as the ratio of the total volume and the total projected area (Eq. 1.3). To obtain the same D_{eff} values, loose particles (such as plates and solid bullet rosettes) with larger D (the maximum dimension) are required in comparison with compact particles (such as aggregates of solid columns and droxtals). Therefore, less energy can be reflected due to the strong forward scattering peak caused by large particles.

The impacts of different habits and degrees of surface roughness also depend on the scattering angle. Fig. 4.9 shows the scattering phase functions of the 6 habits with 3 degrees of surface roughness. Ice crystal surface roughness clearly affects the phase function of each of the habits. In comparison with the phase function differences at 120°, relatively larger discrepancies occur in the backward directions (i.e., near 180°) for solid column, solid bullet rosette, aggregate of eight solid columns, and plate. Fig. 4.10 shows the bi-channel meshes for the same habits as shown in Fig. 4.8, but the scattering angles for these meshes are 180°. Comparing with Fig. 4.8, the meshes at 180° scattering angles show relatively larger differences between smooth and severely roughened particles. However, the two-channel mesh is still more sensitive to ice crystal habit.

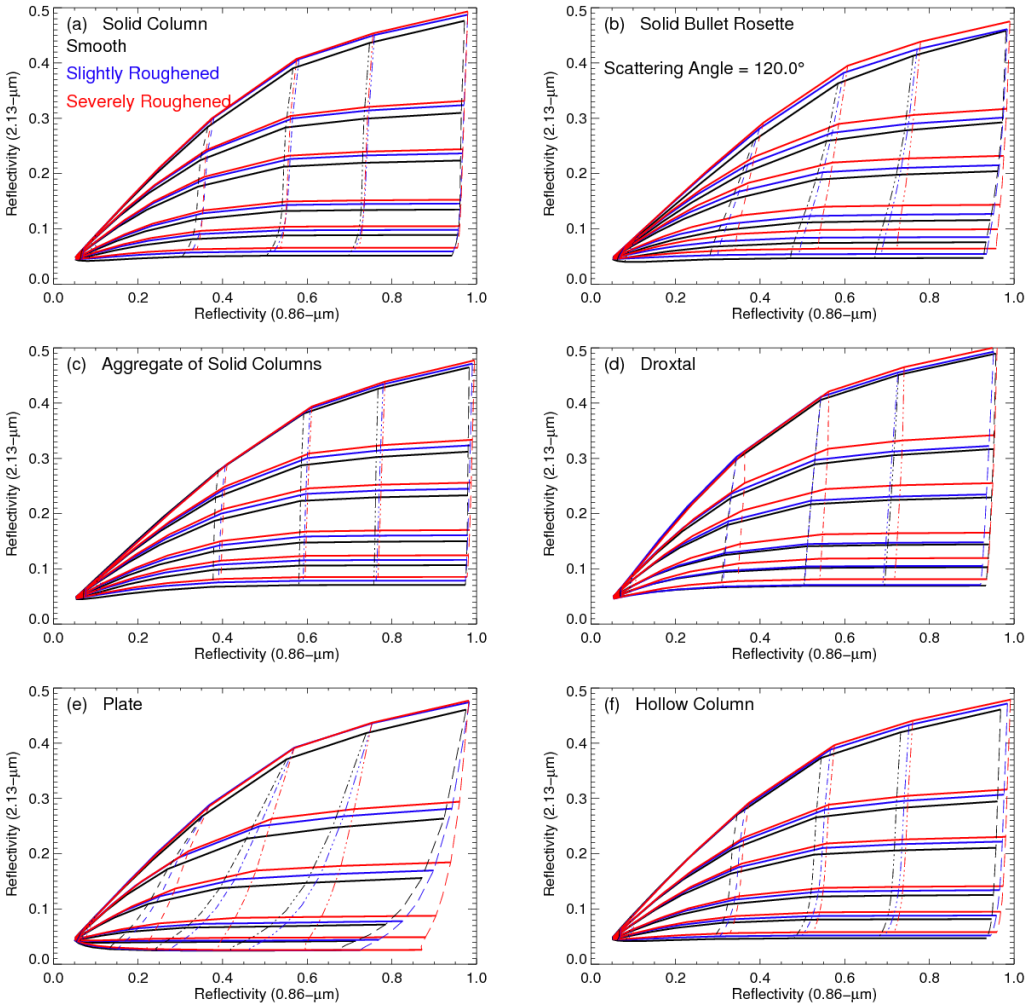

Fig.4.8 Sensitivities of the bi-channel mesh to ice particle habit and degree of surface roughness. Each panel shows a typical habit of ice crystal. Three degrees of surface roughness are considered. Both solar zenith angle and viewing zenith angle are 30°. The relative azimuth angle is 0° and therefore the scattering angle is 120°. The other conditions are the same as in Fig. 4.5.

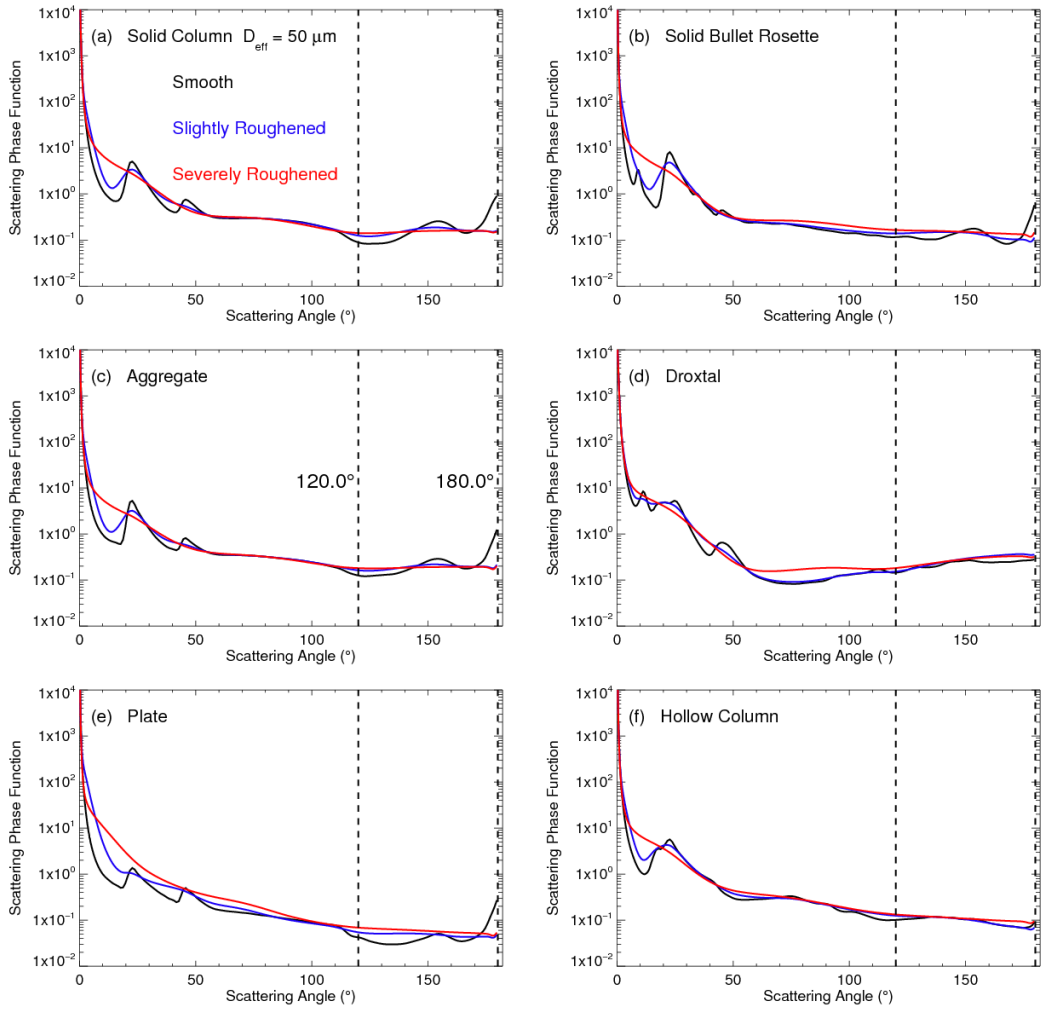

Fig.4.9 Scattering phase functions of ice crystals for 6 habits. Three degrees of surface roughness (smooth, slightly roughened, and severely roughened) are differentiated with black, blue and red curves. The effective particle sizes are 50 μm. The two vertical dashed lines in each panel mark the locations of two scattering angles: 120° and 180°.

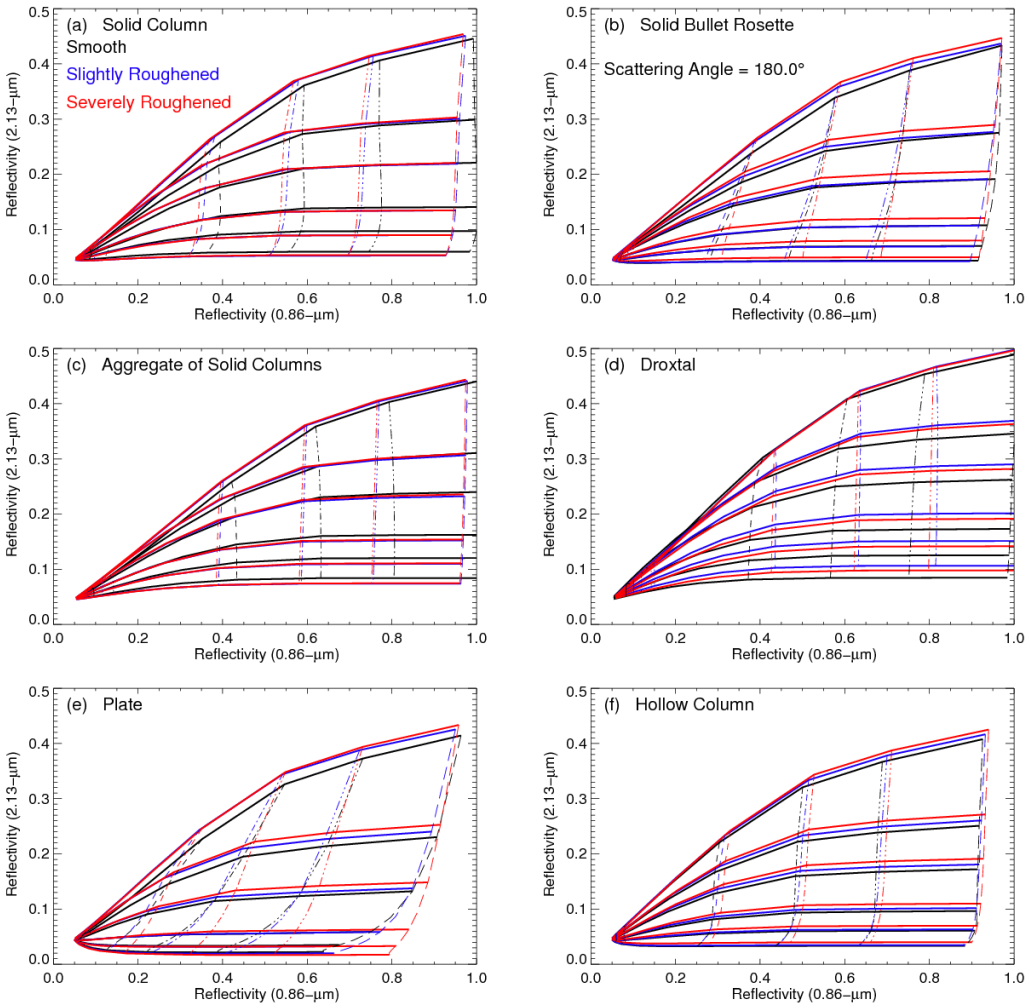

Fig.4.10 Same as Fig. 4.8, but the relative azimuth angles are 180°, and therefore the scattering angles are 180°.

Except the Band26, the other MODIS shortwave channels designed for cloud study are insensitive to atmospheric type and cloud height (i.e., water vapor concentration above cloud). Surface albedo, ice crystal habit and degree of surface

roughness, however, have much more impacts on the shapes of these two-channel meshes. Generally, surface albedo has the largest impact on cloud retrievals if the cloud is optically thin. The habit distribution and degree of surface roughness impact cloud retrievals throughout the whole ranges of cloud optical thickness and effective particle size. It is difficult to conclude the use of assumption that ice cloud particles are severely roughened increases (or decreases) retrieved cloud optical thickness. In fact, the impact from degree of surface roughness is highly dependent on the assumption of habit distribution, the scattering angle, and the whole range of phase functions since multiple scattering are important for most of the cases. For example, the phase function value of smooth solid columns is smaller than the severely roughened solid columns at 120° (Fig. 4.9a). Therefore, the retrieved τ using smooth solid columns must be higher than the retrieved τ using roughened solid columns because the retrieval scheme has to use a larger τ to match the same reflectivity observation. This can be also found by investigating the panel (a) in Fig. 4.8: the black dashed curve (smooth) of a τ value is on the left side of red dashed curve (severely roughened). However, at 180°, phase function of smooth solid columns is much higher than its roughened counterpart, resulting in smaller τ retrievals in comparison with roughened solid columns in this geometry (see Fig. 4.10a).

4.2.3 Sensitivity studies in the thermal infrared regime

Ice crystals are strongly absorptive in the IR regime in comparison with the shortwave region. Fig. 4.11 (a) and (b) show the real and imaginary parts of ice crystal refractive indices, respectively (Warren and Brandt 2008). The imaginary part of ice

crystal index reaches the maximum (larger than 0.4) around 12 μm (i.e., approximate 800 cm^{-1} in Fig. 4.11), which is 5 orders (3 orders) of magnitude higher than in the visual regime (near-infrared regime). For this reason, in the thermal IR regime, emission and absorption are dominant within an ice cloud layer.

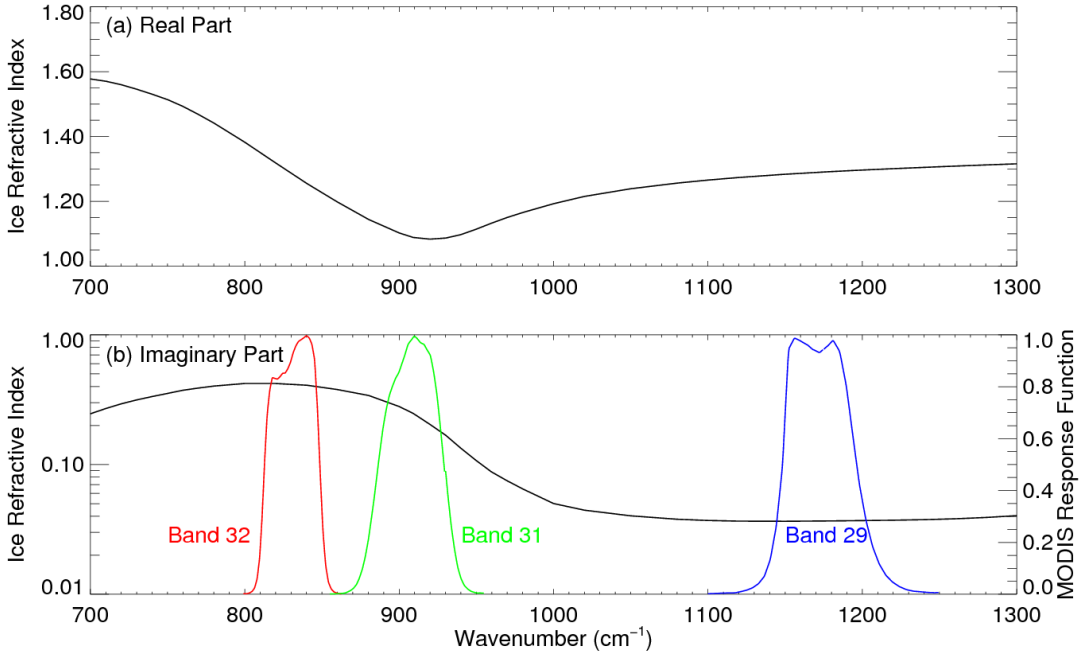

Fig.4.11 Real (a) and imaginary (b) parts of ice crystals in a spectral region from 700 to 1300 cm^{-1} (black curves). The colored curves represent the response function of 3 MODIS channels. The ice crystal refractive indices data are available online:(http://www.atmos.washington.edu/ice_optical_constants/).

The sensitivity of TOA BT spectrum to ice cloud properties is investigated for a case of a mid-latitude summer atmosphere with a single ice cloud layer on 10 km (see Fig. 4.12). The surface is considered to be Lambertian with temperature 299 K and emissivity 0.98. The viewing zenith angle is 0°. Several features are worth noting in Fig. 4.12. First, as expected, the TOA BT spectrum is highly sensitive to τ, especially in the scenes including optically thin ($\tau < 1$) or moderately thick ($\tau \sim 3$) ice clouds, as shown in Fig. 4.12a. Generally speaking, TOA BTs decrease with an increase of τ until they approach the cloud-top temperature. An exception can be observed in the strong absorption bands of CO_2 and O_3. The TOA BTs at the center of absorption lines can be higher than the cloud top physical temperature even if τ is large enough. This is due to the thermal emission of these absorptive species in stratosphere with a relatively high temperature. Second, the slope of the TOA BT spectrum in the region between 800 and 960 cm^{-1} is sensitive to D_{eff}, especially for ice clouds consisting of small ice particles, shown if Fig. 4.12b. Note that the slope decreases rapidly and approaches 0 once D_{eff} exceeds 50 μm (see the two panels in Fig. 4.12).

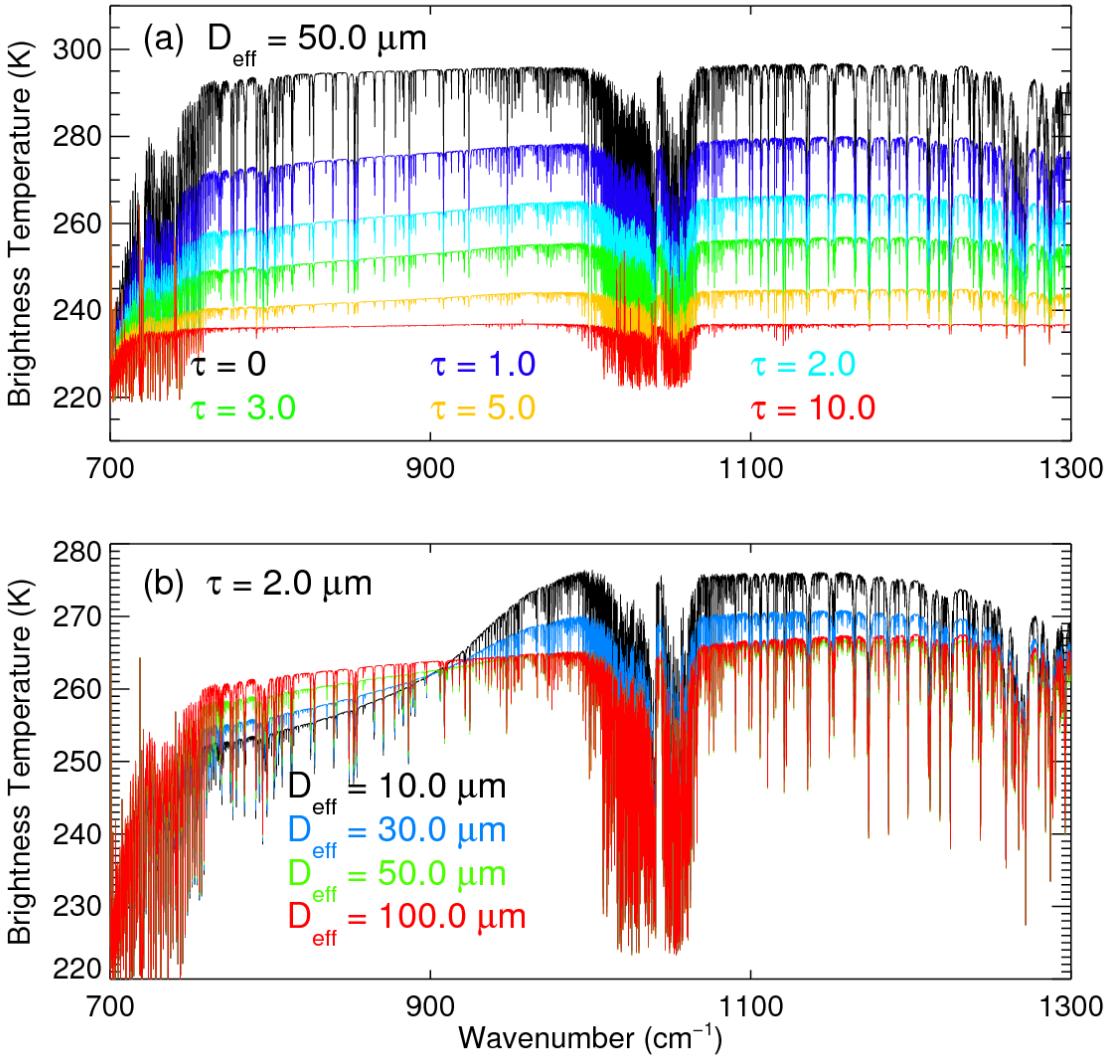

Fig.4.12 Sensitivity of model simulated TOA BT spectrum to cloud optical thickness (τ) and effective particle size (D_{eff}). A mid-latitude summer profile is used for this calculation. Surface temperature is 299 K and emissivity is 0.98. The viewing zenith angle is 0°. The cloud top height is 10 km and cloud physical thickness is 1 km. Ice crystals are assumed to be smooth solid columns with a gamma size distribution.

The satellite-observed TOA BTs in narrow channels, such as the MODIS, can be also simulated as discussed in Chapter 3. Different from the Eq. 3.18, which is suitable for high-spectral resolution instruments, the MODIS observed radiances in the thermal infrared channels are calculated as follows:

$$I_{modis,TOA} = \frac{\int_{\Delta\upsilon} I_{TOA}(\upsilon) r(\upsilon) B(\upsilon) d\upsilon}{\int_{\Delta\upsilon} r(\upsilon) B(\upsilon) d\upsilon}, \tag{4.5}$$

where B indicates the Planck function and I represents the upwelling radiance at the TOA. The infrared channel of MODIS always spans hundreds of wavenumbers (Fig. 4.11), and therefore the variations of the Planck function within MODIS channels are considered for accuracy.

Fig. 4.13 shows simulated TOA BTs in three MODIS infrared channels (8.5, 11, and 12 μm) and their differences. The six colored lines represent ice clouds with six effective particle sizes ranging from 10 to 100 μm. The cloud optical thickness ranges from 0 at a warmer BT (at 11 μm) to 10 at a colder BT. For each effective particle size, the TOA BT decreases rapidly with increasing τ until τ reaches 10 at which the cloud layer essentially becomes opaque. Similar to the conclusions deduced from the BT spectrums (Fig. 4.12), the narrow channel results also demonstrate that the positive BT differences (BTD) between the 8.5- and 11- or 12-μm channels are highly sensitive to D_{eff} for semi-transparent and transparent ice clouds consisting of small particles. Comparing the two panels in Fig. 4.13, the BT differences between the 8.5- and 12-μm channels are larger, because ice crystal absorption reaches its maximum near 12 μm.

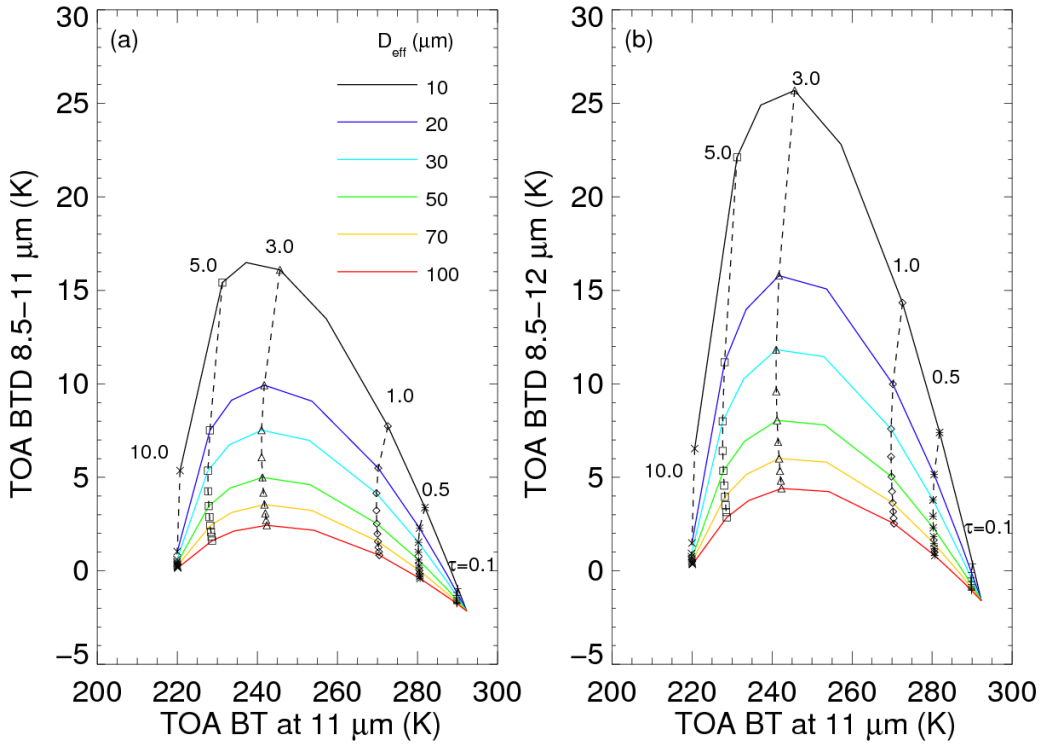

Fig.4.13 Sensitivity of model simulated TOA BT in three MODIS channels (8.5-, 11-, and 12-μm) to cloud optical thickness (τ) and effective particle size (D_{eff}). The other conditions are the same as in Fig. 4.12.

It can be expected that, if only TOA BTs or BTDs between two IR channels are involved, the retrieval of τ is more accurate than the retrieval of D_{eff}. This is due to the different sensitivities of a BT-τ pair and a BT difference-D_{eff} pair, which can be inferred from comparing the ranges of TOA BTs and BTDs from Fig. 4.13. For example, in the case shown in Fig. 4.13, BTs vary from approximately 240 to 300 K when τ decreases

from 5 to 0, whereas BT difference varies within 10~20 K even if D_{eff} varies from 10 to 100 μm.

Fig. 4.14 shows the comparisons of simulated BT-BTD arches (as shown in Fig. 4.13) between three cloud heights: 5, 10, and 15 km, which are depicted by using red, blue, and black curves. The panels a to f show comparisons conducted based on the 6 typical atmospheric profiles. Three features are worth noting in Fig. 4.14. First of all, for most cases, the BT-BTD arches are sensitive to the cloud physical height, especially for tropical and mid-latitude summer profiles (panel b and c). For mid-latitude winter and high-latitude profiles (panel d, e, and f), it is difficult to differentiate the arches between clouds with physical heights 10 and 15 km, which can be attributed to the small temperature differences between the two levels for the high-latitude winter cases. The temperature profiles of the 6 typical atmospheric columns show that the tropical and mid-latitude summer profiles have large temperature lapse rates even if the altitude is higher than 10 km. On the contrary, the other profiles, in particular the high-latitude winter profile, exhibit small temperature lapse rates or even constant temperatures if ice cloud altitudes are higher than 10 km. Second, the higher ice cloud is, the wider the arches span in the BT-BTD space, which is due to the large temperature difference between cloud and the surface. Hence, the narrowest arch occurs if a 5 km height cloud layer is located in a high-latitude winter atmosphere with surface temperature less than 260 K. Third, the simulations (arches) are not sensitive to the concentrations of absorptive gases such as water vapor. This conclusion can be inferred from investigating the clear-sky simulations of the 6 typical atmospheres. For example, for each

atmosphere, the BTDs between the MODIS two channels (8.5- and 12-μm) are close to 0 and the BTs at the 11-μm channel are close to the surface temperatures (a little bit smaller than the surface temperature due to the surface emissivity is 0.98 and the weak gas absorption).

Fig. 4.15 shows the comparisons of simulated BT-BTD arches between ice clouds consisting of smooth (σ = 0) and severely roughened particles (σ = 0.5), which are shown with black and red curves, respectively. Six different habits (panels a through f) are used to generate ice cloud bulk scattering properties by assuming that the particle size distribution satisfies the gamma distribution (Eq. 4.1). The mid-latitude summer atmosphere is used with surface temperature 294 K and the cloud height is 12.5 km. It shows that the simulations are insensitive to the degree of surface roughness. Furthermore, by comparing different habits, the arches are quite similar, suggesting that the TOA BT-BTD pairs are approximately independent of the details of individual ice crystals.

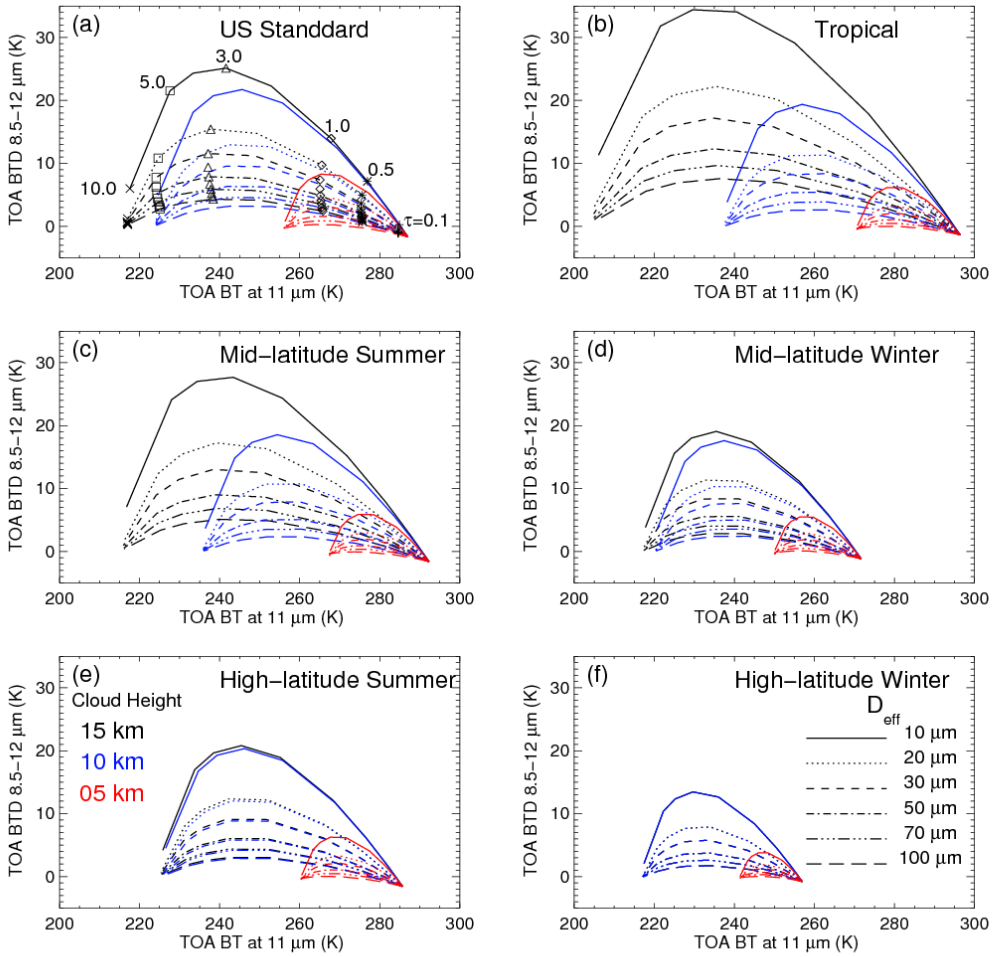

Fig.4.14 BT-BTD arches for ice clouds with different heights in the 6 typical atmospheres as shown in Fig. 4.2. The other conditions are the same as in Fig. 4.12.

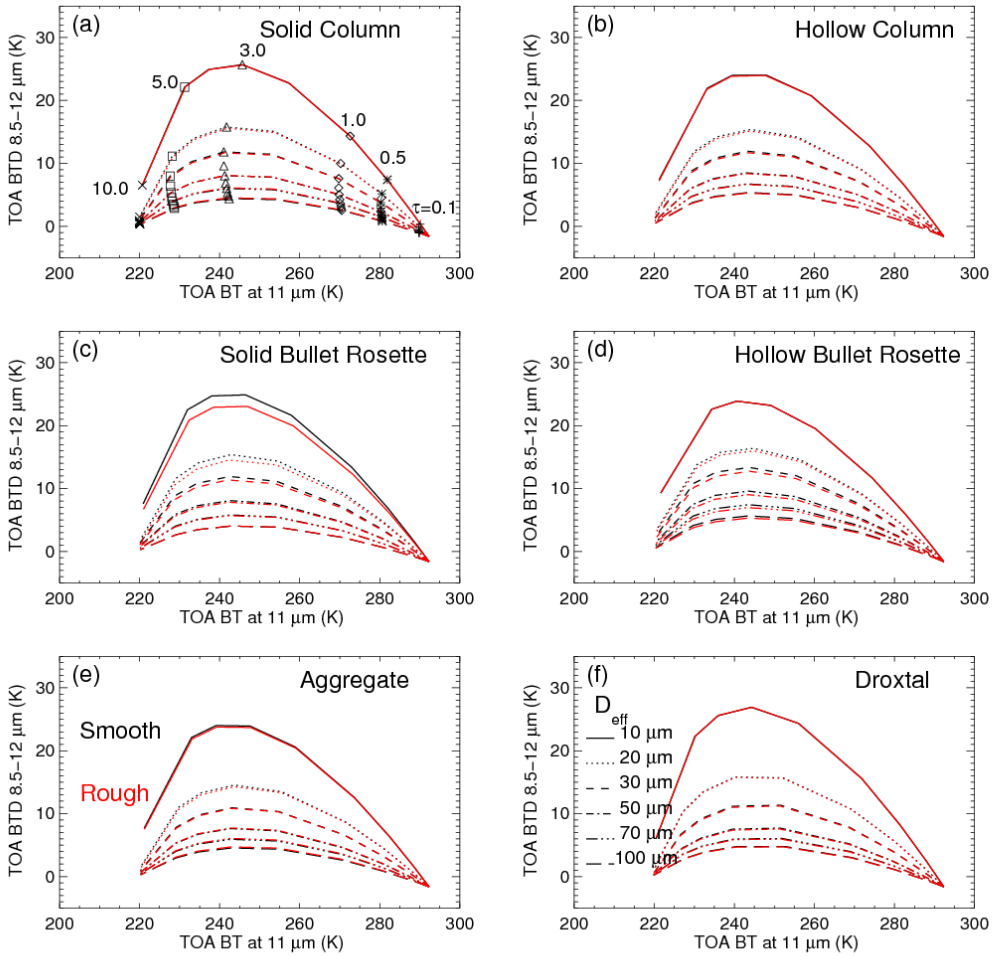

Fig.4.15 BT-BTD arches for ice clouds with different degrees of surface roughness (black: smooth particles with $\sigma = 0$; red: severely roughened particles with $\sigma = 0.5$) and habits. The mid-latitude summer profile is used and the surface temperature is 294 K. The cloud height is 12.5 km. The other conditions are the same as in Fig. 4.12.

Generally, the BT-BTD arch exhibits high sensitivities to different atmosphere profiles (surface temperatures) and cloud heights, but less sensitivities to both particle

habits and degrees of surface roughness. In comparison with the two-channel reflectivity meshes discussed in Section 4.2.2, the IR-based method has several limitations in cloud simulations and retrievals. For example, the BT-BTD pair has no sensitivity if cloud is optically thick and ice particles within the cloud layer are large. Additionally, temperature and humidity profiles, and cloud heights have large impacts on the model simulations. However, the IR-based method is applicable in both daytime and nighttime, which provides a possible approach to investigate the climatology of cloud properties. The TOA BTs have large sensitivities if cloud is optically thin and the BTDs are sensitive to the D_{eff} if both τ and D_{eff} are relatively small. Considering the features of the optically thin cirrus clouds (Jensen et al. 1996; McFarquhar et al. 2000; Dessler and Yang 2003; de Reus et al. 2009), the IR channels have inherent advantages to simulate and retrieve the optically thin cirrus clouds in comparison with the solar reflectivity channels. Meanwhile, the IR-based method shows less sensitivity to the degrees of surface roughness of ice crystals, leading to a smaller impact from the cloud microphysical parameterization schemes on the retrieval of ice cloud.

4.3 Retrieval of τ and D_{eff} using satellite observations

The computational efficiencies of both SRTM and HRTM facilitate the inference of ice cloud optical and microphysical properties from global satellite observations. This section contains the details of the model based retrievals, including the datasets used, the retrieval method, results, and comparisons of retrievals using different models and pre-assumed microphysical parameterization schemes.

4.3.1 Satellite datasets

Satellite data from Feb. 11th, 2008 are employed in the retrieval examples. To implement the model-based retrievals, satellite observations in the shortwave and infrared regimes, cloud geometric information, cloud thermodynamic phase, are provided by the satellites included in the afternoon satellite constellation, or "A-Train" for short (Stephens et al. 2002). The A-Train constellation, consisting of 6 polar orbiting satellites currently, provides continuous observations focusing on different components of the Earth-Atmospheric system. The quasi-simultaneous measurements from different instruments on board different platforms in the A-Train constellation allow people fetch multi-spectral and multi-directional information of the same target. As an important component in the A-Train constellation, the MODIS, on board *Aqua*, is a passive instrument that has 36 narrow spectral bands from visible to thermal IR region. The MODIS has the highest spatial resolution (i.e., 250 m) of Band1 (0.64-μm) and Band2 (0.86-μm), moderate spatial resolution (500 m) of Band3 through Band7, and coarse spatial resolution (1 km) for the rest channels at nadir view. For consistency, we extract satellite observations from the standard MODIS Level-1b 1 km spatial resolution product (MYD021KM), which aggregates the observations of Band1 through Band7 into 1 km pixels. In principal, the solar bi-directional reflectance observations in Band2 (0.86-μm) and Band7 (2.13-μm) are used to conduct the SRTM-based retrieval, and the BT observations in Band29 (8.5-μm), Band31 (11-μm), and Band32 (12-μm) are employed to implement the HRTM-based retrieval. Table 4.3 includes more details about the satellite-based and ancillary datasets used for cloud retrievals.

In addition to the MODIS, the CALIOP on board the CALIPSO is also used to provide vertical structures of cloudy atmospheres. Specifically, the CALIOP Level 2 cloud layer product with 1 km resolution is used to specify cloud geometric boundaries and thermodynamic phase to exclude the cases including multi-layered clouds and water (or mixed) phase clouds.

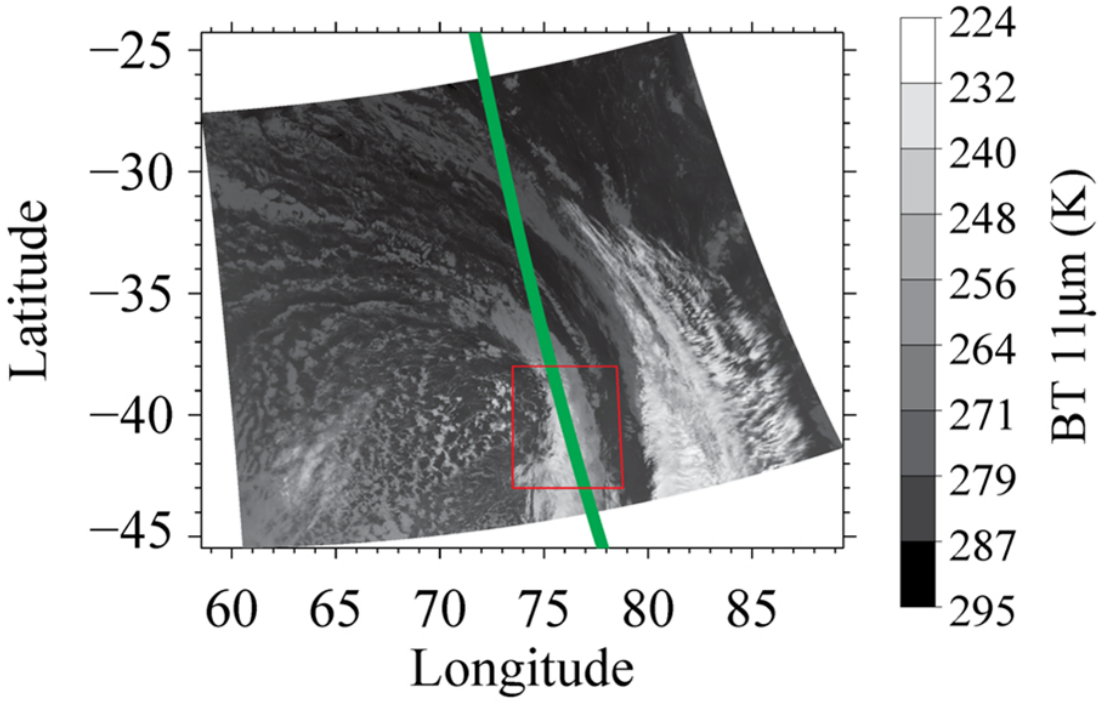

Fig.4.16 The 11-μm BT image for a MODIS granule at 0905 UTC 11 Feb. 2008. The green line indicates the associated CALIPSO/CALIOP track.

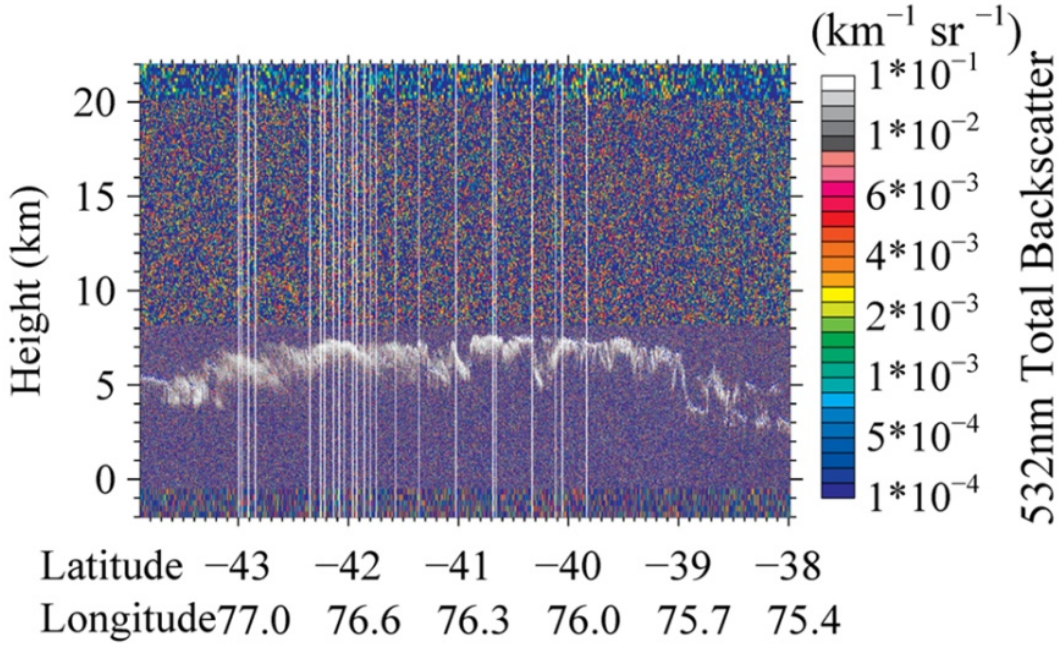

Fig.4.17 The CALIPSO/CALIOP detected 532-nm total backscattering coefficient along the CALIPSO track within the red box region shown in Fig. 4.16. The white lines indicate selected ice cloud pixels.

Meteorological profiles are provided by the Modern Era Retrospective-Analysis for Research and Applications (MERRA, Rienecker et al. 2008) product, which combines both numerical model results and observational data. The 3-hour meteorological profiles of temperature, water vapor and ozone concentrations on 42 pressure levels from the surface to 0.1 hPa with a constant latitude-longitude resolution (1.25°×1.25°) give sufficient information of the background atmosphere. More information about the satellite and meteorological data can be found in Table 4.3. Collocated MODIS, CALIOP, and MERRA data are used to retrieve cloud optical

thickness and effective particle size. Fig. 4.16 shows an example of collocated *Aqua*/MODIS and CALIOP images. The MODIS 11-μm BT image is shown in gray scale and the green line indicates corresponding CALIPSO track. Single layer ice clouds are enclosed by a red rectangle. The vertical structures of cloud layers are revealed by the CALIOP 532-nm total backscatter image shown in Fig. 4.17.

Table 4.3 Ice cloud properties and model parameters employed in the sensitivity studies.

Data Source	Subset	Quantities Selected	Selection Criteria
Aqua/MODIS	MYD02 (L1B)	Reflectivity (Band2, Band7) Brightness Temperature (Band 29, Band31, Band32)	Uncertainty < 1%
	MYD06 (L2)	Cloud Fraction Cloud Phase Surface Temperature	Cloud Fraction > 90% Ice Cloud
CALIPSO/CALIOP	1km Cloud Layer Product (L2)	Cloud Altitude Cloud Phase	Cloud-base height > 5 km Cloud thickness < 2 km Ice Cloud
CALIPSO/IIR	1km Track Product	Surface Emissivity	Emissivity > 0.95
MERRA	3hour Instantaneous Product	Temperature Profile Specific Humidity Profile Ozone Concentration Profile Surface Pressure	-

4.3.2 Retrieval algorithms

Two different RTM-based retrievals are applied to infer cloud optical and microphysical properties. A simple retrieval scheme is used for both of the two methods and is shown in Fig. 4.18. For each MODIS channel, the TOA BT (reflectivity) can be simulated by one of the fast RTMs. An optimal ice cloud τ-D_{eff} pair can be specified by minimizing a cost function, which is defined as:

$$S(\tau, D_{eff}) = \sum_{i=1}^{n} (Obs_i - Sim_i)^2 , \tag{4.6}$$

where i indicates the index of MODIS channel, *Obs* and *Sim* represent the observation and model simulation (BT or reflectivity) in channel i, respectively, and S is the cost function. To minimize uncertainty from the surface, only oceanic ice clouds are included. The CALIPSO/CALIOP Level 2 product is used to eliminate water and mixed-phase clouds. Three IR channels (8.5-, 11, and 12-μm) and two solar reflection channels (0.86- and 2.13-μm) are used to implement the HRTM- and SRTM-based retrieval, respectively. Fig. 4.19 and Fig. 4.20 show the comparisons between satellite observations and model simulations. Using the retrieved τ and D_{eff}, both the SRTM and HRTM simulations perfectly match the MODIS observations.

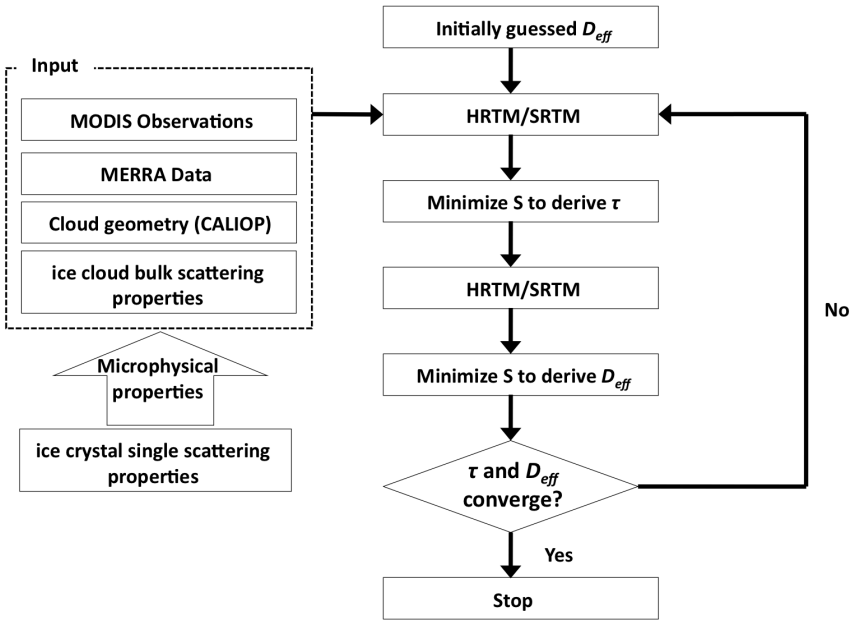

Fig.4.18 Flowchart of the method used to retrieve τ and D_{eff}.

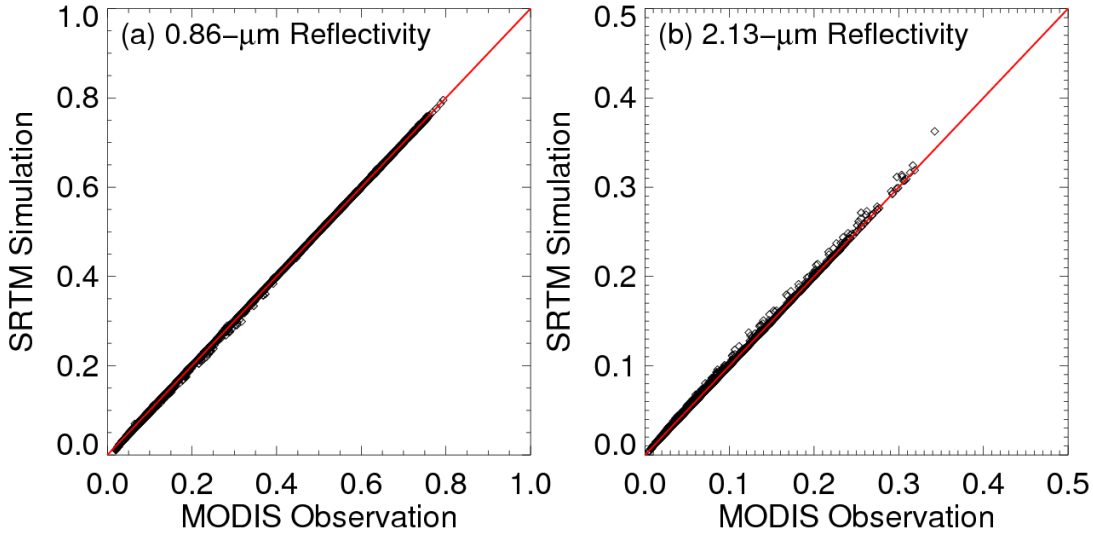

Fig.4.19 Comparisons between the MODIS observations and model simulations using retrieved cloud properties (ice cloud particles are assumed to be smooth solid columns).

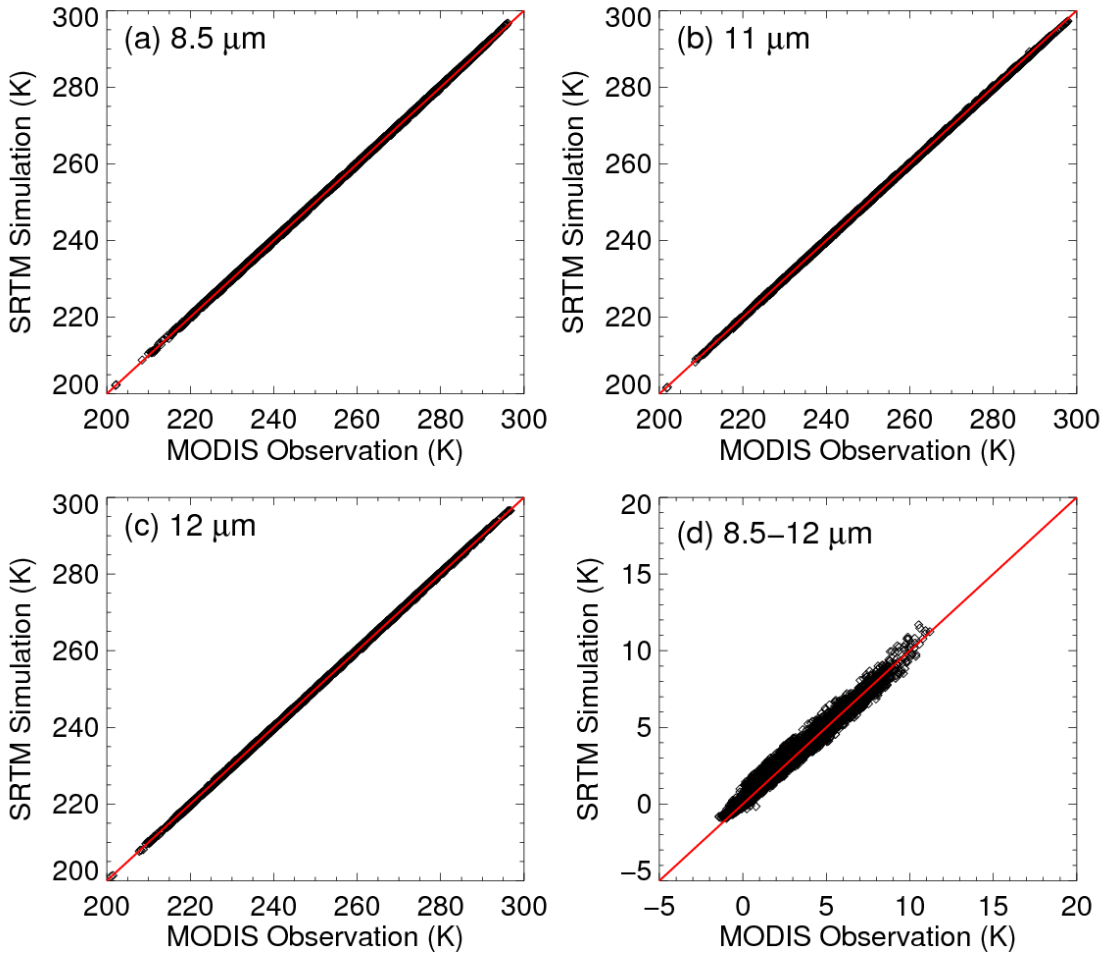

Fig.4.20 Comparisons between the MODIS observed TOA BTs (panels a-c) in Band29 (8.5-μm), Band31 (11-μm), Band32 (12-μm) and BT differences (8.5−12 μm, panel d) and corresponding HRTM simulations in the same channels using retrieved cloud properties (ice cloud particles are assumed to be smooth solid columns).

4.3.3 Comparisons between the SRTM and HRTM based retrievals

Fig. 4.21 and Fig. 4.22 show the comparisons of SRTM-based τ retrievals by assuming different degrees of surface roughness and habits of ice particles. For some

habits, such as the solid column, aggregate of solid columns, and hollow column, the impact from degree of surface roughness on the retrieval of τ is insignificant (i.e., the regression coefficients are close to 1). For other habits, such as droxtal and plate, the retrievals of τ are sensitive to the degree of surface roughness (the regression coefficients are smaller than 0.9). Fig. 4.23 and Fig. 4.24 shows the impacts from degree of ice surface roughness and habit on D_{eff} retrievals, respectively. Similar to the retrieval of τ, the assumption of ice crystal habit significantly impact the retrieval of D_{eff} based on the solar reflectivity channels. Note that in comparison with the impact from ice crystal surface roughness, larger impact from ice crystal habit on both SRTM-based τ and D_{eff} retrievals can be found from Figs. 4.21-4.24.

Different from the SRTM-based retrieval, the HRTM-based retrieval utilizes three IR channels of the MODIS instrument. The sensitivities of both HRTM-based τ and D_{eff} retrievals to pre-assumed cloud microphysical parameterization schemes are shown in Fig. 4.25 and Fig. 4.26. Obviously, the HRTM-based τ retrievals show significant consistency. The impacts on D_{eff} retrievals are slightly higher than τ retrievals, as shown in Fig. 4.27 and Fig. 4.28. However, in comparison with SRTM-based retrieval, the HRTM-based τ and D_{eff} are insensitive to the details of ice crystals, such as the habit and degree of surface roughness.

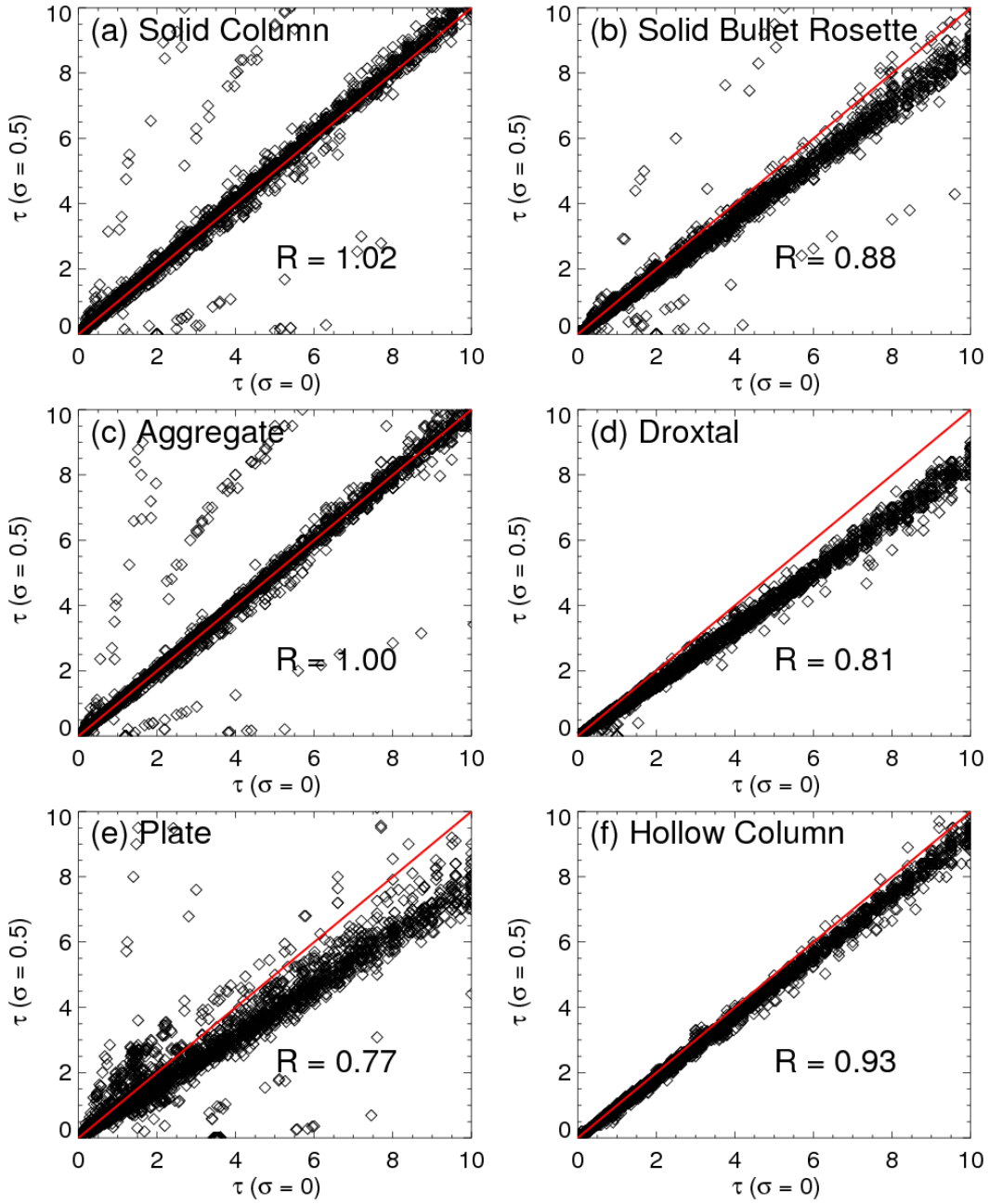

Fig.4.21 Comparisons between the SRTM-based τ retrievals using two degrees of surface roughness (x axis: σ=0; y axis: σ=0.5). Six different habits are shown in the six panels. The number shown in each panel indicates the regression coefficient.

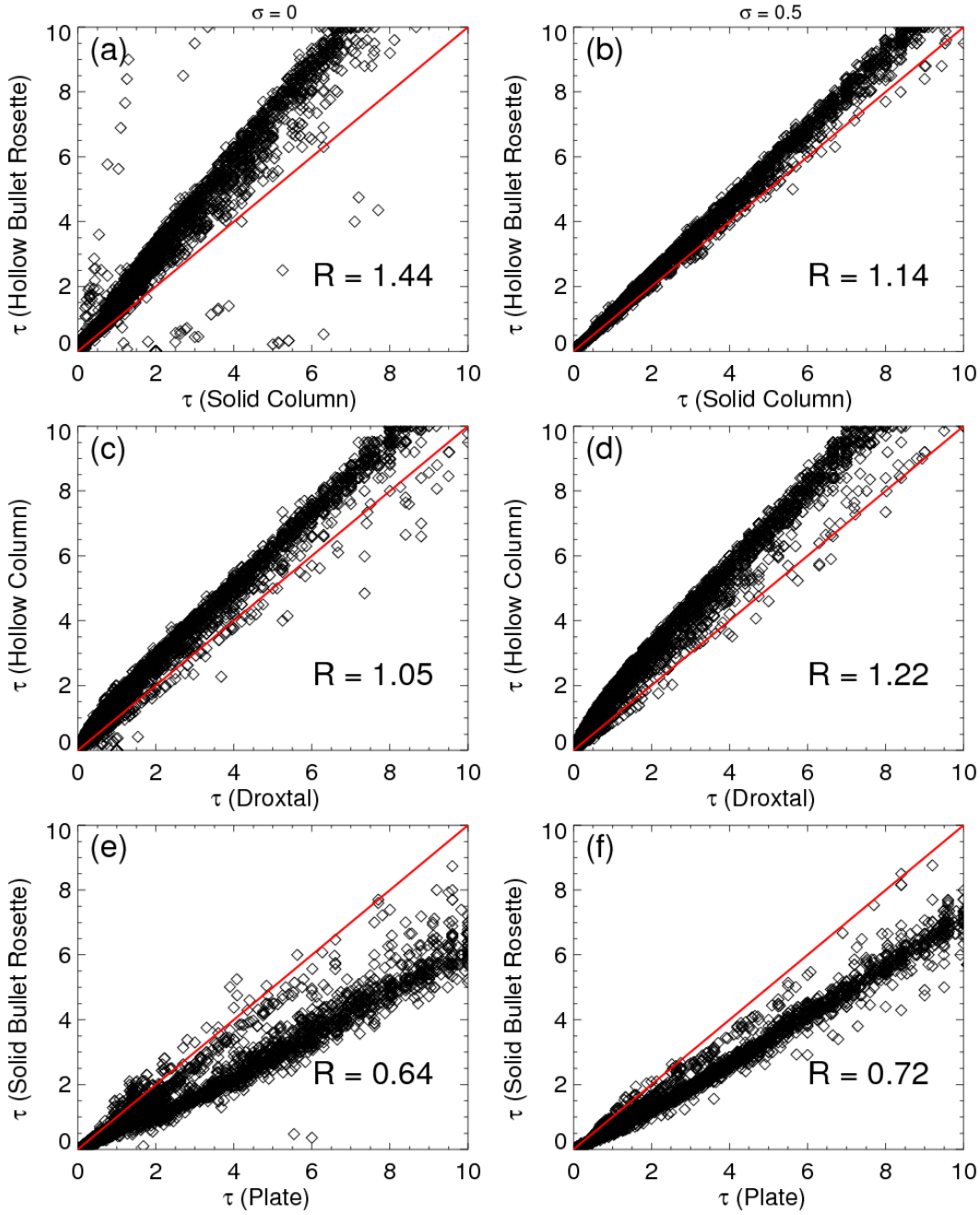

Fig.4.22 Comparisons between the SRTM-based τ retrievals using different habits. Two different degrees of surface roughness are shown in the left (σ=0) and right column (σ=0.5), respectively.

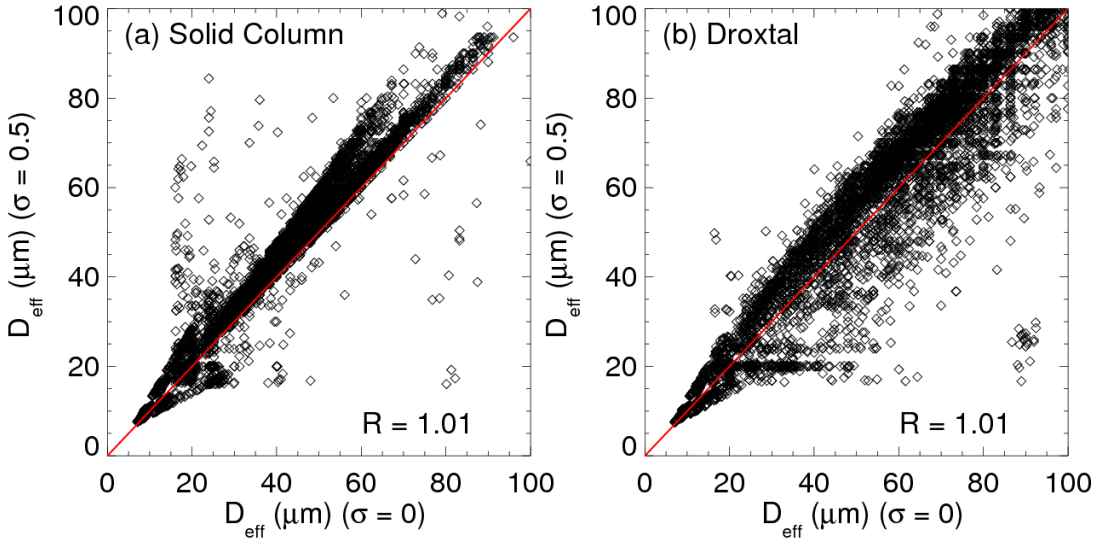

Fig.4.23 Comparisons between the SRTM-based D_{eff} retrievals using two degrees of surface roughness (x axis: σ=0; y axis: σ=0.5) for two different habits.

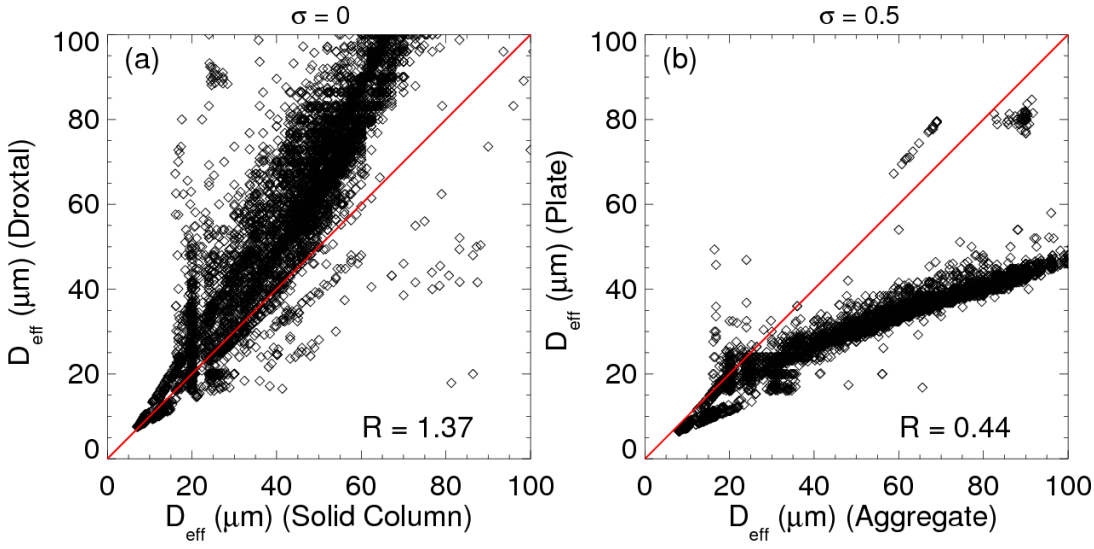

Fig.4.24 Comparisons between the SRTM-based D_{eff} retrievals using different habits. Two different degrees of surface roughness are shown in the left (σ=0) and right column (σ=0.5), respectively.

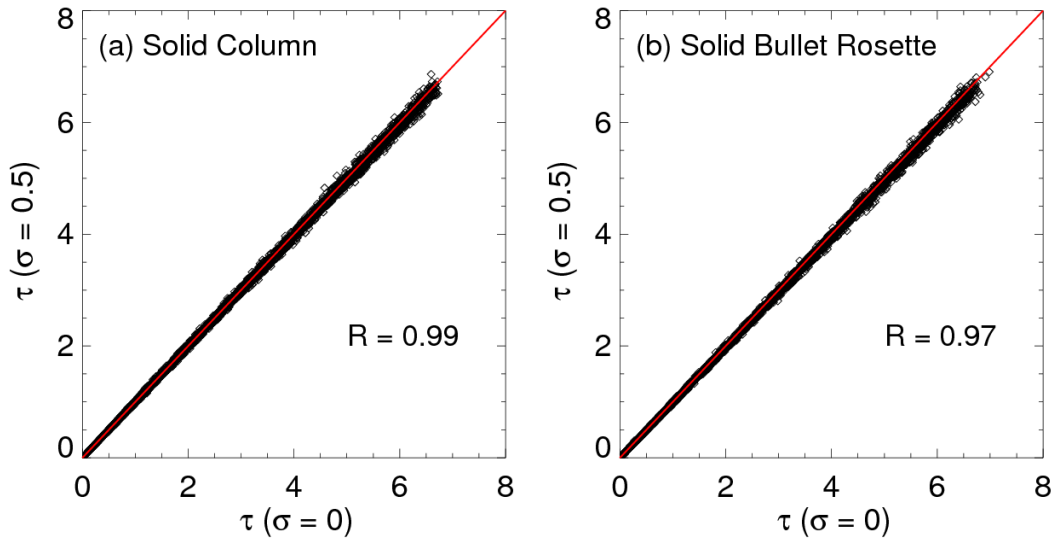

Fig.4.25 Comparisons between the HRTM-based τ retrievals using two degrees of surface roughness (x axis: σ=0; y axis: σ=0.5) for two different habits.

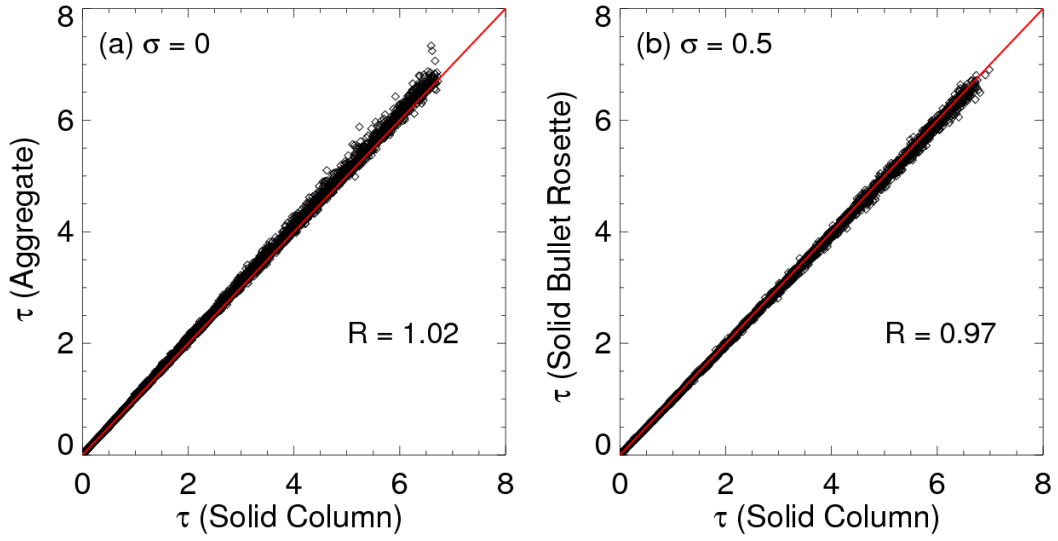

Fig.4.26 Comparisons between the HRTM-based τ retrievals using different habits for two different degrees of surface roughness.

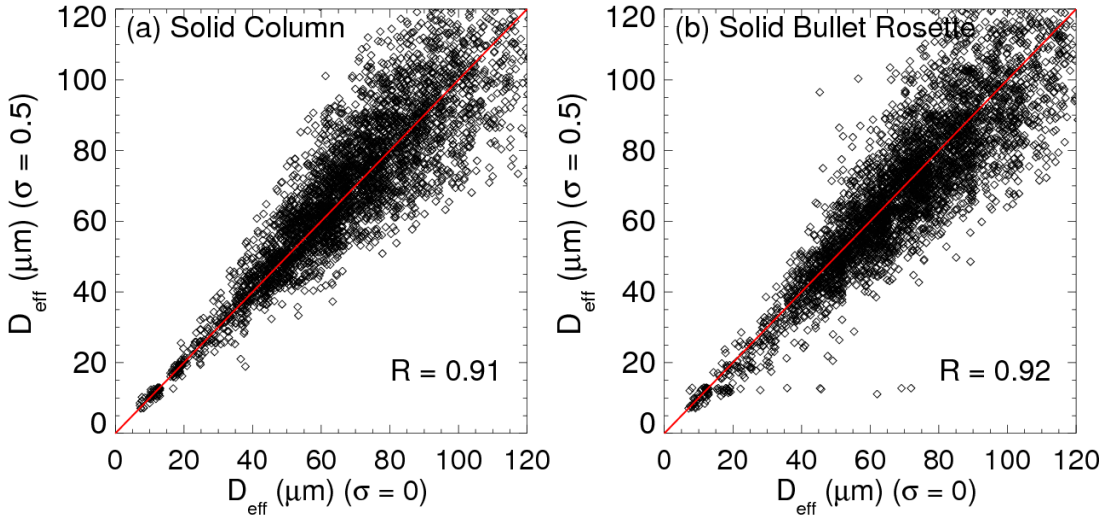

Fig.4.27 Comparisons between the HRTM-based D_{eff} retrievals using two degrees of surface roughness (x axis: σ=0; y axis: σ=0.5) for two different habits.

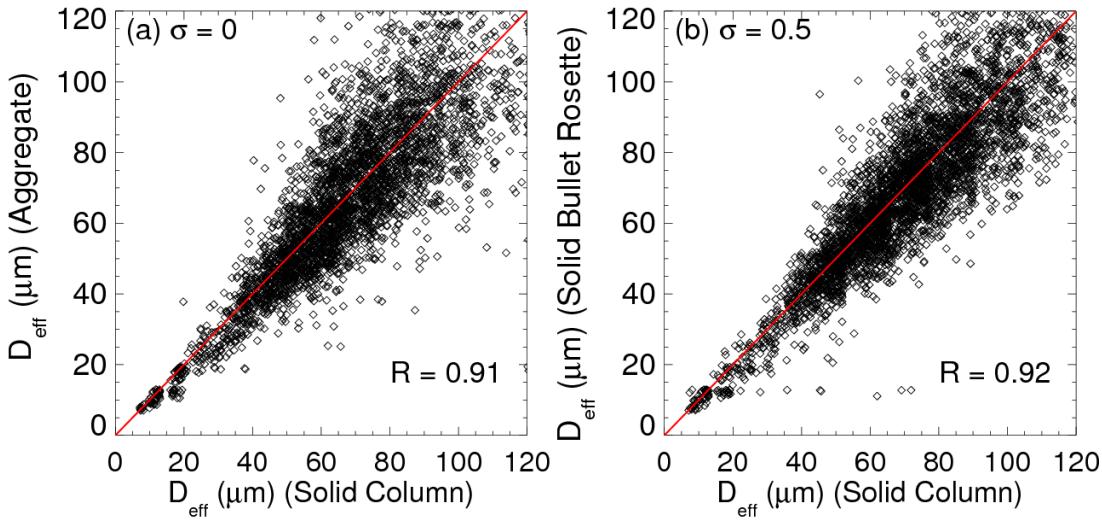

Fig.4.28 Comparisons between the HRTM-based D_{eff} retrievals using different habits for two different degrees of surface roughness.

4.4 Discussion and conclusions

In this chapter, we developed two cloud properties retrieval methods for the two fast RTMs (SRTM and HRTM). The SRTM-based method infers cloud properties by using a combination of two shortwave channels that are sensitive to cloud optical thickness and effective particle size, respectively. The HRTM-based method uses three infrared window channels, which minimize the effects from gas absorption, to deduce cloud properties. The advantages of the two methods become obvious through the elaborate sensitivity studies. In Section 4.3, we also give examples of the two retrievals using observations of the MODIS to visualize the impacts from the pre-assumed cloud properties on the two retrievals.

Generally speaking, retrievals of cloud properties can be influenced by the ambient conditions, such as the surface type, humidity and temperature profiles, and by the internal properties of cloud, such as cloud altitude, and the microphysical features of cloud particles. The two different retrievals utilizing completely different satellite channels show various degrees of sensitivity to both ambient conditions and cloud properties. The SRTM-based method is less sensitive to the ambient profiles and cloud location due to the weak gas absorption in the shortwave spectral region except the 1.38-μm channel. The HRTM-based method also uses window infrared channels in order to minimize the impacts from gas absorption. However, the IR observations (e.g., TOA BTs), have larger sensitivities to cloud location and atmospheric profiles because the cloud layer temperature varies significantly.

As shown in the sensitivity studies, the SRTM-based retrieval is more sensitive to optically thick (or moderately thick, e.g., $\tau > 5$) clouds. For optically thin cirrus clouds, (e.g., $\tau < 1$), the bi-channel reflectivities mesh converges to the values of corresponding surface albedo (assume Lambertian surface), resulting in a relatively large uncertainty of the retrieval. The HRTM-based retrieval, however, performs best if cloud is optically thin (or moderately thin, e.g., $\tau < 3$). Similar to the SRTM-based retrieval, the surface conditions also influence retrievals if cloud is optically thin.

Both retrievals depend on the pre-assumed cloud microphysical parameterization schemes due to the difference between cloud bulk scattering phase functions and other scattering properties (such as single scattering albedo). The habits and degrees of surface roughness of ice crystals impact the finally retrieved τ and D_{eff}. We also show that these impacts are associated with the differences of phase functions at different scattering angles, and the differences of the whole range of phase functions (e.g., asymmetry factor) if multiple scatterings are important. The comparisons between the two RTM-based retrievals show that the use of IR channels leads to consistent τ and D_{eff}, which are approximately independent of the pre-assumed cloud microphysical parameterization schemes. Therefore, the HRTM-based retrievals have intrinsic advantages to get consistent cloud retrievals in current stage that the cloud microphysics is still a major source of uncertainty in both cloud remote sensing applications and climate models.

CHAPTER V

INVESTIGATING THIN CIRRUS CLOUDS USING CALLOCATED AQUA/MODIS AND CALIPSO/CALIOP OBSERVATIONS*

5.1 Background

Optically thin cirrus clouds with visible optical thickness values less than 0.3 are frequently observed in the upper troposphere (Prabhakara et al. 1988, 1993; Winker and Trepte 1998; Dessler and Yang 2003). Because of their widespread spatial distribution and relatively long lifetime (Uthe and Russel 1977), these clouds significantly influence the global energy budget by reflecting solar radiation and emitting longwave radiation at a relatively low temperature (Liou 1986; Rosenfield et al. 1998; McFarquhar et al. 2000). Meanwhile, these clouds keep water vapor from penetrating into stratosphere by homogeneous freezing (Jensen et al. 1996; Khvorostyanov and Sassen 2002; Steinwagner et al. 2010).

Microphysical and optical properties are fundamental parameters for determining the radiative effect of cirrus clouds (Fu 1996). Microphysical properties, such as particle habits (shapes) and size distribution, significantly impact cloud optical properties (Yang et al. 2005; Baum et al. 2010, 2011) and in turn determine the energy balance (Yang et al. 2007). Ice crystal habits and degrees of surface roughness, in particular, impact both

---

* Part of this chapter is reprinted with permission from "A new approach to retrieving cirrus cloud height with a combination of MODIS 1.24- and 1.38-μm channels" by C. Wang, S. Ding, P. Yang, B. A. Baum and A. E. Dessler, 2012. *Geophysical Research Letters*, **39**, L24806, doi:10.1029/2012GL053854, Copyright by John Wiley and Sons.

optical properties and microphysical parameterization of ice cloud in climate model (Mitchell et al. 2008).

Both satellite-based observations (Prabhakara et al. 1988, 1993; Wang et al. 1994, 1996; Mergenthaler et al. 1999) and retrieval techniques (Sassen et al. 2000; Dessler and Yang 2003; Gao et al. 2002, 2004) have been employed to explore properties of thin cirrus clouds. However, very little microphysical information can be obtained from satellite-based observations and retrievals due to the lack of sensitivity. For example, the MODIS operational retrieval method cannot be applied to retrieve both τ and D_{eff} if cloud is optically thin (Ackerman et al. 2008). Therefore, the current knowledge of thin cirrus clouds comes from in situ measurements, which provide more direct approach to observe cloud microphysical properties (Heymsfield and Jahnsen 1974; Heymsfield 1986; Heymsfield and McFarquhar 1996). However, the spatial and temporal limitations (Sassen et al. 2008) prevent the in situ measurements from investigating thin cirrus clouds globally and continually. Meanwhile, uncertainties in published aircraft ice probe measurements arise from ice particle shattering at the inlet to the probes (Heymsfield et al. 2004).

To investigate microphysical properties of optically thin cirrus clouds, we develop a new method to infer the cloud scattering phase functions statistically from one year of satellite observations based on the prior knowledge of cloud optical thickness. This method requires removing the τ-dependent from the satellite reflectivity measurement and then extracting the bulk scattering phase function at a particular scatting angle in the corresponding channel. Current satellite-based operational inference

of τ is based on assumptions of ice crystal microphysical properties. Thus, using these τ would mean that we may not infer anything about the cloud microphysics — trying to do so would only retrieve the microphysics assumed in the retrieval of τ. In Chapter 4, we have demonstrated that the HRTM-based τ retrieval method is independent of the pre-assumed cloud microphysical properties. Therefore, we utilize the HRTM-based method introduced in Section 4.3 to investigate the optical properties of thin cirrus clouds. Observations from two satellite-based instruments, i.e., the MODIS and CALIOP, are primarily used as input in the retrieval method. Based on the retrieved τ, a statistical thin cirrus cloud scattering phase function in the backward directions is derived.

5.2 Methodology

5.2.1 Basic principle

Abundant ice cloud microphysical information is included in the scattering phase matrix, consisting of 4×4 elements that describe the scattering patterns of intensity and polarization. As the first element in the phase matrix, the phase function describes the angular distribution of scattered energy. Several previous studies reported that the phase function, in comparison with other components of phase matrix, shows less sensitivity to ice crystal habits (Hansen 1971b). However, in this study, we still focus on deriving the phase function from satellite observations without polarization for two reasons. First, current satellite instruments that have polarization capabilities, such as the POLDER (Polarization and Directionality of the Earth's Reflectances) wide-field radiometer, do not observe upwelling radiance in the thermal IR regions, and therefore it is difficult to infer the aforementioned independent cloud optical thickness. Second, the instrument,

such as POLDER, has a relatively coarse spatial resolution, resulting in a decreased accuracy in the cloud pixel detection and multi-instrument collocation. For example, the spatial resolution of POLDER Level 1 data is 6 km, whereas the MODIS has 1km or higher spatial resolution.

Investigating the numerically calculated scattering phase functions of ice crystals with various idealized habits and degrees of surface roughness, we find that the phase functions are still sensitive to the habits and surface structures if the incident wavelength is small in comparison with the particle size (e.g., in the shortwave region since the typical particle size of ice crystal is on the order of 10 μm). However, in the IR region, the scattering phase functions of ice crystals become featureless because ice crystals are more absorptive and the a relatively long wavelength leads to the "smoothing out" of sub-wavelength structures on the surface of individual ice crystals. Therefore, a shortwave channel must be used to maintain the sensitivity of the derived phase function to the ice cloud microphysical properties.

The solar reflectance received by the satellite from a single-layer cirrus cloud can be expressed as the summation of two parts (if the Rayleigh scattering is ignored):

$$R_{obs,\lambda} = R_{c,\lambda}(\tau, M, \mu, \phi, -\mu_0, \phi_0) \times T_{two-way,\lambda}(\tau_{g,\lambda}, \mu, -\mu_0) + b_\lambda(\tau, M, \mu, \phi, -\mu_0, \phi_0, r_s), \quad (5.1)$$

where λ indicates the wavelength of a channel, $R_{obs,\lambda}$ is the satellite-observed reflectivity in this channel, $R_{c,\lambda}$ is the cirrus cloud reflectivity, $T_{two\text{-}way,\lambda}$ is the two-way transmissivity including the effect of gas absorption above the cloud layer, b_λ is the surface contributed reflectivity, ϕ is the satellite azimuth angle, μ is the cosine of the satellite viewing zenith angle, ϕ_0 and μ_0 indicate the corresponding geometry of the sun (see Fig. 5.1), τ and M

are the visible optical thickness and microphysical properties of the thin cirrus cloud, $\tau_{g,\lambda}$ is the gas optical thickness, and r_s is surface reflectivity. The two-way transmissivity shown in Eq. (5.1) is defined as:

$$T_{two-way,\lambda}(\tau_{g,\lambda},\mu,-\mu_0)=\exp\left(-\frac{\tau_{g,\lambda}}{\mu}\right)\exp\left(-\frac{\tau_{g,\lambda}}{\mu_0}\right). \tag{5.2}$$

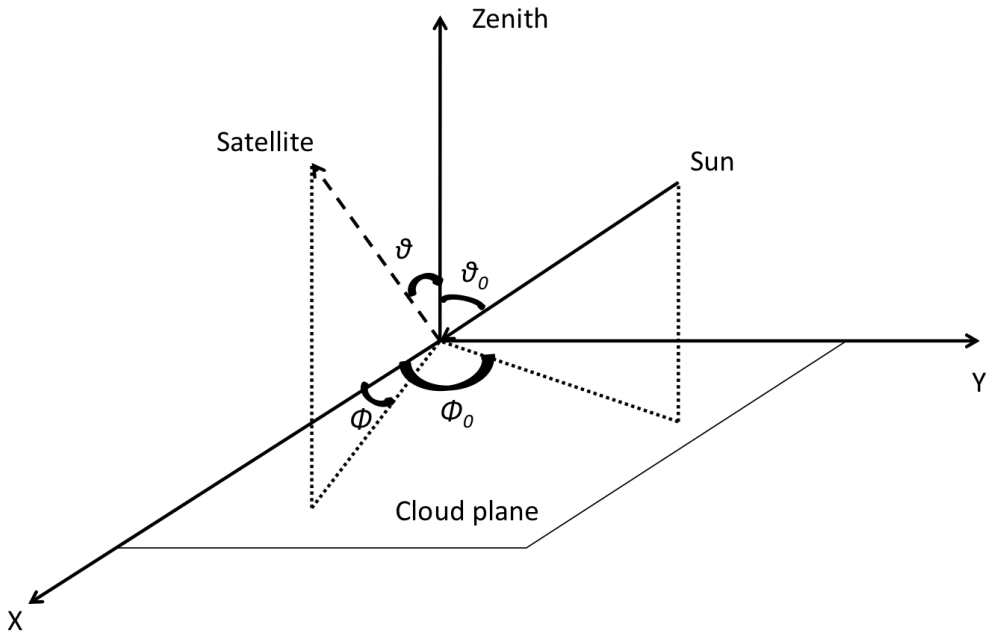

Fig.5.1 Illustrative diagram of the solar-satellite geometry.

If cloud is extremely optically thin (i.e., $\tau << 1$), it is reasonable to derive the scattering phase function at a given scattering angle based on the single scattering approximation (i.e., each photon is scattered no more than once) if μ and μ_0 are not close to 0. In this case, the scattering phase function based on the single scattering approximation can be expressed as follows (Liou 2002):

$$P_{11,\lambda}(\Theta, M) = \frac{4R_{c,\lambda} \times (\mu + \mu_0)}{\omega_{0,\lambda}} \left[1 - \exp(-\tau_\lambda \frac{\mu + \mu_0}{\mu\mu_0}) \right]^{-1}, \tag{5.3}$$

where $P_{11,\lambda}$ is the scattering phase function, $\omega_{0,\lambda}$ is the single scattering albedo, τ_λ is the cloud optical thickness at wavelength λ, Θ is the scattering angle. The relation between cloud optical thickness at a specific wavelength and at a visible wavelength (0.64 μm in this study) is described in Eq. (3.8). If cloud is optically thin (e.g., $\tau \sim 0.1$), the accuracy of single scattering approximation decreases. For this reason, we introduce a multiple-scattering coefficient η_λ (Chiriaco et al. 2006) to give a more general expression of Eq. (5.3):

$$P_{11,\lambda}(\Theta, M) = \frac{4\eta_\lambda R_{c,\lambda} \times (\mu + \mu_0)}{\omega_{0,\lambda}} \left[1 - \exp(-\tau \frac{\mu + \mu_0}{\mu\mu_0}) \right]^{-1}. \tag{5.4}$$

The multiple-scattering coefficient is defined as the ratio of single scattering to total reflectivity:

$$\eta_\lambda = \frac{Rs_{c,\lambda}}{R_{c,\lambda}}, \tag{5.5}$$

where $Rs_{c,\lambda}$ indicates the cloud reflectivity contributed by single-scattering events.

5.2.2 Channel selection

To derive the scattering phase function of ice cloud using Eqs. (5.1~5.5), several approximations must be made for simplification. For example, the Rayleigh scattering, surface reflectivity, and absorption of ice crystals can bring difficulties to our global investigation of thin cirrus clouds.

The MODIS has 36 narrow channels from VIS region to thermal IR region. 20 channels are designed in the shortwave region for various remote sensing applications. To maximize the sensitivity of cloud scattering phase function and minimize the Rayleigh scattering, a shortwave infrared (SWIR) channel can be applied in which ice crystals are weakly absorptive (Warren and Brandt 2008, see Fig. 4.3 and Fig. 5.2) and the Rayleigh scattering can be ignored (Bodhaine et al. 1999). To derive cloud reflectivity from satellite observation using Eq. (5.1), the surface contribution term b_λ needs to be considered. If cloud is optically thick or the surface is non-reflective, this term is small compared with the cloud reflectivity. However, for the optically thin cirrus clouds of interest to this study, b_λ may be comparable to the satellite observed reflectivity and cannot be ignored. To reduce the impact from surface and highlight thin cirrus cloud that frequently occurs in the upper troposphere, a non-window channel (i.e., atmosphere is absorptive) is required. Fig. 5.2 shows the total column transmissivity spectrum of a typical mid-latitude summer atmosphere and the locations of three MODIS SWIR channels. In the MODIS Band5 and Band18, ice crystals are non-absorptive, and the single scattering albedos in the two channels are close to 1. The imaginary part of ice crystal refractive index in the MODIS Band26 is one order of

magnitude higher than in the other two channels (see Fig. 4.3), and therefore ice crystals in the Band26 are weakly absorbing and have a single scattering albedo of 0.99. Absorption abilities of atmosphere in the three MODIS channels are different. Fig. 5.3 (a) shows the cumulative clear-sky optical thickness profiles in the three MODIS channels. For a mid-latitude summer profile, the whole column optical thickness of atmosphere in Band26 is three orders of magnitude higher than in the window channel. Therefore, the satellite observations of a same target in the three channels must have different sensitivities to the cloud altitude and the surface. Recalling Eq. (5.1), the sensitivity of satellite observation to cloud altitude can be expressed as:

$$\frac{dR_{obs,\lambda}}{dz} = R_{c,\lambda} \frac{dT_{two-way,\lambda}}{dz}, \tag{5.6}$$

where z indicates cloud top height (CTH). Note that here we ignore the surface term in Eq. (5.6) since this term is small if atmosphere is strongly absorptive and does not depend on cloud altitude if atmosphere is non-absorptive. An implication of Eq. (5.6) is that the sensitivity of satellite observation is directly proportional to a weighting function, which is defined as the derivative of the clear-sky two-way transmissivity with respect to CTH. Fig. 5.3 (b) shows the corresponding weighting functions in the three channels in typical solar-satellite geometry. The weighting function in the window channel is small in comparison with the absorptive channels and has its maximum values on the surface level, suggesting that the window channel has least sensitivity to CTH and can be significantly impacted by the surface. The 1.38-μm observations have highest sensitivity if CTH is higher than 5 km and they are insensitive to the surface except the

atmosphere is dry. The moderately absorptive channel is sensitive to lower level clouds (e.g., water clouds near the boundary) and can be slightly impacted by the surface. Therefore, we utilize observations in the MODIS Band26 (1.38-μm) to infer the scattering phase function and possible habits and degrees of surface roughness of ice crystals. The phase function equation Eq. (5.4) in this channel can be express as follows:

$$P_{11,1.38}(\Theta,M)=\frac{4\eta_{1.38}R_{obs,1.38}\times(\mu+\mu_0)}{\omega_{0,1.38}\times T_{two-way,1.38}}\left[1-\exp(-\tau\frac{\mu+\mu_0}{\mu\mu_0})\right]^{-1}. \qquad (5.7)$$

The surface term $b_{1.38}$ has been omitted from Eq. (5.1) in this channel.

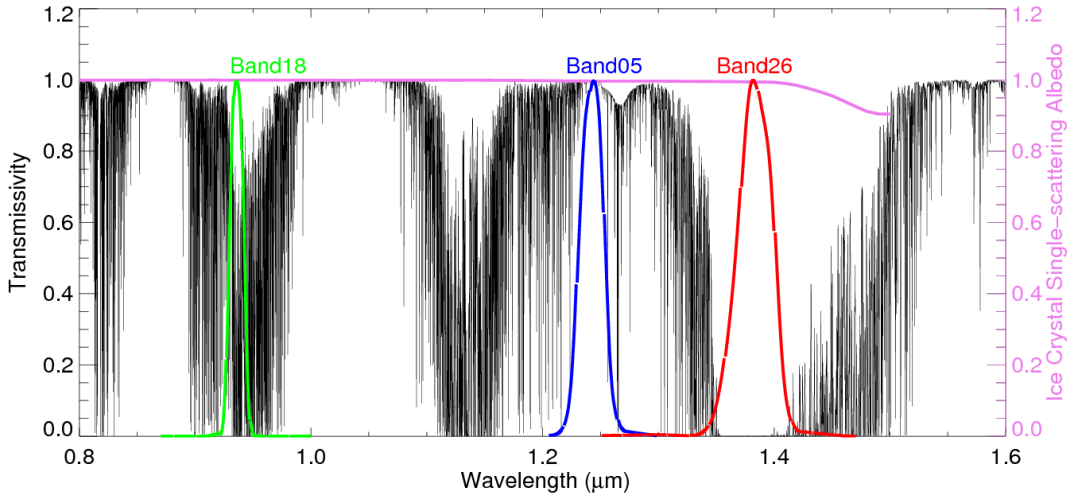

Fig.5.2 The total transmissivity spectrum (black) of a typical mid-latitude summer atmosphere calculated by using the LBLRTM. The violet curve is ice cloud single scattering albedo (D_{eff} = 50 μm, aggregates of roughened solid columns are assumed to be ice particles). The red, blue, and green curves represent the spectral response functions of the MODIS Band26, Band5, and Band18.

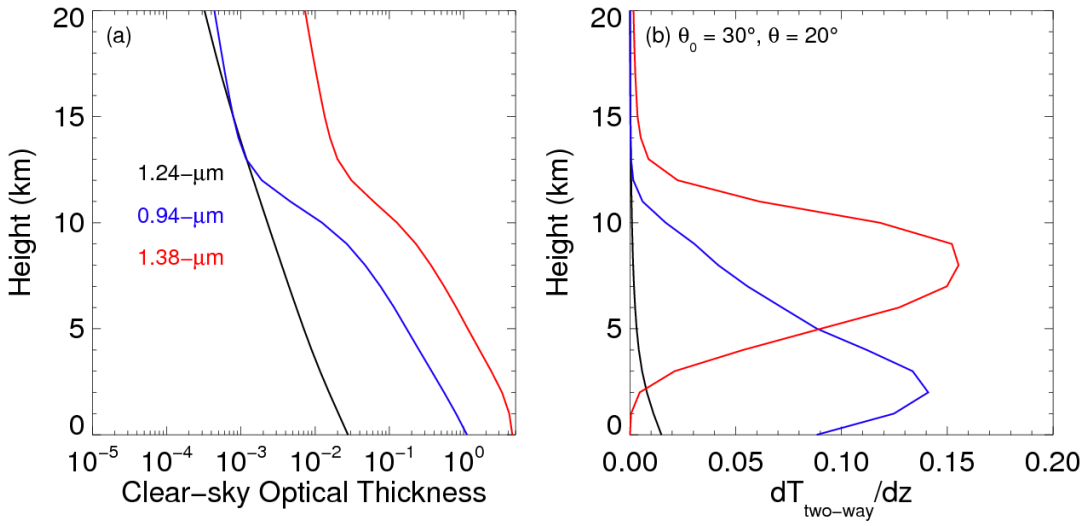

Fig.5.3 (a) The cumulative optical thickness profiles in the three MODIS channels as a function of height. (b) The corresponding weighting functions calculated using a typical geometry.

5.2.3 Cloud optical thickness and clear-sky transmissivity

To deduce cloud microphysical properties or scattering phase functions, we need an independent cloud optical thickness product, which can be inferred by using the three MODIS IR observations in conjunction with the HRTM-based method introduced in Chapter IV. The two-way transmissivity can be accurately calculated by using the LBLRTM with the information of CTH, and atmospheric profiles.

5.2.4 Multiple scattering coefficient

From Eq. (5.5), we can expect the multiple-scattering coefficient η_λ to be a function of the cloud optical and microphysical properties. In this study, we employ two

different bulk ice cloud microphysical models to investigate the sensitivity of η_λ to cloud properties. The first microphysical model is generated using 1117 ice crystal size distributions from in situ measurements of tropical and mid-latitude clouds (e.g., Miloshevich and Heymsfield 1997; Heymsfield et al., 2004). It is used in the current MODIS Collection 5 operational ice cloud retrieval algorithm (hereafter Ice-C5, Baum et al. 2005b). Six different ice crystal habits are used for the Ice-C5 model (droxtal, plate, solid column, hollow column, bullet rosette, and column aggregate), all of which are assumed to be smooth particles except the aggregates of solid columns, which is severely roughened. The habit fractions of the six habits are functions of the maximum dimension of ice crystals (see Fig. 5.4). The second microphysical model considers a generalized habit mixture (GHM) of ice crystals in which all the particles have severely roughened surfaces (hereafter Ice-GHM, Baum et al. 2011). In addition to the six habits used in the Ice-C5 model, three new habits (hollow bullet rosettes, small and large aggregate of plates) are included in the Ice-GHM model (see Fig. 6a in Baum et al. 2011). Single scattering properties of the ice crystals are introduced by Yang et al. (2013).

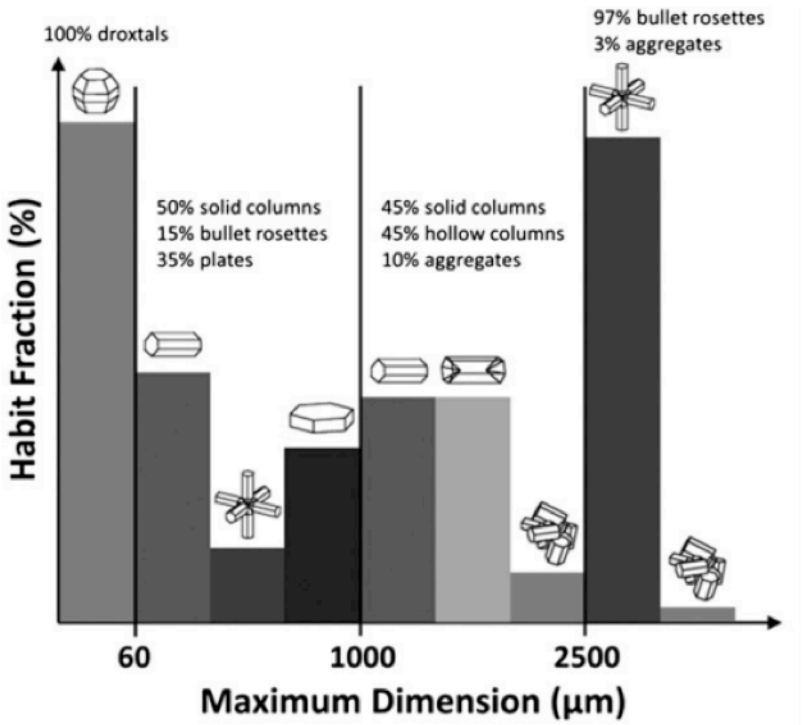

Fig.5.4 Habit distribution of the Ice-C5 microphysical parameterization scheme (from Yang et al. 2013).

$\eta_{1.38}$ values based on Ice-C5 and Ice-GHM are calculated by following Eq. (5.5) with the rigorous DISORT model and single scattering approximation. Fig. 5.5 (a) shows the multiple-scattering coefficient $\eta_{\text{Ice-C5},1.38}$ as a function of effective particle size. For a given scattering angle, $\eta_{\text{Ice-C5},1.38}$ is generally determined by cloud optical thickness, rather than the effective particle size. Fig. 5.5 (b) shows the $\eta_{\text{ICE-GHM}}$-to-$\eta_{\text{Ice-C5}}$ ratio as a function of τ and D_{eff}. The ratio is close to one, suggesting that η is insensitive to cloud

microphysical properties. Therefore, we use the DISORT to generate a lookup table of $\eta_{1.38}$ as function of cloud optical thickness and solar-satellite geometry.

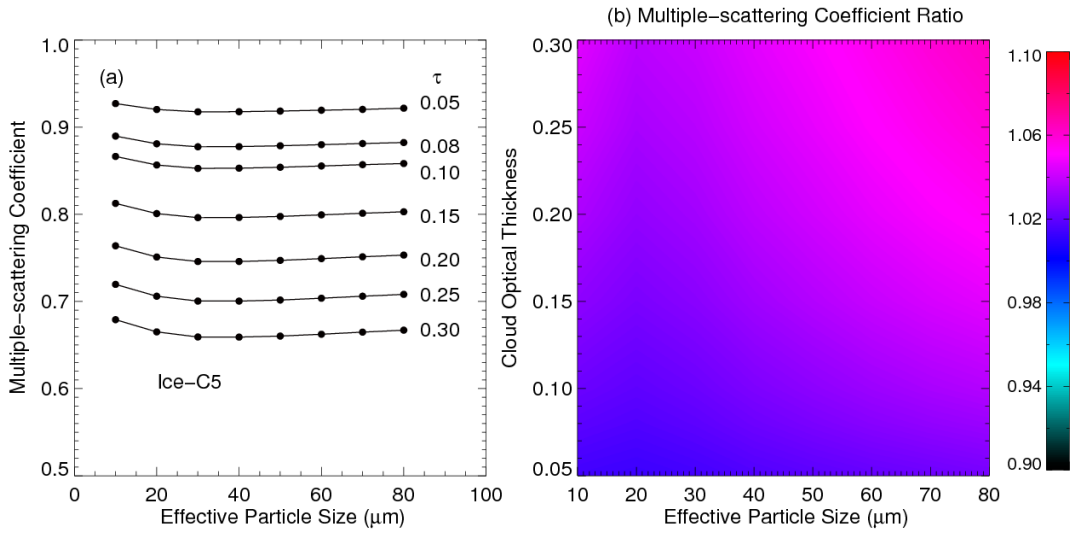

Fig.5.5 (a) The multiple-scattering coefficient as a function of effective particle size calculated by using the Ice-C5 microphysical parameterization scheme. (b) The ratio of multiple-scattering coefficients using the Ice-GHM and Ice-C5 parameterization schemes.

5.3 Data

To investigate the scattering phase functions of optically thin cirrus clouds globally, more than 10 million ice cloud measurements are selected from one year (2008) of collocated *Aqua*/MODIS and CALIPSO/CALIOP products. Specifically, the

CALIOP Level-2 1km cloud layer product is employed to specify the cloud layer boundaries. The MODIS Level-2 cloud product, which has a much wider viewing zenith angle range, also provides retrieved CTH information. However, in this study, the collocated MODIS and CALIOP data are used even if only a narrow range of viewing zenith angles is available, leading to a narrow range of scattering angles. The CO_2 slicing algorithm (Smith and Platt 1978; Menzel et al. 1983; Wylie and Menzel 1999) is used to retrieve CTH for MODIS. However, Holz et al. (2008) found that MODIS Collection 5 mean cloud top heights were frequently lower than collocated Cloud-Aerosol Lidar with Orthogonal Polarization (CALIOP) measurements. By investigating the spatial distribution of the CTH differences, Holz et al. (2008) found that the biggest differences occurred in the Inter-Tropical Convergence Zone (ITCZ), where thin cirrus clouds frequently occur due to deep convections (Jensen et al. 1996; Rosenfield et al. 1998). Fig. 5.6 shows the scaled frequency of ΔCTH (CALIOP−MODIS C5) as a function of CALIOP cloud optical thickness (τ_{CALIOP}). The scaling factor is the highest value of the frequency in each τ_{CALIOP} bin; the CALIOP–detected multi-layered cloud pixels are removed from consideration.

For most of the cases, CALIOP and MODIS CTH values are consistent with each other, with ΔCTH values limiting to ±1km. However, if τ_{CALIOP} are less than 0.7, the absolute values of ΔCTH clearly increase, suggesting that, in comparison with observations of CALIOP, the MODIS CTH is more variable at these low optical thickness values, and may even fail to retrieve a cloud height for some cases as evidenced by the maximum ΔCTH frequency bin in the upper left corner of Fig. 5.6. The

relatively large ΔCTH indicates that, if a cloud is optically thin, the application of the CO_2 slicing algorithm becomes problematic due to the relatively weak cloud signal-to-noise ratio in the thermal infrared CO_2 absorption channels (Menzel et al. 2008). The surface and lower atmosphere contribute more emission to the satellite-received signal and, therefore, increase the retrieval uncertainty.

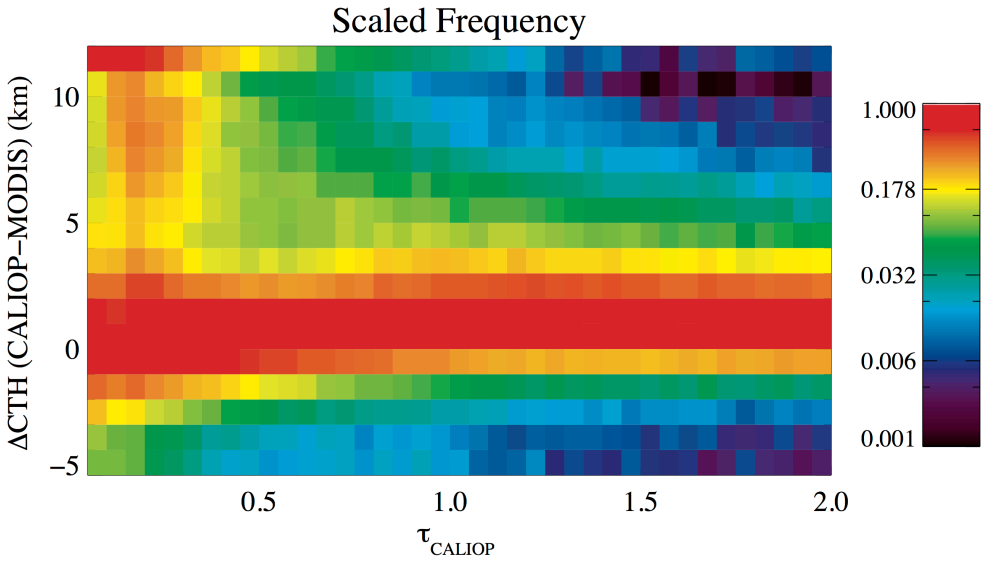

Fig.5.6 Frequency of ΔCTH (CALIOP−MODIS) as a function of τ_{CALIOP}. The frequency is scaled by dividing the largest frequency in each τ_{CALIOP} bin. Data are from collocated MODIS and CALIOP measurements made in August 2006.

The MODIS data are filtered based on the CALIOP product for single-layered cirrus clouds with cloud base altitudes higher than 8 km. The MODIS observations in 1.38-, 8.5-, 11, and 12-μm channels are extracted to retrieve the cloud scattering phase function, optical thickness, and effective particle size. The temperature, humidity and ozone concentration profiles are extracted from the MERRA reanalysis data (Rienecker et al. 2008).

5.4 Results

5.4.1 Overview

Figs. 5.7 and 5.8 show the geographical distributions of the collocated cloud data for daytime and nighttime, respectively. No matter daytime or nighttime, the frequencies of all kinds of clouds (i.e., including ice and water clouds) and ice clouds have similar patterns globally. In high-latitude regions, water clouds dominate but in tropics, more than half of the cloudy samples are ice clouds, which can be found by investigating the differences between the frequencies of all kinds of clouds (i.e., including water, ice, and mixed phase clouds) and ice clouds only samples (see the first and second panels in Figs. 5.7 and 5.8). Panel (c) in each of the two figures shows the frequency of thin cirrus cloud with the CALIOP retrieved cloud optical thickness between 0.03 and 0.3 and CTH higher than 8 km. Panel (d) shows the frequency of subvisible cirrus clouds with τ_{CALIOP} less than 0.03. Most of the optically thin cirrus clouds ($\tau_{CALIOP} < 0.3$) occur in the tropics, especially the western Pacific, Africa, and South America and its west coast, which is consistent with previous studies (Sassen et al. 2008). In comparison with the frequencies of subvisible cirrus clouds during the daytime and nighttime, it is found that

the nighttime frequency is systematically higher than the daytime. During the daytime, reflected solar radiation decreases the signal-to-noise ratio (SNR) of the CALIOP observation. Consequently, the CALIOP cloud detection algorithm needs to increase a threshold of cloud-to-gas molecule scattering ratio to eliminate false cloud signals. However, the increase of the threshold value also eliminates some real cloud signals, especially if cloud is optically thin (Vaughan et al. 2009; Chepfer et al. 2013).

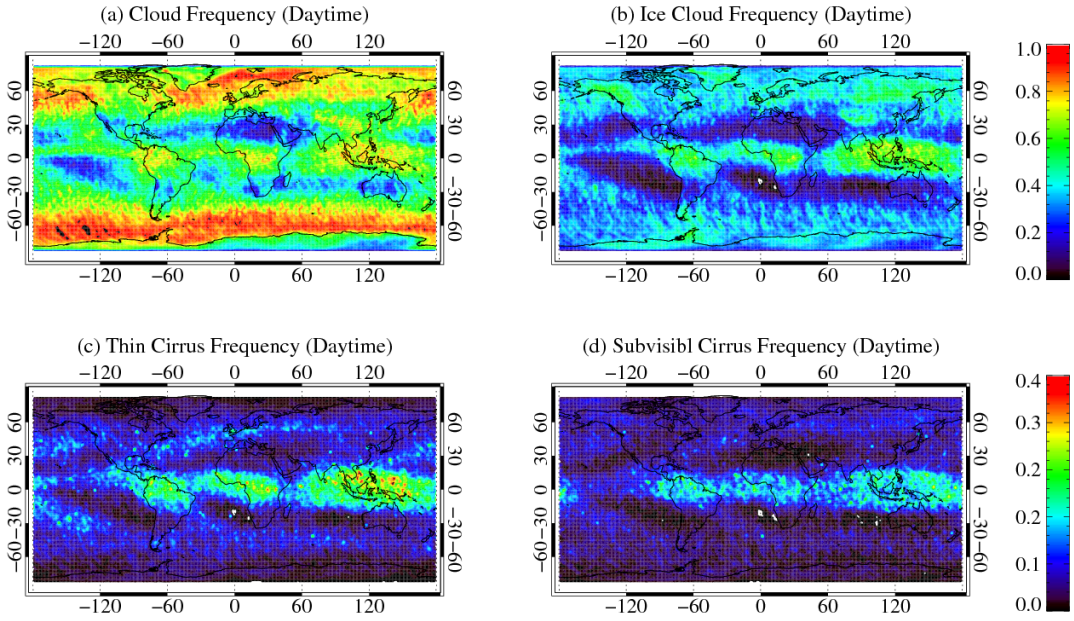

Fig.5.7 Daytime frequencies of (a) cloud, (b) ice cloud, (c) thin cirrus cloud (i.e., 0.03 < τ_{CALIOP} < 0.3, CTH > 8 km), and (d) subvisible cirrus (τ_{CALIOP} < 0.03, CTH > 8 km) during 2008.

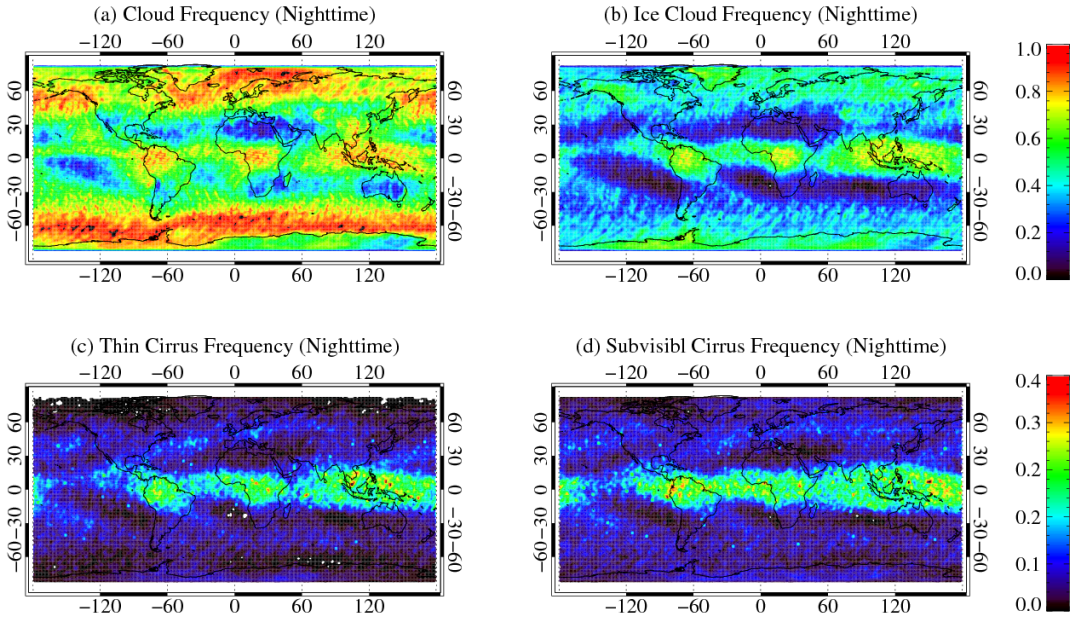

Fig.5.8 Nighttime frequencies of (a) cloud, (b) ice cloud, (c) thin cirrus cloud (i.e., 0.03 < τ_{CALIOP} < 0.3, CTH > 8 km), and (d) subvisible cirrus (τ_{CALIOP} < 0.03, CTH > 8 km) during 2008.

The scattering angle frequencies of global, low-, mid-, and high-latitude thin cirrus clouds are shown in black, red, green, and blue in Fig. 5.9. More than 80% of the data have Θ larger than 120° because solar zenith angles are relatively small (collected pixels are frequently located in the tropical region) and the collocations of the CALIOP and MODIS observations occur over a small viewing zenith angle of the MODIS instrument (always smaller than 20°). High-latitude samples dominate scattering angles that are smaller than 110°.

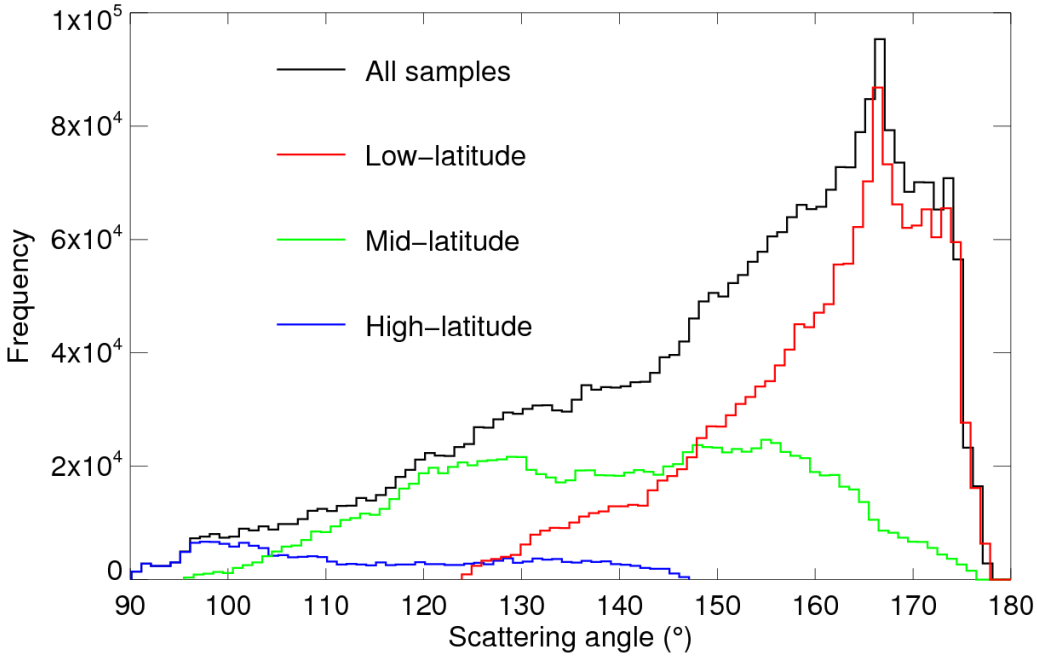

Fig.5.9 Frequencies of scattering angles for global, low- (30°S to 30°N), mid- (30°N/S to 60°N/S), and high-latitude (60°N/S to 90°N/S) thin cirrus samples.

5.4.2 Optical property

Ice cloud optical thicknesses are retrieved using the IR-based method and assuming the Ice-C5 cloud microphysical parameterization scheme. Fig. 5.10 shows the normalized (red bar) and cumulative (black line) frequency of the cirrus τ from the IR-retrieval (but adjusted to 0.64 μm using Eq. 3.8). It shows that the IR-based cloud optical thickness values for all ice cloud samples (more than 10 millions) span a wide range from 0 to 8. About 2 millions samples (20%) are thin cirrus clouds with τ less than 0.3.

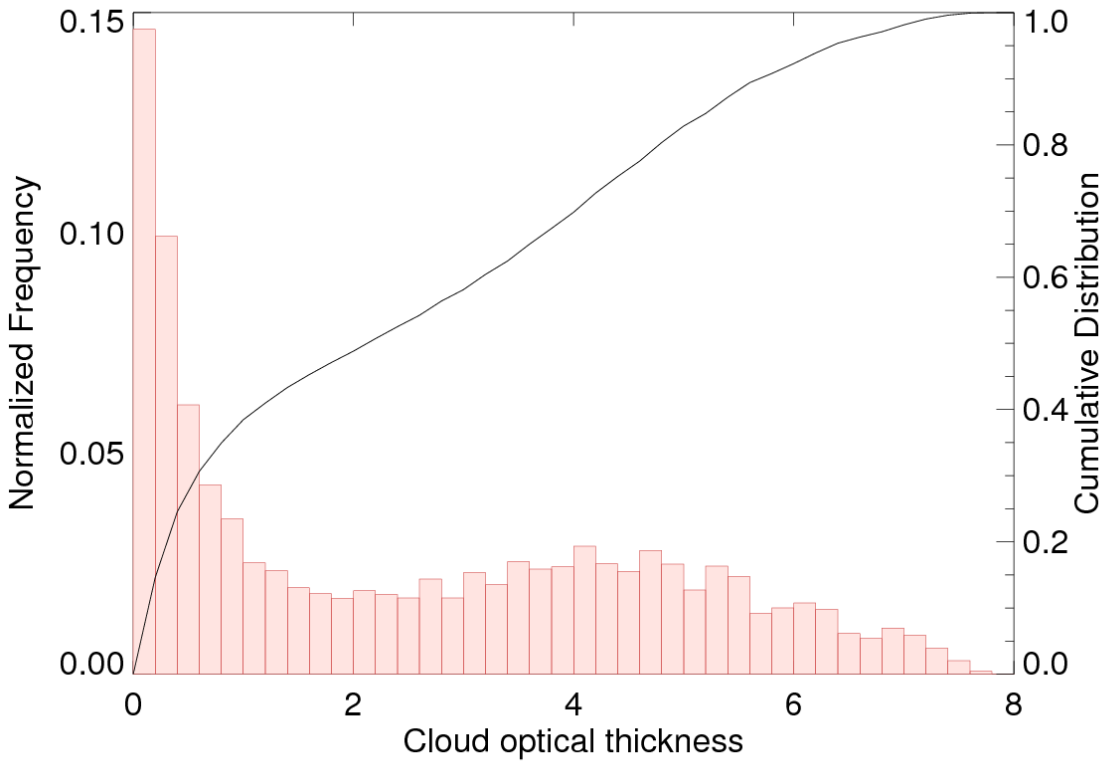

Fig.5.10 Normalized frequency (red bar) and cumulative distribution (black curve) of retrieved ice cloud τ (at visible wavelength) using IR-based method.

The two panels in Fig. 5.11 show the global annual averaged cloud optical thickness distributions for all ice cloud samples and thin cirrus only samples, respectively. The averaged τ geographical distribution of ice cloud samples has similar pattern with the corresponding frequency distribution, that is, high frequency regions coincide with the large τ regions approximately. However, for optically thin cirrus clouds (panel b in Fig. 5.11), the geographical distribution of τ shows little spatial

variation and has little relation with the frequency of occurrence. This feature can also be obtained from the zonal mean frequencies and zonal mean optical thicknesses of ice cloud and thin cirrus cloud samples, which are shown in Fig. 5.12. The optical thicknesses of thin cirrus clouds over land and ocean are quite similar. More details about the statistics of cloud optical thickness are listed in Table. 5.1.

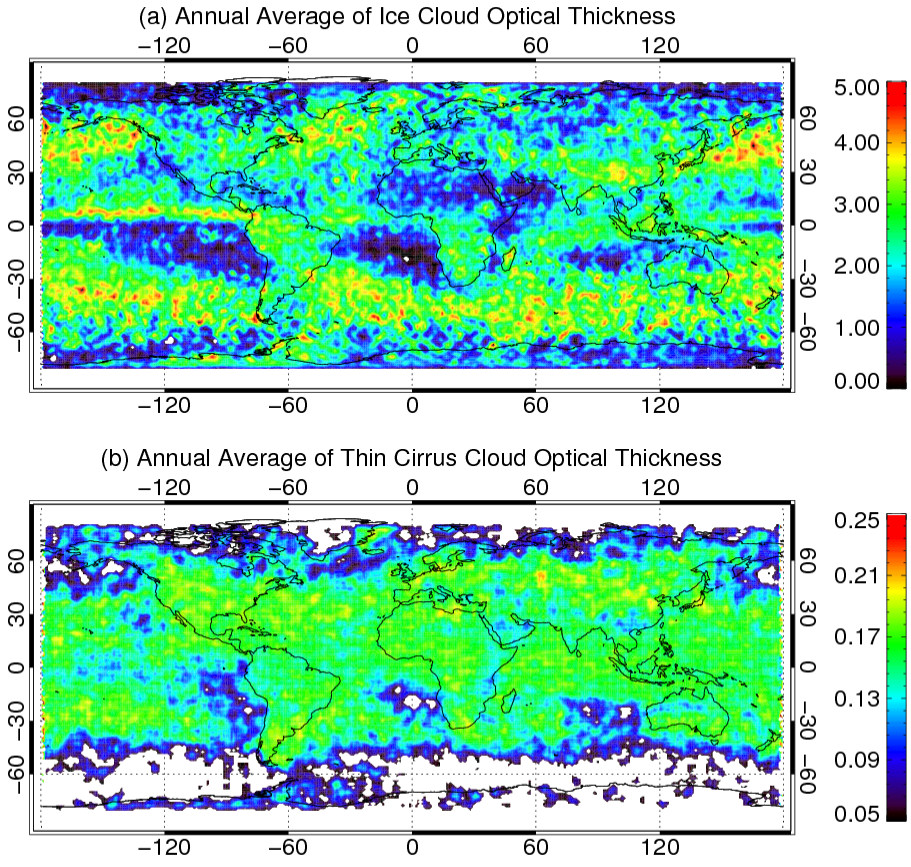

Fig.5.11 Annual averaged IR-based τ distribution patterns of (a) ice clouds, and (b) optically thin cirrus clouds ($\tau < 0.3$).

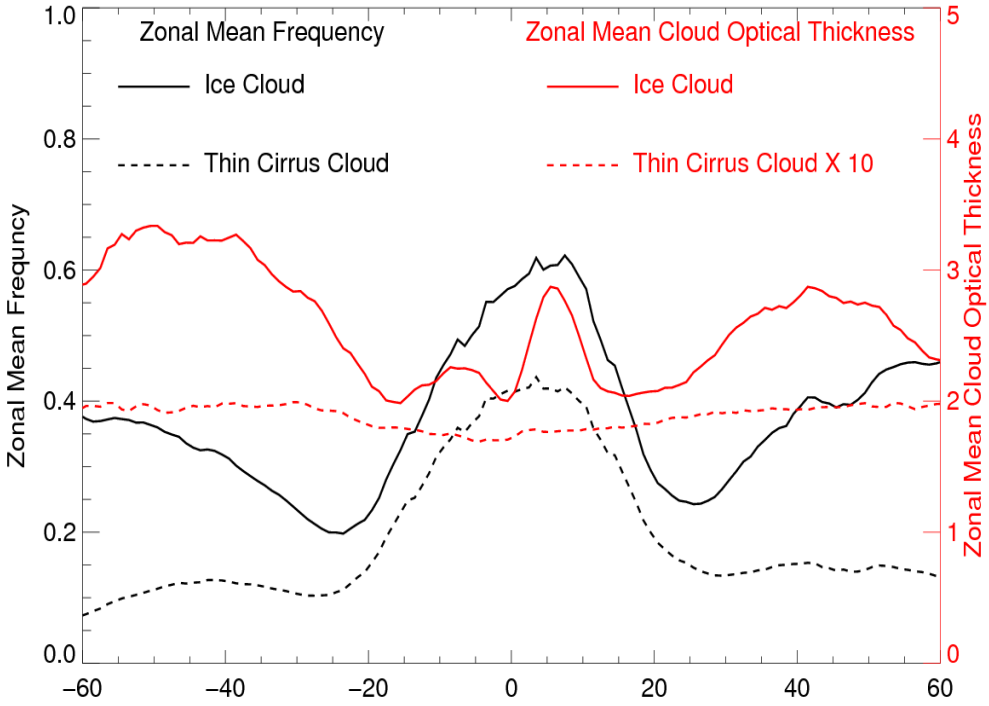

Fig.5.12 Zonal mean frequencies of ice cloud and thin cirrus cloud samples (black curves), and zonal mean cloud optical thickness of ice cloud and thin cirrus cloud samples (red curves, zonal mean optical thickness of thin cirrus cloud is amplified by a factor of 10).

5.4.3 Microphysical properties

Fig. 5.13a and 5.13b show the scattering plots of inferred thin cirrus cloud phase functions over land and ocean, respectively. The mean values of terrestrial thin cirrus clouds and corresponding standard deviations are shown with squares (circles for samples over ocean) and vertical bars, respectively. In comparison with the averaged phase function over ocean, the phase function over land exhibits several oscillations. The larger standard deviations over land may partially result from less cirrus samples are collected over land and/or relatively large uncertainties of land surface temperature and emissivity decrease the quality of τ retrieval (Wang et al. 2013a). As mentioned in Section 5.2, the 1.38-μm reflectivity observations may include the surface information if column water vapor concentration is low (e.g., high-latitude region). Therefore, we plot the inferred scattering phase function again by eliminating the thin cirrus samples with latitude higher than (45°N or 45°S), as shown in Fig. 5.14. It shows that the samples with low scattering angles ($\Theta < 110°$) are generally removed. However, there is no obvious change in both of the averaged phase functions and the corresponding standard deviations.

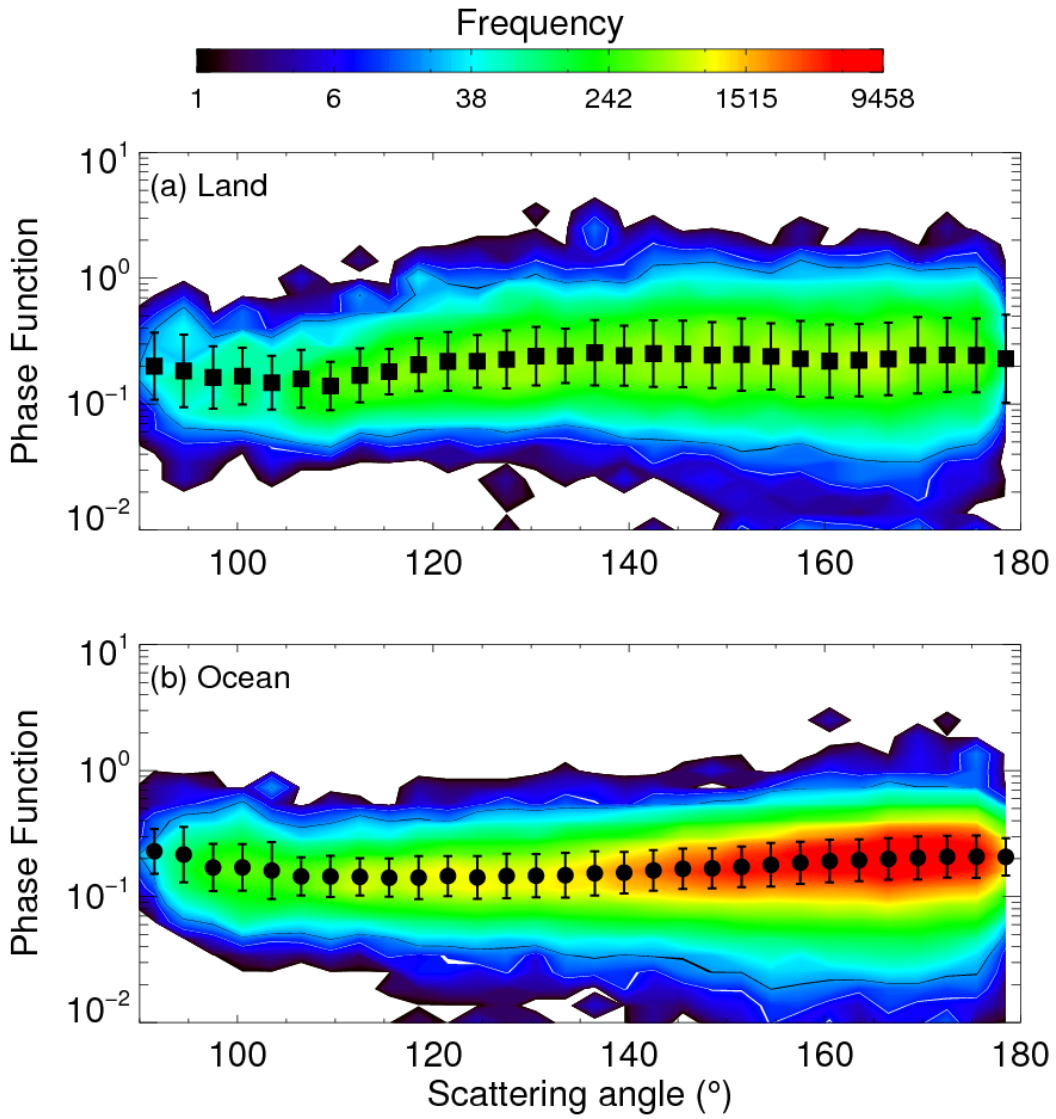

Fig.5.13 Scattering plot of inferred thin cirrus cloud phase function over land (a) and over ocean (b). Black squares and circles represent the corresponding averaged phase functions. Error bars indicate corresponding standard deviations.

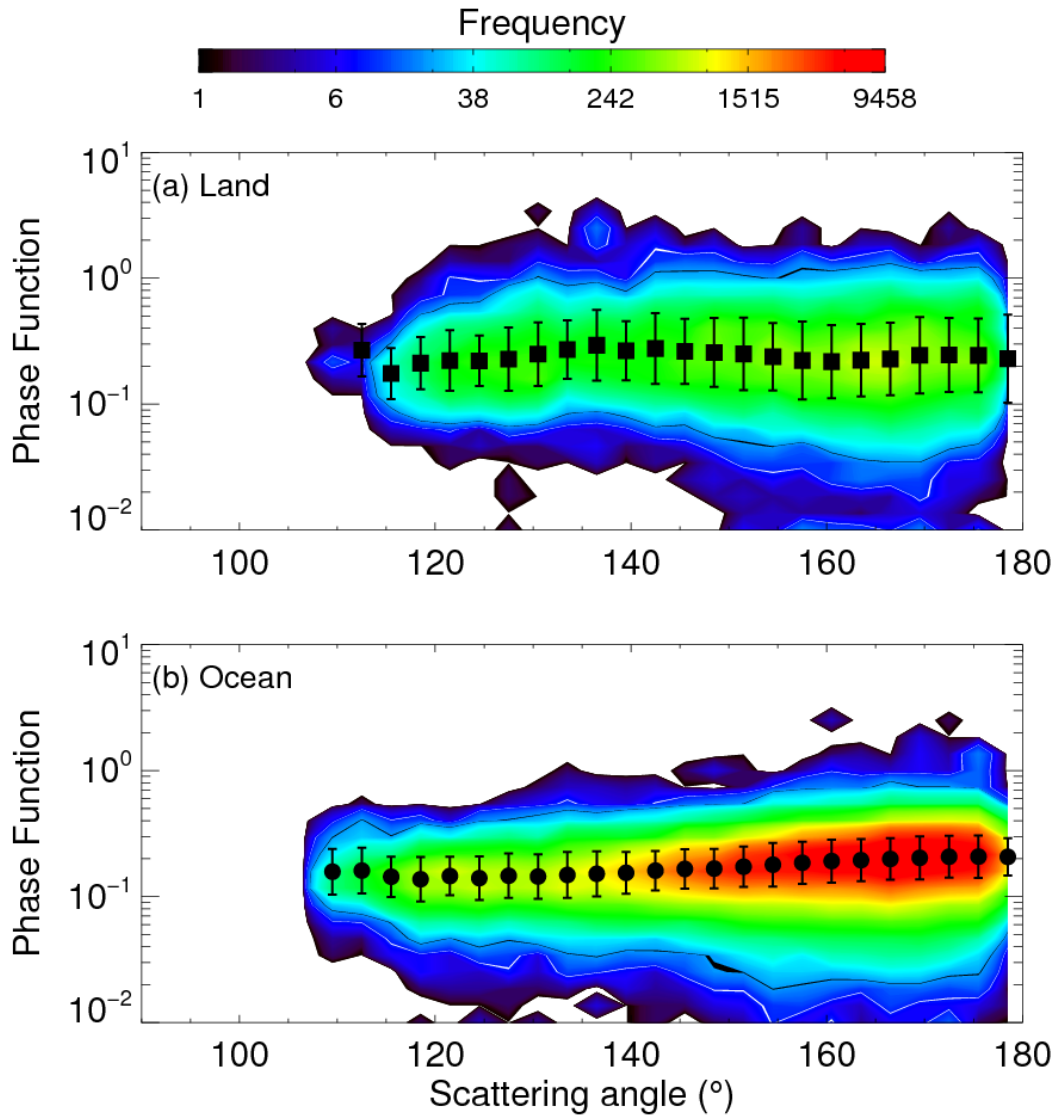

Fig.5.14 Same as Fig.5.13, but samples in low-latitude region (45°S ~ 45°N) are plotted.

To better represent the microphysical properties of thin cirrus clouds with idealized ice crystal models (e.g., the 9 habits mentioned in Chapter IV), we employ the Monte Carlo method that uses the theoretically calculated phase functions of randomly

oriented ice crystals to fit the averaged scattering phase functions inferred from observations. Panels (a) to (d) in Fig. 5.15 show the comparisons between the inferred scattering phase functions of oceanic thin cirrus clouds and theoretical phase functions of different gamma distributed ice crystals. In comparison with the phase functions of smooth particles, the phase functions of roughened solid columns and column aggregates seem to be most similar to the inferred oceanic cirrus phase function, suggesting that the phase function comparisons reveal that roughened solid columns and column aggregates may dominate thin cirrus clouds over ocean. Baum et al. (2011) show that in synoptic cirrus clouds, ice particles initiated by homogeneous nucleation are likely to grow as poly-crystals. Furthermore, a portion of thin cirrus clouds in the upper troposphere, particularly in tropics with ambient temperature lower than -55°C, (Sassen et al. 2008; Baum et al. 2011) may include droxtals. As shown in panels (c) and (d), only scattering phase functions of droxtals exhibit a gradual increment in side through backward directions. Panel (e) in Fig. 5.15 shows comparisons between inferred oceanic phase function and the phase functions generated with two habit mixtures (i.e., Ice-C5 and Ice-GHM). Similarly, the assumption of smooth particles in the Ice-C5 model leads to relatively strong phase function oscillations and strong backward scattering. The phase function of Ice-GHM captures the major features of the inferred one, suggesting that it is possible that roughened particles are dominant thin cirrus clouds. A best-fitted scattering function is shown in Panel (f). Obviously, the artificially generated scattering phase function almost perfectly matches the inferred one. Therefore, we suggest using 55%

severely roughened solid columns, 35% severely roughened droxtals, and 10% smooth aggregates to represent the ice crystals within oceanic thin cirrus clouds.

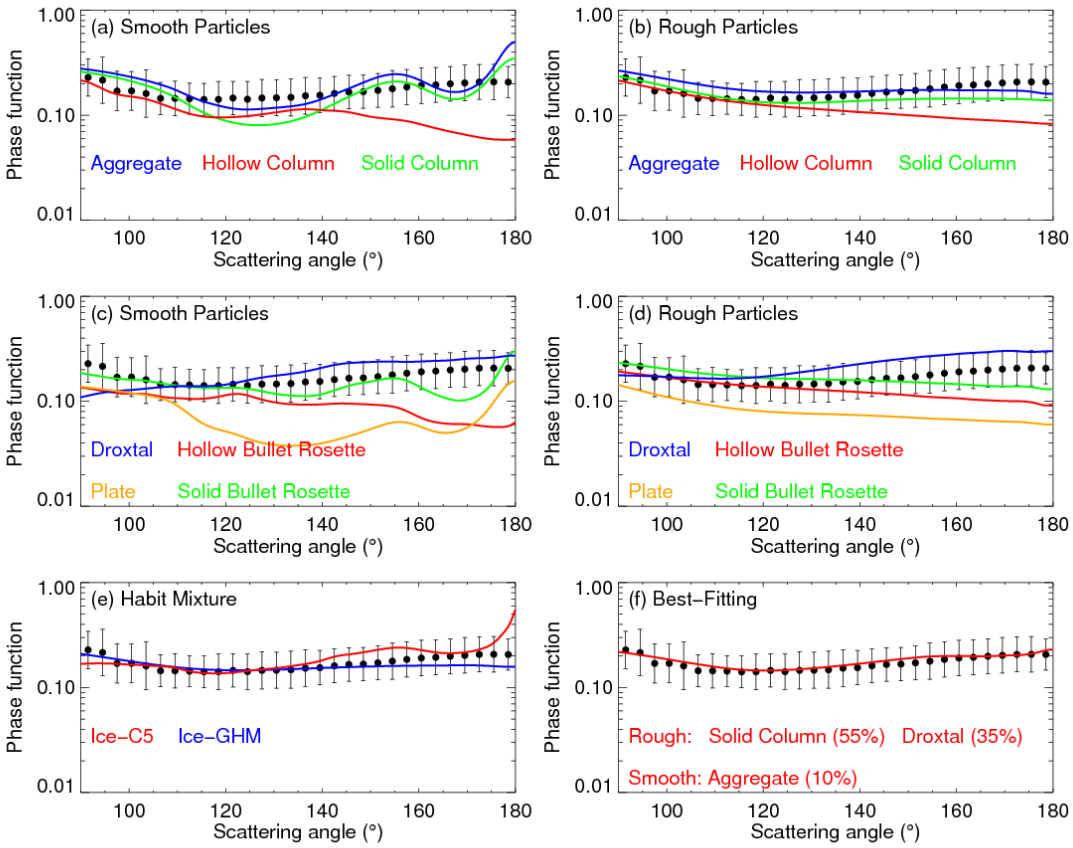

Fig.5.15 Comparisons between inferred scattering phase function of oceanic thin cirrus clouds (black dots as shown in Fig. 5.13b) and scattering phase functions of ice crystals with ideal habits or mixtures of habits.

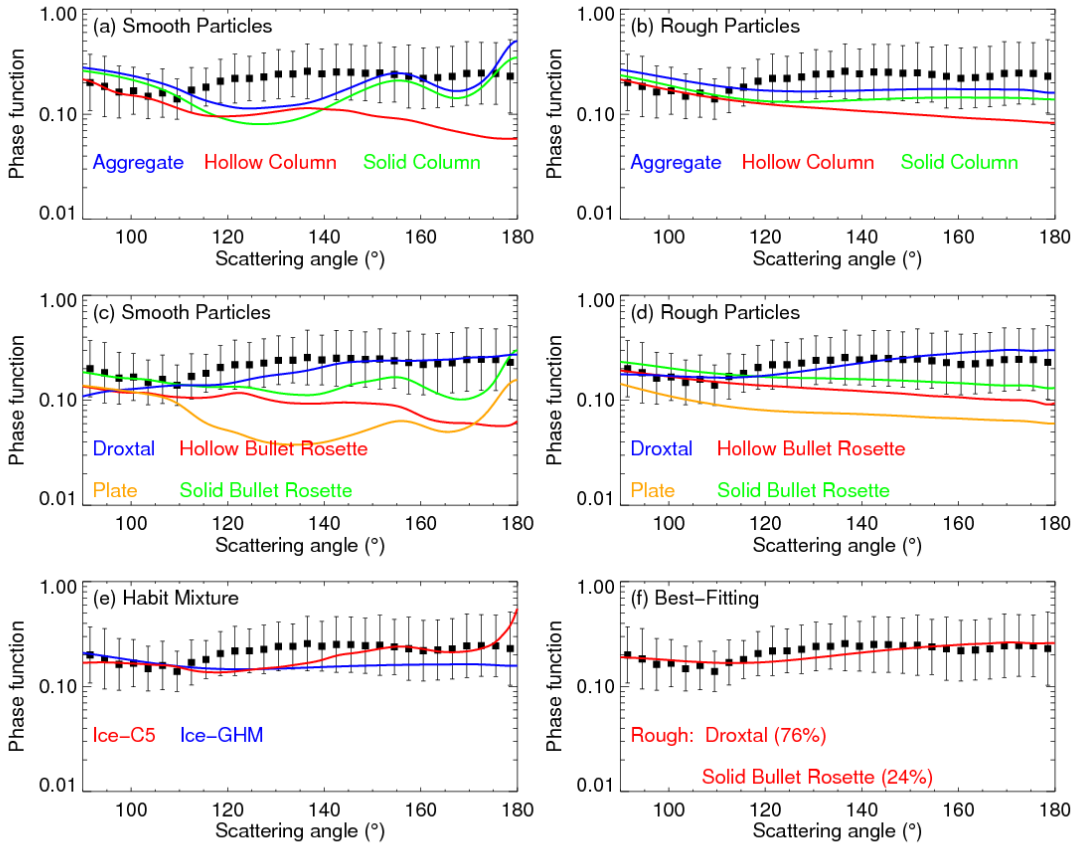

Fig.5.16 Same as Fig.5.15, but for comparisons between theoretical scattering phase functions and inferred scattering phase function of thin cirrus clouds over land.

For optically thin cirrus clouds over land, it is difficult to match the inferred scattering phase function by using current idealized habits. Fig. 5.16 shows the comparisons between theoretical scattering phase functions and inferred scattering phase function of thin cirrus clouds over land. For scattering angles larger than 120°, almost all of the ideal habits have smaller scattering phase function in comparison with the inferred

one, except the droxtal. For this reason, the best-fitted habits mixture consists of 74% severely roughened droxtals and 26% severely roughened solid bullet rosettes. Generally speaking, more uncertainties are associated with the inferred phase function over land. More studies are required to investigate the difference the oceanic and terrestrial thin cirrus clouds.

The effective particle size can be obtained using the IR-based retrieval with the two best-fitted microphysical models for thin cirrus clouds. If the oceanic and terrestrial thin cirrus cloud habits mixtures are used for corresponding surface types, the annual averaged D_{eff} geographical distributions of all ice cloud samples and thin cirrus samples are shown in Fig.5.17 (a) and (b), respectively. The pattern of D_{eff} distribution is similar to the τ distribution pattern for all ice cloud samples. For thin cirrus clouds, the D_{eff} values of oceanic clouds are generally larger than their terrestrial counterparts. More details about the statistics of D_{eff} retrievals of thin cirrus clouds can be found in Table 5.1.

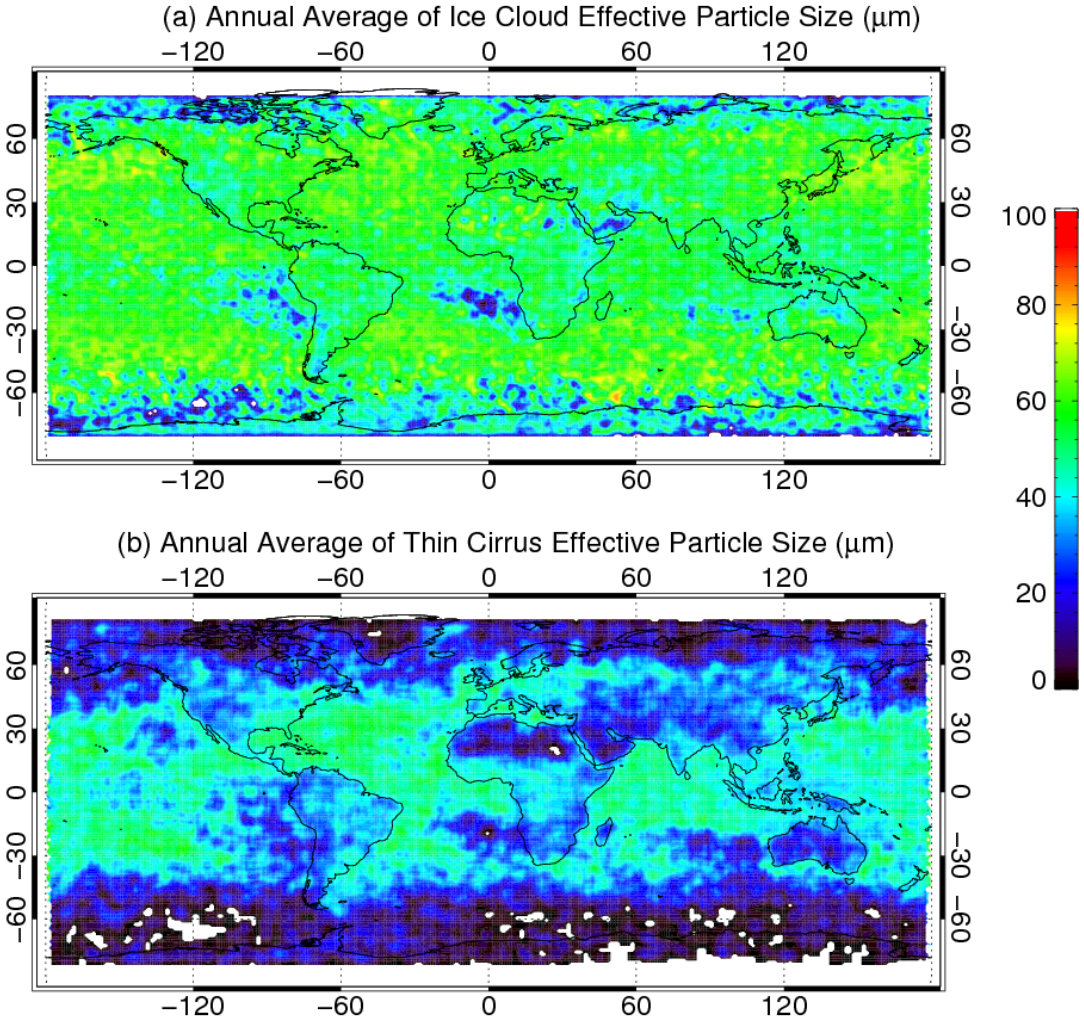

Fig.5.17 Annual averaged IR-based D_{eff} distribution patterns of (a) ice clouds, and (b) thin cirrus clouds ($\tau < 0.3$).

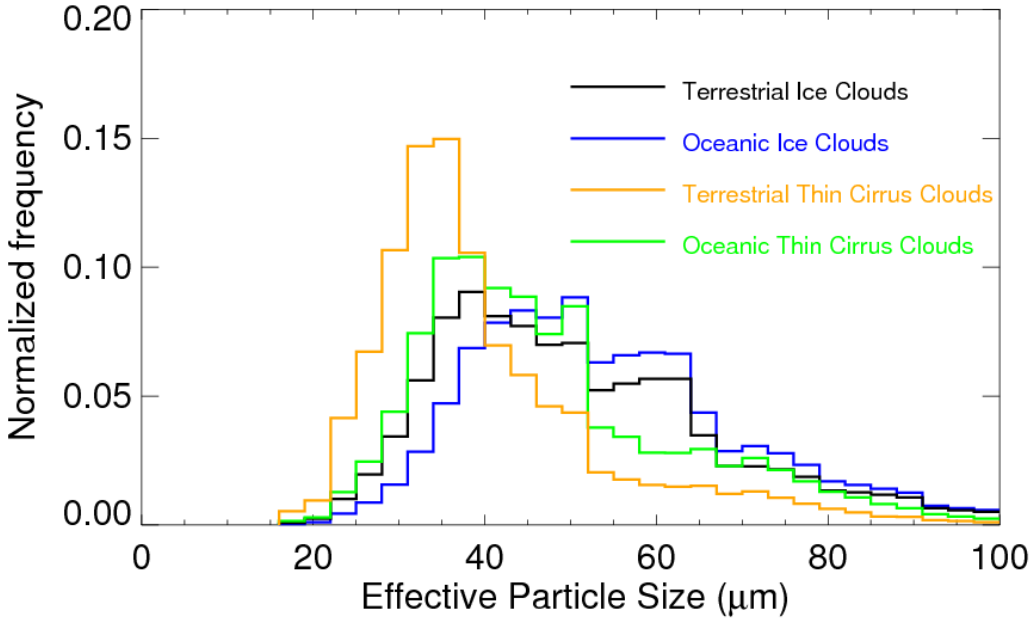

Fig.5.18 Normalized Frequencies of D_{eff} for terrestrial ice clouds (black), oceanic ice clouds (blue), terrestrial thin cirrus clouds (orange), and oceanic thin cirrus clouds (green).

Table 5.1 Global annual means of τ and D_{eff} for ice cloud and thin cirrus cloud samples.

Cloud Properties (Global Annual Mean)		Cloud Optical Thickness	Effective Particle Size (μm)
Ice Cloud	Global	2.56	53.7
	Oceanic	2.54	54.3
	Terrestrial	2.64	50.8
Thin Cirrus	Global	0.18	47.1
	Oceanic	0.18	47.8
	Terrestrial	0.19	40.3

5.5 Conclusions

We develop a new approach to investigate the optical and microphysical properties of global thin cirrus clouds statistically. In order to reduce the impact from surface reflection and highlight thin cirrus clouds in upper troposphere, we utilize the MODIS observations in a strong water vapor absorptive band (1.38-μm) to retrieve scattering phase functions of thin cirrus clouds globally. Moreover, an IR-based retrieval method, in conjunction with a fast forward RTM (i.e., the HRTM), is applied to infer τ that is independent to the pre-assumed ice cloud microphysical properties. Based on one year of MODIS observations in the 1.38-μm band and corresponding τ values retrieved by using three MODIS infrared channels (i.e., the 8.5-, 11-, and 12-μm), the scattering phase function of thin cirrus clouds are inferred approximately with Eq. 5.4.

Comparisons between the inferred and theoretical phase functions reveal that roughened solid columns, droxtals, and smooth column aggregates may dominate thin cirrus clouds over ocean. A habits mixture for oceanic thin cirrus clouds is suggested by fitting the inferred cloud scattering phase function with theoretical phase functions of different ice crystals. To be more specific, the ensemble of 55% severely roughened solid columns, 35% severely roughened droxtals, and 10% smooth aggregates almost perfectly match the inferred scattering phase function. The inferred scattering phase function of optically thin cirrus clouds over land represents relatively strong oscillations in comparison with its oceanic counterpart. It is difficult to use theoretical phase functions to match the terrestrial cirrus phase function. A possible reason is more terrestrial thin cirrus clouds may be initiated by deep convection, leading to a larger

portion of irregular ice crystals during collision processes than ice particles in oceanic cirrus clouds. In comparison with oceanic region, analysis of ice crystal habits in thin cirrus clouds over land is much more difficult due to the large uncertainties associated with surface temperature and emissivity, which impact the IR-based τ retrieval.

Optically thin cirrus clouds with τ less than 0.3 frequently occurs in tropics. The global averaged τ of thin cirrus cloud is 0.18. Different from the optical thickness distribution of all ice clouds that has a similar geographical pattern as the occurrence frequency, the optical thickness distribution has little relationship with its frequency of occurrence. Furthermore, little difference of optical properties can be found between oceanic and terrestrial thin cirrus clouds. For cloud effective particle size, the thin cirrus clouds are composed of relatively small ice crystals in comparison with the optically thick ice clouds. The global mean D_{eff} values of all ice cloud and thin cirrus samples are 54 and 47 μm, respectively. Meanwhile, the averaged D_{eff} values of the two different ice cloud types exhibit strong spatial dependence, that is, the D_{eff} values of oceanic ice clouds are systematically larger than their terrestrial counterparts. The difference in effective particle size may be attributed to the different number concentrations of ice nuclei and updraft velocities. However, further studies focusing on the differences between oceanic and terrestrial thin cirrus clouds are necessary.

CHAPTER VI

SUMMARY

Thin cirrus clouds (visible optical thickness values less than 0.3) impact the radiation budget of the Earth-Atmosphere system by reflecting solar radiation and emitting upwelling longwave radiation at a low temperature. Modeling of these clouds requires knowledge of their microphysical and optical properties. In this dissertation, we introduce a new approach to infer ice crystal sizes and habits (shapes) of global thin cirrus clouds from one year of satellite observations.

Retrievals of cloud depend on the pre-assumed cloud microphysical parameterization scheme, which is a major source of uncertainty in both remote sensing and climate studies. In order to investigate the impacts from cloud microphysics, we develop two fast RTMs in two different spectral regions (i.e., SRTM and HRTM) and two RTM-based retrieval algorithms. In Chapter II and Chapter III, we introduce the principles and features of the two fast models. The SRTM simulates solar reflected radiance (or reflectivity) and the TOA under different cloud-surface conditions. The HRTM calculates TOA BTs with a high-spectral resolution under single-layer cloud condition. The two models utilize pre-computed LUTs specifying cloud absorption and scattering properties calculated by the rigorous DISORT to speed up calculations.

Two retrieval methods are discussed in Chapter IV. Elaborated sensitivity studies are conducted in this chapter to understand the advantages of the two methods. The SRTM-based retrieval is sensitive to the surface reflectivity and ice crystal habits and

degrees of surface roughness. Meanwhile, this method performs best if cloud optical thickness is larger than 5. The IR-based method, which is sensitive to ambient conditions, surface temperature and emissivity, and cloud location, has largest sensitivity if cloud is optically thin and ice crystals are small. Most importantly, by retrieving exactly the same ice cloud samples with different cloud microphysical parameterization schemes, we conclude that the IR-based retrieval method could be considered to be an appropriate approach to infer independent cloud optical thickness. Therefore, in this study, the IR-based method is employed to conduct the global retrieval of optically thin cirrus clouds.

Finally, we develop a new approach to explore the optical and microphysical properties of global optically thin cirrus clouds by making full use of the independent IR-based cloud optical thickness. The cloud microphysical properties are deduced from the averaged bulk scattering phase function of thin cirrus clouds. Comparing the inferred cloud phase function to the numerically simulated phase functions using idealized ice crystal habits, two best-fitted habits mixtures are suggested to represent thin cirrus clouds over ocean and land, respectively. The thin cirrus clouds over ocean may consist of severely roughened column-like particles and a fraction of droxtals. The inferred scattering phase function of terrestrial thin cirrus clouds, however, shows relatively strong oscillations in side through backward directions and is difficult to be matched by using an ensemble of theoretical phase functions. In comparison with optically thick ice clouds, the optically thin cirrus clouds are composed of small ice crystals. The global averaged D_{eff} value of the optically thin cirrus clouds is 47 μm. Furthermore, the

particles within oceanic thin cirrus clouds are systematically larger than particles in terrestrial thin cirrus clouds. Further studies are necessary to understand the differences between the oceanic and terrestrial thin cirrus clouds.

REFERENCES

Ackerman, S. A., R. E. Holz, R. Frey, E. W. Eloranta, B. C. Maddux, and M. McGill, 2008: Cloud detection with MODIS. Part II: Validation. *J. Atmos. Oceanic Technol.*, **25,** 1073-1086, doi:10.1175/2007JTECHA1053.1.

Ambartzumian, V. A., 1958: *Theoretical astrophysics*. Pergamon Press, New York.

Arking, A. and K. Grossman, 1972: The influence of line shape and band structure on temperatures in planetary atmospheres. *J. Atmos.Sci.*, **29,** 937-949.

—— and J. D. Childs, 1985: Retrieval of cloud cover parameters from multispectral satellite images. *J. Climate Appl. Meteor.*, **24,** 322-333.

Armbruster, W. and J. Fischer, 1996: Improved method of exponential sum fitting of transmissions to describe the absorption of atmospheric gases. *Appl. Opt.*, **35,** 1931-1941.

Aumann, H. H., M. T. Chahine, C. Gautier, M. D. Goldberg, E. Kalnay, L. M. McMillin, H. Revercomb, P. W. Rosenkranz, W. L. Smith, D. H. Staelin, L. L. Strow, and J. Susskind, 2003: AIRS/AMSU/HSB on the *Aqua* mission: Design, science objectives, data products, and processing systems. *IEEE Trans. Geosci. Remote Sens.*, **41,** 253-264.

Baran, A. J. and P. N. Francis, 2004a: On the radiative properties of cirrus cloud at solar and thermal wavelength: A test of model consistency using high-resolution airborn radiance measurements. *Q. J. R. Meteorol. Soc.*, **130,** 763-778.

——, 2004b: On the scattering and absorption properties of cirrus cloud. *J. Quant. Spectrosc. Radiat. Transfer*, **89,** 17-36.

——, 2009: A review of the light scattering properties of cirrus. *J. Quant. Spectrosc. Radiat. Transfer*, **110,** 1239-1260.

Baum, B. A., A. J. Heymsfield, P. Yang, and S. T. Bedka, 2005a: Bulk scattering models for the remote sensing of ice clouds. Part I: Microphysical data and models. *J. Appl. Meteor.*, **44,** 1885-1895.

——, P. Yang, A. J. Heymsfield, S. Platnick, M. D. King, Y. X. Hu, and S. T. Bedka, 2005b: Bulk scattering models for the remote sensing of ice clouds. Part II: Narrowband models. *J. Appl. Meteor.*, **44,** 1896-1911.

——, ——, S. L. Nasiri, A. K. Heidinger, A. J. Heymsfield, and J. Li, 2007: Bulk scattering models for the remote sensing of ice clouds. Part III: High-resolution spectral models from 100 to 3250 cm^{-1}. *J. Appl. Meteor.*, **46,** 423-434.

——, ——, Y. X. Hu, and Q. Feng, 2010: The impact of ice particle roughness on the scattering phase matrix. *J. Quant. Spectrosc. Radiat. Transfer*, **111,** 2534-2549.

——, ——, A. J. Heymsfield, C. Schmitt, Y. Xie, A. Bansemer, Y. X. Hu, and Z. Zhang, 2011: Improvements to shortwave bulk scattering and absorption models for the remote sensing of ice clouds. *J. Appl. Meteor. Clim.*, **50,** 1037-1056.

Bi, L., P. Yang, G. W. Kattawar, and R. Kahn, 2008: Single-scattering properties of tri-axial ellipsoidal particles for a size parameter range from the Rayleigh to geometric-optics regimes. *Appl. Opt.*, **48,** 114-126.

——, ——, ——, B. A. Baum, Y. X. Hu, D. M. Winker, R. S. Brock, and J. Q. Lu, 2009: Simulation of the color ratio associated with the backscattering of radiation by ice particles at the wavelengths of 0.532 and 1.064 μm. *J. Geophys. Res.*, **114,** D00H08, doi:10.1029/2009JD011759.

——, ——, ——, Y. X. Hu, and B. A. Baum, 2011a: Diffraction and external reflection by dielectric faceted particles. *J. Quant. Spectrosc. Radiat. Transfer*, **112,** 163-173.

——, ——, ——, ——, and ——, 2011b: Scattering and absorption of light by ice particles: Solution by a new physical-geometric optics hybrid method. *J. Quant. Spectrosc. Radiat. Transfer*, **112,** 1492-1508.

Bodhaine, B. A., N. B. Wood, E. G. Dutton, and J. R. Slusser, 1999: On Rayleigh optical depth calculations. *J. Atmos. Oceanic Technol.*, **16,** 1854-1861.

Blumstein, D., G. Chalon, T. Carlier, C. Buil, P. Hebert, T. Maciaszek, G. Ponce, T. Phulpin, B. Tournier, D. Simeoni, P. Astruc, A. Clauss, G. Kayal, and R. Jegou, 2004: IASI instrument: Technical overview and measured performances. *Infrared Spaceborne Remote Sensing XII, SPIE*, **5543,** 196-207.

Boehm, M. T. and J. Verlinde, 2000: Stratospheric influence on upper tropospheric tropical cirrus. *Geophys. Res. Lett.*, **27,** 3209-3212, doi:10.1029/2000GL011678.

—— and S. Lee, 2003: The implications of tropical Rossby waves for tropical tropopause cirrus formation and for the equatorial upwelling of the Brewer-Dobson circulation. *J. Atmos. Sci.*, **60,** 247-261.

Chandrasekhar, S., 1960: *Radiative transfer*, Dover Publications, New York.

Chepfer, H., G. Brogniez, and Y. Fouquart, 1998: Cirrus clouds' microphysical properties deduced from POLDER observations. *J. Quant. Spectrosc. Radiat. Transfer*, **60,** 375-390.

——, G. Cesana, D. Winker, B. Getzewich, M. Vaughan, and Z. Liu, 2013: Comparison of two different cloud climatologies derived from CALIOP-attenuated backscattered measurements (Level 1): The CALIPSO-ST and the CALIPSO-GOCCP. *J. Atmos. Oceanic Technol.*, **30,** 725-744, doi:10.1175/JTECH-D-12-00057.1.

Chiriaco, M., H. Chepfer, V. Noel, A. Delaval, M. Haeffelin, P. Dubuisson, and P. Yang, 2004: Improving retrievals of cirrus cloud particle size coupling lidar and three-channel radiometric techniques. *Mon. Wea. Rev.*, **132,** 1684-1700.

——, R. Vautard, H. Chepfer, M. Haeffelin, Y. Wanherdrick, Y. Morille, A. Protat, J. Dudhia, and C. F. Mass, 2006: The ability of MM5 to simulate thin ice clouds: Systematic comparisons with lidar/radar and fluxes measurements. *Mon. Wea. Rev.*, **134,** 897-918.

Clough, S. A., F. X. Kneizys, and R. W. Davies, 1989: Line shape and the water vapor continuum. *Atmos. Res.*, **23,** 229-241.

——, M. J. Iacono, and J.-L, Moncet, 1992: Line-by-line calculations of atmospheric fluxes and cooling rates: Application to water vapor. *J. Geophys. Res.*, **97,** 15761-15785.

——, M. W. Shephard, E. J. Mlawer, J. S. Delamere, M. J. Iacono, K. Candy-Pereira, S. Boukabara, and P. D. Brown, 2005: Atmospheric radiative transfer modeling: A summary of the AER codes. *J. Quant. Spectrosc. Radiat. Transfer*, **91,** 233-244.

Collins, D. G., W. G. Blattner, M. B. Wells, and H. G. Horak, 1972: Backward Monte Carlo Calculations of the Polarization Characteristics of the Radiation Emerging from Spherical-Shell Atmospheres. *Appl. Opt.*, **11,** 2684-2696.

Cooper, S. J. and T. J. Garrett, 2010: Identification of small ice cloud particles using passive radiometric observations. *J. Appl. Meteor. Climatol.*, **49,** 2334-2347.

Cox, C. and W. Munk, 1954: Measurement of the Roughness of the Sea Surface from Photographs of the Suns Glitter. *J. Opt. Soc. Am.*, **44,** 838-850.

de Reus, M., S. Borrmann, A. Bansemer, A. J. Heymsfield, R. Weigel, C. Schiller, V. Mitev, W. Frey, D. Kunkel, A. Kürten, J. Curtius, N. M. Sitnikov, A. Ulanovsky, and F. Ravegnani, 2009: Evidence for ice particles in the tropical stratosphere from in-situ measurements. *Atmos. Chem. Phys.*, **9,** 6775-6792.

Derber, J. C., D. F. Parrish, and S. J. Lord, 1991: The new global operational analysis system at the National Meteorological Center. *Wea. Forecasting*, **6,** 538-547.

Dessler, A. E. and P. Yang, 2003: The distribution of tropical thin cirrus clouds inferred from *Terra* MODIS Data. *J. Clim.*, **16,** 1241-1247.

——, S. P. Palm, and J. D. Spinhirne, 2006: Tropical cloud-top height distributions revealed by the Ice, Cloud, and Land Elevation Satellite (ICESat)/Geoscience Laser Altimeter System (GLAS). *J. Geophys. Res.*, **111,** D12215, doi:10.1029/2005JD006705.

Dubuisson, P., V. Giraud, O. Chomette, H. Chepfer, and J. Pelon, 2005: Fast radiative transfer modeling for infrared imaging radiometry. *J. Quant. Spectrosc. Radiat. Transfer*, **95,** 201-220.

Eguchi, N., T. Yokota, and G. Inoue, 2007: Characteristics of cirrus clouds from ICESat/GLAS observations. *Geophys. Res. Lett.*, **34,** L09810, doi:10.1029/2007GL029529.

Field, P. R., A. J. Heymsfield, A. Bansemer, 2006: Shattering and particle interarrival times measured by optical array probes in ice clouds. *J. Atmos. Oceanic Technol.*, **23,** 1357-1371, doi:10.1175/JTECH1922.1.

Fu, Q., 1996: An accurate parameterization of the solar radiative properties of cirrus clouds for climate models. *J. Climate*, **9,** 2058-2082.

Fujiwara, M., S. Iwasaki, A. Shimizu, Y. Inai, M. Shiotani, F. Hasebe, I. Matsui, N. Sugimoto, H. Okamoto, N. Nishi, A. Hamada, T. Sakazaki, and K. Yoneyama, 2009: Cirrus observations in the tropical tropopause layer over the western Pacific. *J. Geophys. Res.*, **114,** D09304, doi:10.1029/2008JD011040.

Gallery, W. O., F. X. Kneizys, and S. A. Clough, 1983: Air mass computer program for atmospheric transmittance/radiance calculations: FSCATM. *Air Force Geophys*. **Laboratory Rep. AFGL-TR-83-0065**, Hanscom AFB, MA.

Gao, B.-C., Y. J. Kaufman, W. Han, R.-R. Li, and W. J. Wiscombe, 1998: Correction of thin cirrus path radiances in the 0.4-1.0 μm spectral region using the sensitive 1.375 μm cirrus detecting channel. *J. Geophys. Res.*, **103,** 32169-32176, doi:10.1029/98JD02006.

——, P. Yang, W. Han, R.-R. Li, and W. J. Wiscombe, 2002: An algorithm using visible and 1.375-μm channels to retrieve cirrus cloud reflectances from aircraft and satellite data. *IEEE Trans. Geosci. Remote Sens.*, **40,** 1659-1668.

——, K. Meyer, and P. Yang, 2004: A new concept on remote sensing of cirrus optical depth and effective ice particle size using strong water vapor absorption channels near

1.38 and 1.88 μm. *IEEE Trans. Geosci. Remote Sens.*, **42,** 1891-1899, doi:10.1109/TGRS.2004.833778.

Garnier, A., J. Pelon, P. Dubuisson, M. Faivre, O. Chomette, N. Pascal, and D. P. Kratz, 2012: Retrieval of cloud properties using CALIPSO Imaging Infrared Radiometer. Part I: Effective emissivity and optical depth. *J. Appl. Meteor. Climatol.*, **51,** 1407-1425, doi:10.1175/JAMC-D-11-0220.1.

Goody, R., R. West, L. Chen, and D. Crisp, 1989: The correlated-k method for radiation calculations in nonhomogeneous atmospheres. *J. Quant. Spectrosc. Radiat. Transfer*, **42,** 539-550.

Górski, K. M., E. Hivon, A. J. Banday, B. D. Wandelt, F. K. Hansen, M. Reinecke, and M. Bartelman, 2005: HEALPix: A Framework for High-Resolution Discretization and Fast Analysis of Data Distributed on the Sphere. *Astrophys. J.*, **622,** 759-771.

Haladay, T. and G. Stephens, 2009: Characteristics of tropical thin cirrus clouds deduced from joint CloudSat-CALIPSO observations. *J. Geophys. Res.*, **114,** D00A25, doi:10.1029/2008JD010675.

Hale, G. M. and M. R. Querry, 1973: Optical Constants of Water in the 200-nm to 200-μm Wavelength Region. *Appl. Opt.*, **12,** 555-563.

Han, Y., 2010: A rapid radiative transfer model for SSMIS UAS channels that takes the earth-rotation doppler shift and Zeeman effects into account. *Microwave Radiometry and Remote Sensing of the Environment (MicroRad)*, **2010 11th Specialist Meeting on 2010**, 37-42.

Hansen J. E. and J. W. Hovenier, 1971a: The doubling method applied to multiple scattering of polarized light. *J. Quant. Spectrosc. Radiat. Transfer*, **11,** 809-812.

——, 1971b: Multiple scattering of polarized light in planetary atmospheres. Part 2: Sunlight reflected by terrestrial water clouds. *J. Atmos. Sci.*, **28,** 1400-1426.

—— and L. D. Travis, 1974: Light scattering in planetary atmospheres. *Space Science Reviews*, **16,** 527-610.

Hartmann, D. L. and D. A. Short, 1980: On the use of earth radiation budget statistics for studies of clouds and climate. *J. Atmos. Sci.*, **37,** 1233-1250.

——, J. R. Holton, and Q. Fu, 2001: The heat balance of the tropical tropopause, cirrus, and stratospheric dehydration. *Geophys. Res. Lett.*, **28,** 1969-1972.

Heidinger, A. K., C. O'Dell, R. Bennartz, and T. Greenwald, 2006: The successive-order-of-interaction radiative transfer model. Part I: Model development. *J. Appl. Meteor. Clim.*, **45,** 1388-1402.

—— and M. J. Pavolonis, 2008: Gazing at cirrus clouds for 25 years through a split window. Part I: Methodology. *J. Appl. Meteor. Climatol.*, **48,** 1100-1116.

Heikes, R. and D. A. Randall, 1995a: Numerical-Integration of the Shallow-Water Equations on a Twisted Icosahedral Grid. 1. Basic Design and Results of Tests. *Mon. Wea. Rev.*, **123,** 1862-1880.

—— and ——, 1995b: Numerical-Integration of the Shallow-Water Equations on a Twisted Icosahedral Grid. 2. A Detailed Description of the Grid and an Analysis of Numerical Accuracy. *Mon. Wea. Rev.*, **123,** 1881-1887.

Herman, G. F., M. C. Wu, and W. T. Johnson, 1980: The effect of clouds on the earth's solar and infrared radiation budgets. . *J. Atmos. Sci.*, **37,** 1251-1261.

Hess, M., R. B. A. Koelemeijer, and P. Stammes, 1998: Scattering matrices of imperfect hexagonal ice crystals. *J. Quant. Spectrosc. Radiat. Transfer*, **60,** 301-308.

Heymsfield, A. J. and J. Jahnsen, 1974: Microstructure of tropopause cirrus layers. *Proc. 6th Conf. Aerosp. Aeronaut. Meteorol.*, 43-48.

——, 1986: Ice particles observed in a cirriform cloud at −83°C and implications for polar stratospheric clouds. *J. Atmos. Sci.*, **43,** 851-855.

—— and L. M. Miloshevich, 1995: Relative humidity and temperature influences on cirrus formation and evolution: Observations from wave clouds and FIRE-II. *J. Atmos. Sci.*, **52,** 4302-4326.

—— and G. M. McFarquhar, 1996: On the high albedos of anvil cirrus in the tropical Pacific warm pool: Microphysical interpretations from CEPEX and from Kwajalein, Marshall Islands. *J. Atmos. Sci.*, **53,** 2424-2451.

—— and J. Iaquinta, 2000: Cirrus crystal terminal velocities. *J. Atmos. Sci.*, **57,** 916-938.

——, A. Bansemer, P. R. Field, S. L. Durden, J. L. Stith, J. E. Dye, W. Hall, and C. A. Grainger, 2002: Observations and parameterizations of particle size distributions in deep tropical cirrus and stratiform precipitation clouds: Results from in situ observations in TRMM field campaigns. *J. Atmos. Sci.*, **59,** 3457-3491.

——, A. Bansemer, C. G. Schmitt, C. Twohy, and M. R. Poellet, 2004: Effective ice particle densities derived from aircraft data. *J. Atmos. Sci.*, **61,** 982-1003.

Hintsa, E. J., K. A. Boering, E. M. Weinstock, J. G. Anderson, B. L. Gary, L. Pfister, B. C. Daube, S. C. Wofsy, M. Loewenstein, J. R. Podolske, J. J. Margitan, T. P. Bui, 1998: Troposphere-to-stratosphere transport in the lowermost stratosphere from measurements of H_2O, CO_2, N_2O, and O_3. *Geophys. Res. Lett.*, **25,** 2655-2658, doi:10.1029/98GL01797.

Holz, R. E., S. A. Ackerman, F. W. Nagle, R. A. Frey, S. Dutcher, R. E. Kuehn, M. A. Vaughan, and B. A. Baum, 2008: Global Moderate Resolution Imaging Spectroradiometer (MODIS) cloud detection and height evaluation using CALIOP. *J. Geophys. Res.*, **113,** D00A19, doi:10.1029/2008JD009837.

Hong, G., P. Yang, H.-L. Huang, B. A. Baum, Y. X. Hu, and S. Platnick, 2007: The sensitivity of ice cloud optical and microphysical passive satellite retrievals to cloud geometrical thickness. *IEEE Trans. Geosci. Remote Sens.*, **45,** 1315-1323.

Hsu, N. C., S. C. Tsay, M. D. King, and J. R. Herman, 2004: Aerosol properties over bright-reflecting source regions. *IEEE Trans. Geosci. Remote Sens.*, **42,** 557-569.

——, ——, ——, and ——, 2006: Deep Blue retrievals of Asian aerosol properties during ACE-Asia. *IEEE Trans. Geosci. Remote Sens.*, **44,** 3180-3195.

Hu, Y. X., B. Wielicki, B. Lin, G. Gibson, S. C. Tsay, K. Stamnes, and T. Wang, 2000: δ-Fit: A fast and accurate treatment of particle scattering phase functions with weighted singular-value decomposition least-squares fitting. *J. Quant. Spectrosc. Radiat. Transfer*, **65,** 681-690.

Huang, H.-L., P. Yang, H. Wei, B. A. Baum, Y. X. Hu, P. Antonelli, and S. A. Ackerman, 2004: Inference of ice cloud properties from high spectral resolution infrared observations. *IEEE Trans. Geosci. Remote Sens.*, **42,** 842-850.

Immler, F., K. Krüger, M. Fujiwara, G. Verver, M. Rex, and O. Schrems, 2008: Correlation between equatorial Kelvin waves and the occurrence of extremely thin ice clouds at the tropical tropopause. *Atmos. Chem. Phys.*, **8,** 4019-4026.

Inoue, T., 1985: On the temperature and effective emissivity determination of semi-transparent cirrus clouds by bi-spectral measurements in the 10 micron window region. *Meteorological Society of Japan*, **63,** 88-99.

Jensen, E. J., O. B. Toon, H. B. Selkirk, J. D. Spinhirne, and M. R. Schoeberl, 1996: On the formation and persistence of subvisible cirrus clouds near the tropical tropopause. *J. Geophys. Res.*, **101,** 21361-21376.

——, L. Pfister, S. A. Ackerman, A. Tabazadeh, and O. Toon, 2001: A conceptual model of the dehydration of air due to freeze-drying by optically thin, laminar cirrus rising slowly across the tropical tropopause. *J. Geophys. Res.*, **106,** 17237-17252.

Jin, X. and J. Li, 2010: Improving moisture profile retrieval from broadband infrared radiances with an optimized first-guess scheme. *Remote Sens. Lett.*, **1,** 213-238.

Khvorostyanov, V. I. and K. Sassen, 2002: Microphysical processes in cirrus and their impact on radiation: *A mesoscale modeling perspective*, in *Cirrus*, Oxford University Press, New York.

King, M. D., S. C. Tsay, S. Platnick, M. Wang, and K. N. Liou, 1997: Cloud retrieval algorithms for MODIS: Opitcal thickness, effective particle radius, and thermodynamic phase. *MODIS algorithm theoretical basis document*, **ATBD-MOD-05,** 78 pp.

——, W. P. Menzel, Y. J. Kaufman, D. Tanre, B.-C. Gao, S. Platnick, S. A. Ackerman, L. A. Remer, R. Pincus, and P. A. Hubanks, 2003: Cloud and aerosol properties, precipitable water, and profiles of temperature and water vapor from MODIS. *IEEE Trans. Geosci. Remote Sens.*, **41,** 442-458.

Kokhanovsky, A. A. and T. Nauss, 2005: Satellite-based retrieval of ice cloud properties using a semianalytical algorithm. *J. Geophys. Res.*, **110,** D19206, doi:10.1029/2004JD005744.

Kosarev, A. L. and I. P. Mazin, 1991: An empirical model of the physical structure of upper layer clouds. *Atmos. Res.*, **26,** 213-228.

Kratz, D. P., 1995: The correlated k-distribution technique as applied to the AVHRR channels. *J. Quant. Spectrosc. Radiat. Transfer*, **53,** 501-517.

Kuo, C. C, D. H. Staelin, and P. W. Rosenkranz, 1994: Statistical iterative scheme for estimating atmospheric relative-humidity profiles. *IEEE Trans. Geosci. Remote Sens.*, **32,** 254-260.

Lacis, A., W. C. Wang, and J. Hansen, 1979: Correlated k-distribution method for radiative transfer in climate models: Application to effect of cirrus clouds on climate. *NASA conf. Publ.*, **2076,** 309-314.

—— and V. Oinas, 1991: A description of the correlated k-distribution method for modeling nongray gaseous absorption, thermal emission, and multiple scattering in vertically inhomogeneous atmospheres. *J. Geophys. Res.*, **96,** 9027-9063.

Lee, J., P. Yang, A. E. Dessler, B.-C. Gao, and S. Platnick, 2009: Distribution and radiative forcing of tropical thin cirrus clouds. *J. Atmos. Sci.*, **66,** 3721-3731.

Levoni, C., M. Cervino, R. Guzzi, and F. Torricella, 1997: Atmospheric aerosol optical properties: a database of radiative characteristics for different components and classes. *Appl. Opt.*, **36,** 8031-8041.

Li, X. and A. H. Strahler, 1992: Geometric-optical bidirectional reflectance modeling of the discrete crown vegetation canopy: Effect of crown shape and mutual shadowing. *IEEE Trans. Geosci. Remote Sens.*, **30,** 276-292.

Li, Y., G. R. North, P. Yang, and B. A. Baum, 2010: Exploration of the MODIS cloud-top property products for the investigation of equatorial wave system. *J. Appl. Meteor. Clim.*, **49,** 2050-2057.

Liou, K. N., 1986: Influence of cirrus clouds on weather and climate processes: A global perspective. *Mon. Wea. Rev.*, **114,** 1167-1199.

——, 2002: *An introduction to atmospheric radiation*. Academic Press, San Diego, CA.

Liu, X., W. L. Smith, D. K. Zhou, and A. Larar, 2006: Principal component-based radiative transfer model for hyperspectral sensors. *Appl. Opt.*, **45,** 201-209.

Lucht, W., C. B. Schaaf, and A. H. Strahler, 2000: An algorithm for the retrieval of albedo from space using semiempirical BRDF models. *IEEE Trans. Geosci. Remote Sens.*, **38,** 977-998.

Luo, Z., and W. B. Rossow, 2004: Characterizing tropical cirrus life cycle, evolution and interaction with upper tropospheric water vapor using Lagrangian trajectory analysis of satellite observations. *J. Clim.*, **17,** 4541-4563, doi:10.1175/3222.1.

Lynch, D. K. and K. Sassen, 2002: *Subvisual cirrus*, in *Cirrus*, Oxford University Press, New York.

McClatchey, R. A., W. S. Fenn, J. E. A. Selby, F. E. Volz, and J. S. Garing, 1971: *Optical properties of the atmosphere.* Rep. AFCRL-71-0279, 85 pp., Air Forcing Cambridge Res. Lab., Bedford, Mass.

Massie, S. T., J. Gille, C. Craig, R. Khosravi, J. Barnett, W. Read, and D. Winker, 2010: HIRDLS and CALIPSO observations of tropical cirrus. *J. Geophys. Res.*, **115,** D00H11, doi:10.1029/2009JD012100.

McFarquhar, G. M., A. J. Heymsfield, J. Spinhirne, and B. Hart, 2000: Thin and subvisual tropopause tropical cirrus: Observations and radiative impacts. *J. Atmos., Sci.*, **57,** 1841-1853.

Meirink, J. F., R. Roebelling, E. Wolters, and H. Deneke, 2010: Algorithm theoretical basis document Cloud Physical Products AVHRR/SEVIRI. *EUMETSAT*.

Menzel, W. P., W. L. Smith, and T. R. Stewart, 1983: Improved Cloud Motion Wind Vector and Altitude Assignment Using VAS. *J. Climate Appl. Meteor.*, **22,** 377-384.

—— and Coauthors, 2008: MODIS global cloud-top pressure and amount estimation: Algorithm description and results. *J. Appl. Meteor. Climatol.*, **47,** 1175-1198.

Mergenthaler, J. L., A. E. Roche, J. B. Kumer, and G. A. Ely, 1999: Cryogenic Limb Array Etalon Spectrometer observations of tropical cirrus. *J. Geophys. Res.*, **104,** 22183-22194, doi:10.1029/1999JD900397.

Meyer, K., P. Yang, and B.-C. Gao, 2004: Optical thickness of tropical cirrus clouds derived from the MODIS 0.66 and 1.38-μm channels. *IEEE Trans. Geosci. Remote Sens.*, **42,** 833-841, doi:10.1109/TGRS.2003.818939.

—— and S. Platnick, 2010: Utilizing the MODIS 1.38 μm channel for cirrus cloud optical thickness retrievals: Algorithm and retrieval uncertainties. *J. Geophys. Res.*, **115,** D24209, doi:10.1029/2010JD014872.

Miloshevich, L. M. and A. J. Heymsfield, 1997: A balloon-borne continuous cloud particle replicator for measuring vertical profiles of cloud microphysical properties: Instrument design, performace, and collection efficiency analysis. *J. Atmos. Oceanic Technol.*, **14,** 753-768.

Minnis, P. and Coauthors, 2011a: CERES edition-2 cloud property retrievals using TRMM VIRS and *Terra* and *Aqua* MODIS data — Part I: Algorithms. *IEEE Trans. Geosci. Remote Sens.*, **49,** 4347-4400, doi:10.1109/TGRS.2011.2144601.

—— and Coauthors, 2011b: CERES edition-2 cloud property retrievals using TRMM VIRS and *Terra* and *Aqua* MODIS data — Part II: Examples of average results and comparisons with other data. *IEEE Trans. Geosci. Remote Sens.*, **49,** 4401-4430, doi:10.1109/TGRS.2011.2144602.

Mitchell, D. L., 1991: Evolution of snow-size spectra in cyclonic storms. Part II: Deviations from the exponential form. *J. Atmos. Sci.*, **48,** 1885-1899.

——, P. Rasch, D. Ivanova, G. McFarquhar, and T. Nousiainen, 2008: Impact of small ice crystal assumptions on ice sedimentation rates in cirrus clouds and GCM simulations. *Geophys. Res. Lett.*, **35,** L09806, doi:10.1029/2008GL033552.

——, R. P. d'Entremont, and R. P. Lawson, 2010: Inferring cirrus size distribution through satellite remote sensing and microphysical databases. *J. Atmos. Sci.*, **67,** 1106-1125.

Mlawer, E. J., S. A. Clough, and D. C. Tobin, 2003: The MT_CKD water vapor continuum: A revised perspective including collision induced effects. *Proc. 10th Conf. on Atmospheric Science from Space using Fourier Transform Spectrometry*, Bad Wildbad, Germany, Institut für Meteorologie und Klimaforschung.

Mobley, C. D., 1994: *Light and water : radiative transfer in natural waters*. Academic Press, San Diego.

Moncet, J. L., G. Uymin, A. E. Lipton, and H. E. Snell, 2008: Infrared radiance modeling by optimal spectral sampling. *J. Atmos. Sci.*, **65,** 3917-3934.

Morel, A., 1974: Optical properties of pure water and pure sea water. *Optical aspects of oceanography*, Academic Press, New York.

Nakajima, T. and M. D. King, 1990: Determination of the opitcal thickness and effective particle radius of clouds from reflected solar radiation measurements. Part I: Theory. *J. Atmos., Sci.*, **47,** 1878-1893.

Nasiri, S. L., B. A. Baum, A. J. Heymsfield, P. Yang, M. Poellot, D. P. Kratz, and Y. X. Hu, 2002: Development of midlatitude cirrus models for MODIS using FIRE-I, FIRE-II, and ARM in situ data. *J. Appl. Meteor.*, **41,** 197-217.

Niu, J., P. Yang, H.-L. Huang, J. E. Davies, J. Li, B. A. Baum, and Y. X. Hu, 2007: A fast infrared radiative transfer model for overlapping clouds. *J. Quant. Spectrosc. Radiat. Transfer*, **103,** 447-459.

Ohring, G. and P. Clapp, 1980: The effect of changes in cloud amount on the net radiation at the top of the atmosphere. . *J. Atmos. Sci.*, **37,** 447-454.

Omar, A. H. and C. S. Cardner, 2001: Observations by the Lidar In-Space Technology Experiment (LITE) of high-altitude cirrus clouds over the equator in regions exhibiting extremely cold temperatures. *J. Geophys. Res.*, **106,** 1227-1236, doi:10.1029/2000JD900489.

Pfister, L., H. B. Selkirk, E. J. Jensen, M. R. Schoeberl, O. B. Toon, E. V. Browell, W. B. Grant, B. Gary, M. J. Mahoney, T. V. Bui, and E. Hintsa, 2001: Aircraft observations of thin cirrus clouds near the tropical tropopause. *J. Geophys. Res.*, **106,** 9765-9786.

Plass, G. N. and G. W. Kattawar, 1968: Monte Carlo Calculations of Light Scattering from Clouds. *Appl. Opt.*, **7,** 415-419.

Platnick, S. and S. Twomey, 1994: Determining the susceptibility of cloud albedo to changes in droplet concentration with the Advanced Very High Resolution Radiometer. *J. Appl. Meteor.*, **33,** 334-347.

——, J. Y. Li, M. D. King, H. Gerber, and P. V. Hobbs, 2001: A solar reflectance method for retrieving the optical thickness and droplet size of liquid water clouds over snow and ice surfaces. *J. Geophys. Res.*, **106,** 15185-15199, doi:10.1029/2000JD900441.

——, M. D. King, S. A. Ackerman, W. P. Menzel, B. A. Baum, J. C. Riedi, and R. A. Frey, 2003: The MODIS cloud products: Algorithms and examples from Terra. *IEEE Trans. Geosci. Remote Sens.*, **41,** 459-473.

Poulsen, C. A., R. Siddans, G. E. Thomas, A. M. Sayer, R. G. Grainger, E. Campmany, S. M. Dean, C. Arnold, and P. D. Watts, 2012: Cloud retrievals from satellite data using optimal estimation: evaluation and application to ATSR. *Atmos. Meas. Tech.*, **5,** 1889-1910, doi:10.5194/amt-5-1889-2012.

Prabhakara, C., R. S. Fraser, G. Dalu, M. L. C. Wu, R. J. Curran, and T. Styles, 1988: Thin cirrus clouds: Seasonal distribution over oceans deduced from *Nimbus-4* IRIS. *J. Appl. Meteor.*, **27,** 379-399.

——, D. P. Kratz, J. -M. Yoo, G. Dalu, and A. Vernekar, 1993: Optically thin cirrus clouds: Radiative impact on the warm pool. *J. Quant. Spectrosc. Radiat. Transfer*, **49,** 467-483.

Ramanathan, V., L. Callis, R. Cess, J. Hansen, I. Isaksen, W. Kuhn, A. Lacis, F. Luther, J. Mahlman, R. Reck, and M. Schlesinger, 1987: Climate-chemical interactions and effects of changing atmospheric trace gases. *Rev. Geophys.*, **25,** 1441-1482, doi:10.1029/RG025i007p01441.

Rienecker, M. M., M. J. Suarez, R. Todling, J. Bacmeister, L. Takacs, H.-C. Liu, W. Gu, M. Sienkiewicz, R. D. Koster, R. Gelaro, I. Stajner, and J. E. Nielsen, 2008: The GEOS-5 data assimilation system — Documentation of Versions 5.0.1, 5.1.0, and 5.2.0. *Tech. Rep. Ser. on Global Modeling and Data Assimilation*, **27**.

Riihimaki, L. D. and S. A. McFarlane, 2010: Frequency and morphology of tropical tropopause layer cirrus from CALIPSO observations: Are isolated cirrus different from those connected to deep convection? *J. Geophys. Res.*, **115,** D18201, doi:10.1029/2009JD013133.

Rodgers, C. D, 1976: Retrieval of atmospheric-temperature and composition from remote measurements of thermal-radiation. *Rev. Geophys.*, **14,** 609-624.

Rosenfield, J. E., D. B. Considine, M. R. Schoeberl, and E. V. Browell, 1998: The impact of subvisual cirrus clouds near the tropical tropopause on stratospheric water vapor. *Geophys. Res. Lett.*, **25,** 1883-1886, doi:10.1029/98GL01294.

Roskovensky, J. K. and K. N. Liou, 2005: Differentiating airborne dust from cirrus clouds using MODIS data. *Geophys. Res. Lett.*, **32,** L12809, doi:10.1029/2005GL022798.

Ross, J, 1981: *The radiation regime and architecture of plant stands*, Dr. W. Junk, Boston, Mass.

Rothman, L. S. and Coauthors, 2005: The HITRAN 2004 molecular spectroscopic database. *J. Quant. Spectrosc. Radiat. Transfer*, **96,** 139-204.

Ruston, B., F. Weng, and B. Yan, 2008: Use of a one-dimensional variational retrieval to diagnose estimates of infrared and microwave surface emissivity over land for ATOVS sounding instruments. *IEEE Trans. Geosci. Remote Sens.*, **46,** 393-402.

Salomon, J. G., C. B. Schaaf, A. H. Strahler, F. Gao, and Y. Jin, 2006: Validation of the MODIS Bidirectional Reflectance Distribution Function and Albedo retrievals using combined observations from the Aqua and Terra platforms. *IEEE Trans. Geosci. Remote Sens.*, **44,** 1555-1565.

Sassen, K., R. P. Benson, and J. D. Spinhirne, 2000: Tropical cirrus cloud properties derived from TOGA/COARE airborne polarization lidar. *Geophys. Res. Lett.*, **27,** 673-676, doi:10.1029/1999GL010946.

——, Z. Wang, and D. Liu, 2008: Global distribution of cirrus clouds from CloudSat/Cloud-Aerosol Lidar and Infrared Pathfinder Satellite Observations (CALIPSO) measurements. *J. Geophys. Res.*, **113,** D00A12, doi:10.1029/2008JD009972.

——, ——, and ——, 2009: Cirrus clouds and deep covection in the tropics: Insights from CALIPSO and CloudSat. *J. Geophys. Res.*, **114,** D00H06, doi:10.1029/2009JD011916.

Saunders, R., M. Matricardi, and P. Brunel, 1999: An improved fast radiative transfer model for assimilation of satellite radiance observations. *Q. J. R. Meteorol. Soc.*, **125,** 1407-1425, doi:10.1002/qj.1999.49712555615.

——, P. Brunel, S. English, P. Bauer, U. O'Keeffe, P. Francis, and P. Rayer, 2006: RTTOV-8 — Science and validation report. *Met Office Forecasting and Research Tech. Doc*. NWPSAF-MO-TV-007, 46pp.

——, P. Rayer, P. Brunel, A. von Engeln, N. Bormann, L. Strow, S. Hannon, S. Heilliette, X. Liu, F. Miskolczi, Y. Han, G. Masiello, J.-L. Moncet, G. Uymin, V. Sherlock, and D. S. Turner, 2007: A comparison of radiative transfer models for simulating Atmospheric Infrared Sounder (AIRS) radiances. *J. Geophys. Res.*, **112,** D01S90, doi:10.1029/2007JD007088.

Schaaf, C. B., F. Gao, A. H. Strahler, W. Lucht, X. Li, T. Tsang, N. C. Strugnell, X. Zhang, Y. Jin, J.-P. Muller, P. Lewis, M. Barnsley, P. Hobson, M. Disney, G. Roberts, M. Dunderdale, C. Doll, R. P. d'Entremont, B. Hu, S. Liang, J. L. Privette, and D. Roy, 2002: First operational BRDF, albedo nadir reflectance products from MODIS. *Remote Sens. Envion.*, **83,** 135-148.

Schmetz, J., P. Pili, S. Tjemkes, D. Just, J. Kerkmann, S. Rota, and A. Ratier, 2002: An introduction to Meteosat Second Generation (MSG). *Bull. Am. Meteorol. Soc.*, **83,** 977-992.

Smith, W. L. and C. M. R. Platt, 1978: Comparison of satellite-deduced cloud height with indications from radiosonde and ground-based laser measurements. *J. Appl. Meteor.*, **17,** 1796-1802.

Sokolik, I., A. Andronova, and T. C. Johnson, 1993: Complex refractive index of atmospheric dust aerosols. *Atmos. Environ.*, **27A,** 2495-2502.

Solomon, S., K. H. Rosenlof, R. W. Portmann, J. S. Daniel, S. M. Davis, T. J. Sanford, G.-K. Plattner, 2010: Contributions of stratospheric water vapor to decadal changes in the rate of global warming. *Sciences*, **327,** 1219-1223, doi:10.1126/science.1182488.

Stamnes, K., S. C. Tsay, K. Jayaweera, and W. Wiscombe, 1988: Numerically stable algorithm for Discrete-Ordinate-Method Radiative Transfer in multiple scattering and emitting layered media. *Appl. Opt.*, **27,** 2502-2509.

Steinwagner, J., S. Fueglistaler, G. Stiller, T. von Clarmann, M Kiefer, P. P. Borsboom, A. van Delden, and T. Röckmann, 2010: Tropical dehydration processes constrained by the seasonality of stratospheric deuterated water. *Nat. Geosci.*, **3,** 262-266, doi:10.1038/NGEO822.

Stephens, G. L. and Coauthors, 2002: The CloudSat mission and the A-train. *Bull. Am. Meteorol. Soc.*, **83,** 1771-1790.

——, 2005: Cloud feedbacks in the climate system: A critical review. *J. Clim.*, **18,** 237-273.

Strow, L. L., S. E. Hannon, S. De Souza-Machado, H. E. Motteler, and D. Tobin, 2003: An overview of the AIRS radiative transfer model. *IEEE Trans. Geosci. Remote Sens.*, **41,** 303-313.

Stubenrauch, C. J., R. E. Holz, A. Chedin, D. L. Mitchell, and A. J. Baran, 1999: Retrieval of cirrus ice crystal sizes from 8.3 and 11.1 μm emissivities determined by the improved initialization inversion of TIROS-N operational vertical sounder observations. *J. Geophys. Res.*, **104,** 793-808.

——, A. Chédin, G. Rädel, N. A. Scott, and S. Serrar, 2006: Cloud properties and their seasonal and diurnal variability from TOVS Path-B. *J. Clim.*, **19,** 5531-5553.

Stuhne, G. R. and W. R. Peltier, 1999: New icosahedral grid-point discretizations of the shallow water equations on the sphere. *J. Comput. Phys.*, **148,** 23-58.

Sun, W., N. G. Loeb, G. Videen, and Q. Fu, 2004: Examination of surface roughness on light scattering by long ice columns by use of a two-dimensional finite-difference time-domain algorithm. *Appl. Opt.*, **43,** 1957-1964.

Twomey, S., H. Jacobowitz, and H. B. Howell, 1966: Matrix Methods for Multiple-Scattering Problems. *J. Atmos. Sci.*, **23,** 289-298.

Uthe, E. E. and P. B. Russell, 1977: Lidar Observations of tropical high-altitude cirrus clouds. *Radiation in the Atmosphere*, Science press, Princeton.

Vaughan, M. A., K. A. Powell, R. E. Kuehn, S. A. Young, D. M. Winker, C. A. Hostetler, W. H. Hunt, Z. Liu, M. J. McGill, and B. J. Getzewich, 2009: Fully automated detection of cloud and aerosol layers in the CALIPSO lidar measurements. *J. Atmos. Oceanic Technol.*, **26,** 2034-2050, doi:10.1175/2009JTECHA1228.1.

Volz, F. E., 1972: Infrared Refractive Index of Atmospheric Aerosol Substances. *Appl. Opt.*, **11,** 755-759.

Wan, Z. and Z. Li, 1997: A physics-based algorithm for retrieving land-surface emissivity and temperature from EOS/MODIS data. *IEEE Trans. Geosci. Remote Sens.*, **35,** 980-996.

Wang, C., P. Yang, B. A. Baum, S. Platnick, A. K. Heidinger, Y. X. Hu, and R. E. Holz, 2011: Retrieval of ice cloud optical thickness and effective particle size using a fast infrared radiative transfer model. *J. Appl. Meteor. Clim.*, **50,** 2283-2297, doi:10.1175/JAMC-D-11-067.1.

——, S. Ding, P. Yang, B. Baum, and A. E. Dessler, 2012: A new approach to retrieving cirrus cloud height with a combination of MODIS 1.24- and 1.38-μm channels. *Geophys. Res. Lett.*, **39,** L24806, doi:10.1029/2012GL053854.

——, P. Yang, S. Platnick, A. K. Heidinger, B. A. Baum, T. Greenwald, Z. Zhang, and R. E. Holz, 2013a: Retrieval of ice cloud properties from AIRS and MODIS observations based on a fast high-spectral-resolution radiative transfer model. *J. Appl. Meteor. Clim.*, **52,** 710-726, doi:10.1175/JAMC-D-12-020.1.

——, ——, S. Nasiri, S. Platnick, B. A. Baum, A. K. Heidinger, and X. Liu, 2013b: A fast radiative transfer model for visible through shortwave infrared spectral reflectances in clear and cloudy atmospheres. *J. Quant. Spectrosc. Radiat. Transfer*, **116,** 122-131.

Wang, M. and M. D. King, 1997: Correction of Rayleigh scattering effects in cloud optical thickness retrievals. *J. Geophys. Res.*, **102,** 25915-25926.

Wang, P. H., M. P. McCormick, L. R. Poole, W. P. Chu, G. K. Yue, G. S. Kent, and K. M. Skeens, 1994: Tropical high cloud characteristics derived from Sage II extinction measurements. *Atmos. Res.*, **34,** 53-83.

——, P. Minnis, M. McCormick, G. Kent, and K. Skeens, 1996: A 6-year climatology of cloud occurrence frequency from Stratospheric Aerosol and Gas Experiment II observations (1985-1990). *J. Geophys. Res.*, **101,** 29407-29429.

Warren, S. G. and R. E. Brandt, 2008: Optical constants of ice from the ultraviolet to the microwave: A revised compilation. *J. Geophys. Res.*, **113,** D14220, doi:10.1029/2007JD009744.

Watts, P. D., R. Bennartz, and F. Fell, 2011: Retrieval of two-layer cloud properties from multispectral observations using optimal estimation. *J. Geophys. Res.*, **116,** D16203, doi:10.1029/2011JD015883.

Wei, H., P. Yang, J. Li, B. A. Baum, H.-L. Huang, S. Platnick, Y. X. Hu, and L. Strow, 2004: Retrieval of semitransparent ice cloud optical thickness from atmospheric infrared sounder (AIRS) measurements. *IEEE Trans. Geosci. Remote Sens.*, **42,** 2254-2267.

——, X. Chen, R. Rao, Y. Wang, and P. Yang, 2007: A moderate-spectral-resolution transmittance model based on fitting the line-by-line calculation. *Opt. Express*, **15,** 8360-8370.

Wendisch, M. and Coauthors, 2005: Impact of cirrus crystal shape on solar spectral irradiance: A case study for subtropical cirrus. *J. Geophys. Res.*, **105,** D03202, doi:10.1029/2004JD005294.

—— and P. Yang, 2012: *Theory of atmospheric radiative transfer: A compresensive introduction*. Wiley-VCH, Weinheim, Germany.

Weng, F. and Q. Liu, 2003: Satellite data assimilation in numerical weather prediction models. Part I: Forward radiative transfer and Jacobian modeling in cloudy atmospheres. *J. Atmos. Sci.*, **60,** 2633-2646.

——, T. Zhu, B. Yan, 2007: Satellite data assimilation in numerical weather prediction models. Part II: Uses of rain-affected radiances from microwave observations for hurricane vortex analysis. *J. Atmos. Sci.*, **64,** 3910-3925., doi:10.1175/2006JAS2051.1.

Winker, D. M. and M. A. Vaughan, 1994: Vertical distribution of clouds over Hampton, Virginia observed by lidar under the ECLIPS and FIRE ETO progrms. *Atmos. Res.*, **34,** 117-133.
——, R. H. Couch, and M. P. McCormick, 1996: An overview of LITE: NASA's Lidar In-space Technology Experiment. *Proc. IEEE*, **84,** 164-180.

——, and C. Trepte, 1998: Laminar cirrus observed near the tropical tropopause by LITE. *Geophys. Res. Lett.*, **25,** 3351-3354, doi:10.1029/98GL01292.

——, M. A. Vaughan, A. Omar, Y. X. Hu, K. A. Powell, Z. Liu, W. H. Hunt, and S. A. Young, 2009: Overview of the CALIPSO Mission and CALIPSO data processing algorithms. *J. Atmos. Oceanic Technol.*, **26,** 2310-2323, doi:10.1175/2009JTECHA1281.1.

Wiscombe, W. J., 1977: Delta-M method — rapid yet accurate radiative flux calculations for strongly asymmetric phase functions. *J. Atmos. Sci.*, **34,** 1408-1422.

Wylie, D. P. and W. P. Menzel, 1999: Eight years of high cloud statistics using HIRS. *J. Clim.*, **12,** 170-184.

Xie, Y., P. Yang, G. W. Kattawar, P. Minnis, and Y. X. Hu, 2009: Effect of the inhomogeneity of the ice crystals on retrieving ice cloud optical thickness and effective particle size. *J. Geophys. Res.*, **114,** D11203, doi:10.1029/2008JD011216.

Yang, P. and K. N. Liou, 1998: Single-scattering properties of complex ice crystals in terrestrial atmosphere. *Contrib. Atmos. Phys.*, **71,** 223-248.

——, ——, K. Wyser, and D. Mitchell, 2000: Parameterization of the scattering and absorption properties of individual ice crystals. *J. Geophys. Res.*, **105,** 4699-4718.

——, H. Wei, H. L. Huang, B. A. Baum, Y. X. Hu, G. W. Kattawar, M. I. Mishchenko, and Q. Fu, 2005: Scattering and absorption property database for nonspherical ice particles in the near-through far infrared spectral region. *Appl. Opt.*, **44,** 5512-5523.

——, L. Zhang, G. Hong, S. L. Nasiri, B. A. Baum, H.-L. Huang, M. D. King, and S. Platnick, 2007: Differences between collection 4 and 5 MODIS ice cloud optical/microphysical products and their impact on radiative forcing simulations. *IEEE Trans. Geosci. Remote Sens.*, **45,** 2886-2899.

——, G. W. Kattawar, G. Hong, P. Minnis, and Y. X. Hu, 2008: Uncertainties associated with the surface texture of ice particles in satellite-based retrieval of cirrus clouds: Part I. Single-scattering properties of ice crystals with surface roughness. *IEEE Trans. Geosci. Remote Sens.*, **46,** 1940-1947.

——, L. Bi, B. A. Baum, K. N. Liou, G. W. Kattawar, M. I. Mishchenko, and B. Cole, 2013: Spectrally consistent scattering, absorption, and polarization properties of atmospheric ice crystals at wavelengths from 0.2 to 100 μm.

Yue, Q. and K. N. Liou, 2009: Cirrus cloud optical and microphysical properties determined from AIRS infrared spectra. *Geophys. Res. Lett.*, **36,** L05810, doi:10.1029/2008GL036502679.

Yurkin, M. A. and A. G. Hoekstra, 2011: The discrete-dipole-approximation code ADDA: capabilities and known limitations. *J. Quant. Spectrosc. Radiat. Transfer*, **112,** 2234-2247.

Zhang, Z., P. Yang, G. W. Kattawar, S. C. Tsay, B. A. Baum, Y. X. Hu, A. J. Heymsfield, and J. Reichardt, 2004: Geometrical-optics solution to light scattering by droxtal ice crystals. *Appl. Opt.*, **43,** 2490-2499.

——, ——, ——, H.-L. Huang, T. Greenwald, J. Li, B. A. Baum, D. K. Zhou, and Y. X. Hu, 2007: A fast infrared radiative transfer model based on the adding–doubling method for hyperspectral remote-sensing applications. *J. Quant. Spectrosc. Radiat. Transfer*, **105,** 243-263.

——, ——, ——, J. Riedi, L. C. Labonnote, B. A. Baum, S. Platnick, and H. L. Huang, 2009: Influence of ice particle model on retrieving cirrus cloud optical thickness from satellite measurements: model comparison and implication for climate study. *Atmos. Chem. Phys.*, **9,** 1-15.